

Inhomogeneous chiral symmetry breaking phases

Vom Fachbereich Physik
der Technischen Universität Darmstadt

zur Erlangung des Grades
eines Doktors der Naturwissenschaften
(Dr. rer. nat.)

genehmigte Dissertation von
M. Sc. Stefano Carignano
aus Moncalieri, Italien

Darmstadt 2012
D17

Referent: Priv. Doz. Dr. Michael Buballa
Korreferent: Prof. Dr. Jochen Wambach

Tag der Einreichung 11.07.2012
Tag der Prüfung: 24.10.2012

Abstract

In this thesis we investigate the formation of inhomogeneous chiral symmetry breaking phases, characterized by a spatially modulated quark-antiquark condensate. In order to determine the relevance of this kind of structure for the phase diagram of strongly interacting matter, we employ the Nambu–Jona-Lasinio model for two light quark flavors and study the properties of the ground state of the system. After observing the appearance of an inhomogeneous “island” at low temperatures and intermediate chemical potentials in the model phase diagram, we compare different one- and two-dimensional crystalline shapes for the chiral condensate, in order to determine which one is the thermodynamically most favored. Once having determined the favored shape for the ground state of the system, we study in more detail the properties of this inhomogeneous phase. We then investigate the effects on it of common model extensions like the inclusion of vector interactions and an effective coupling with the Polyakov loop. Finally, in order to compare our results with recent predictions on inhomogeneous structures from quarkyonic matter studies, we study the model phase structure at higher chemical potentials and determine that the favored shape for the system ground state changes. A careful discussion on the interpretation of these results is included as well.

Zusammenfassung

In dieser Arbeit untersuchen wir die Bildung von inhomogenen, die chirale Symmetrie brechenden Phasen, welche durch ein räumlich variierendes Quark-Antiquark Kondensat charakterisiert werden. Um herauszufinden, ob solche Strukturen im Phasendiagramm von stark wechselwirkender Materie relevant sind, nutzen wir ein Nambu-Jona-Lasinio-Modell mit zwei leichten Quark-Freiheitsgraden und untersuchen die Eigenschaften des Grundzustands des Systems. Nachdem wir einen inhomogenen Bereich (“Insel”) bei kleinen Temperaturen und mittlerem chemischen Potential im Phasendiagramm des Modells gefunden haben, untersuchen wir verschiedene ein- und zweidimensionale Kristallstrukturen für das chirale Kondensat, um den thermodynamisch niedrigsten Zustand zu bestimmen. Im Anschluss bestimmen wir ausführlich die Eigenschaften der gefundenen inhomogenen Phasen und untersuchen die Auswirkungen von typischen Erweiterungen des Modells wie die Hinzunahme von Vektorwechselwirkungen und das Ankoppeln an den Polyakov-Loop. Abschließend vergleichen wir unsere Ergebnisse mit jüngsten Vorhersagen von Studien über quarkionische Materie bei hohem chemischen Potential und finden, dass sich dort der bevorzugte Grundzustand des Systems ändert. Wir enden mit einer Diskussion und Interpretation der Ergebnisse.

*You can't always get what you want /
But if you try sometimes, you just might find /
You'll get what you need.*

– The Rolling Stones

Contents

1. Introduction	1
2. Formalism	7
2.1. QCD and symmetries	7
2.2. The NJL model	8
2.2.1. Mean-field approximation	9
2.2.2. Vacuum phenomenology: dynamical chiral symmetry breaking	11
2.2.3. Extension to finite temperature and chemical potential	12
2.2.4. Regularization	15
2.3. The Quark-Meson model	16
3. Diagonalization of the Hamiltonian: zero temperature results	19
3.1. Homogeneous chiral condensates	19
3.2. Inhomogeneous chiral condensates: general approach	20
3.2.1. Lower-dimensional modulations	22
3.3. One-dimensional modulations	23
3.3.1. Chiral density wave	24
3.3.2. Sinusoidal modulation	25
3.3.3. Solitonic solutions	26
3.4. Two-dimensional modulations	28
3.4.1. Egg carton	29
3.4.2. Honeycomb	30
3.5. Comparison of free energies	31
3.5.1. Most favored 1D modulation	31
3.5.2. Most favored: 1D vs 2D	33
4. Solitonic solutions	37
4.1. Phase diagram	37
4.2. Density profiles	39
4.3. Finite quark masses	40
4.4. Quark-Meson model results	41
5. Effects of model extensions on inhomogeneous phases	43
5.1. Inclusion of vector-channel interactions	43
5.1.1. Homogeneous case	44
5.1.2. Inhomogeneous case: solitonic solutions	44
5.1.3. Chiral density wave	49

5.1.4. Quark number susceptibilities	50
5.1.5. Finite current quark masses and vector interaction	53
5.2. Effects of Polyakov loop dynamics	53
5.2.1. Homogeneous case	55
5.2.2. Inhomogeneous case	56
5.2.3. PNJL and large N_c	57
6. Inhomogeneous phases at higher densities	59
6.1. An inhomogeneous “continent”	59
6.2. Favored phase at high densities	64
7. Conclusions	67
A. Conventions	70
B. Details on the formalism	71
B.1. Mean-field Lagrangian	71
B.2. Inverse propagator in momentum space	71
C. Regularization	74
C.1. Isolating vacuum and medium contributions	74
C.2. Regularization schemes	76
C.2.1. Three-momentum cutoff	76
C.2.2. Free energy regularization	76
C.2.3. Vacuum proper-time regularization	77
C.2.4. Pauli-Villars	79
C.3. Parameter fitting	79
D. Parameter sets	80
D.1. NJL parameters	80
D.2. QM parameters	80
D.3. PNJL parameters	81
E. More details on the solitonic solutions	82
E.1. Density of states	82
F. Spatially dependent density	86
G. Ginzburg-Landau expansion for vector interactions	89
H. Lattice structures and symmetries	92
H.1. Two-dimensional lattice structures	93
I. Numerical diagonalization of the Hamiltonian	97
I.1. Cutoff and asymptotic density of states	98
I.2. Analytical expressions for the chiral density wave modulation	99

1. Introduction

The standard model of particle physics is nowadays the widely accepted fundamental quantum field theory describing known particles and their interactions, with the exception of gravitational forces. Its elegant description of the fundamental forces among particles in terms of local gauge symmetries has proven to be extremely successful over the last years, with a great number of experimental confirmations culminating in the recent discovery of a possible signal for the Higgs boson [1].

The gauge theory in the standard model describing strong interactions is called quantum chromodynamics (QCD), and is based on the $SU(3)$ color group. Its matter content consists of quarks, which are spin 1/2 point-like particles considered to be the fundamental constituents of hadrons, while the interaction is mediated by massless spin 1 gauge bosons called gluons. Both quarks and gluons carry color, which plays the role of a charge (in analogy with the electric one) for strong interactions. However, due to the non-abelian structure of the theory, QCD features more interaction vertices compared to quantum electrodynamics, resulting in a completely different behavior.

Other than color, quarks carry an additional “flavor” internal degree of freedom: one thus distinguishes between up, down, strange, charm, beauty and top quarks.

The most prominent feature of QCD, which renders it still nowadays, more than 40 years after its introduction, one of the most interesting and challenging subjects in contemporary physics, is its strongly coupled nature for low energies. Indeed, it has been determined that the strength of the interaction between quarks and gluons grows at large distances, or equivalently for small energies or momenta. This property results in a whole series of characteristic low energy features, like confinement and spontaneous chiral symmetry breaking, and is believed to be largely responsible for the observed values of the hadron masses, as well as for the impossibility to observe free quarks experimentally. On the other hand, the value of the coupling decreases at high energies, leading to the so-called asymptotic freedom [2, 3], which allowed to identify quarks as fundamental constituents of hadronic matter.

Since the value of the strong coupling constant increases with decreasing energies, well-established perturbative techniques (which have proven to be extremely successful in quantum electrodynamics at all scales of interest) are applicable only to study high energy and short distance processes involving strong interactions, but turn out to be completely inadequate to describe ground state and vacuum properties of QCD, including hadron spectra. The typical energy scale where non-perturbative effects are expected to dominate is given by the so-called Λ_{QCD} , which is found to be around 200 MeV. This Λ_{QCD} can be interpreted as a characteristic energy scale for the theory. It is comparable, for example, to the typical hadron masses and sizes (for this it is sufficient to recall that in natural units 200 MeV corresponds to approximately 1 fm).

In the present work, we will mainly focus on the aspect of dynamical mass generation, a non-perturbative phenomenon which can be related to the spontaneous breaking of chiral symmetry by the QCD ground state and the consequent formation of a $\bar{q}q$ condensate.

While being aware that vacuum properties of the theory are still not yet completely understood, nuclear physicists have recently drawn their attention towards the mapping of the QCD phase diagram, that is, the study of the behavior of strongly interacting matter at non-zero temperature T and baryon density (or equivalently chemical potential μ) [4, 5, 6, 7]. Inspired by the asymptotic freedom property of the theory, it has been argued already several years ago that above a given temperature close to Λ_{QCD} , any hadronic system should experience a phase transition, and behave as a free chirally symmetric gas of deconfined partons [8]. This simplistic assumption has been subsequently refined, and nowadays we expect to have such a free gas phase only at asymptotically high temperatures. It is worth noting that although chiral symmetry breaking and confinement are both related to the strongly coupled nature of the theory, it is not clear *a priori* whether the phase transition will involve both of them at the same time, or if two transitions will occur at separate values of temperature and baryon chemical potential.

Most of the current knowledge on the QCD phase diagram revolves around the $\mu = 0$ axis. This is in fact the region which is being currently experimentally accessed by heavy-ion collisions at RHIC in Brookhaven and LHC at CERN. On the theory side, ab-initio lattice QCD calculations have been able to give estimates on the critical temperature and the nature of the phase transition, which according to the latest results is rather expected to be a crossover [9, 10, 11].

On the other hand, in spite of considerable efforts, our current understanding of the phase diagram at low temperatures and intermediate baryon chemical potentials is still rather scarce. On the experimental side, current heavy ion colliders are not able to access this region, although future facilities like FAIR at GSI in Darmstadt and NICA at JINR in Dubna do aim to explore properties of dense and cold strongly interacting matter through high luminosity low energy collisions [12, 13]. Some insight on this region of the phase diagram may be inferred from the phenomenology of compact stars, a field which in any case presents several experimental challenges as well (for dedicated reviews, see *e. g.* [14, 15]). From the theory point of view, current lattice calculations are unable to provide reliable results at intermediate and high densities due to the so-called sign problem. The most widely employed tools to study this region are then effective models, which share some basic properties with QCD but feature simplified interactions and are as such more easily tractable. More refined techniques using functional methods based on full QCD have been applied to this problem as well, although they require considerably more effort and have still limited predictive power [16, 17].

The phase structure of QCD at low temperatures in the chemical potential direction is at any rate expected to be rich (for dedicated reviews, see *e. g.* [18, 19]). Indeed, while chiral symmetry is expected to be restored at high densities, other effects may appear, like the formation of a color-superconducting phase [20, 21, 22, 23] (see [24] for a recent review). This kind of phase is expected to be the true ground state of QCD at asymptotically high chemical potentials, although its possible extension to intermediate densities is not yet clearly determined and current results are strongly model-dependent [25, 18, 24].

The low temperature and intermediate density regime could also be characterized by the formation of inhomogeneous phases, characterized by a spatial dependence of the properties of the system, possibly leading to the formation of crystalline structures (a brief recent review on the topic is presented in [26]).

The idea of inhomogeneous phases for strongly interacting matter is certainly not a new one. More than 50 years ago, Overhauser suggested that the true ground state of nuclear matter might be characterized by the presence of large static density waves [27]. Aside from that, nuclear matter is also expected to form “pasta” phases, characterized by different kinds of spatial inhomogeneities according to the density of the system [28]. The Skyrme picture describing nucleons as chiral solitons has also been successfully employed in describing dense strongly interacting matter, and seems to predict the formation of three-dimensional crystalline structures [29, 30]. More recent studies of cold nuclear matter using holographic models seem to predict the formation of spatially inhomogeneous structures as well [31].

Spatially dependent states have also been discussed in the context of pion condensation within the framework of sigma models. In those cases as well the condensate field is expected to be spatially modulated [32].

Crystalline phases are also expected to be relevant in the context of (color-)superconductivity, which, in spite of being driven by different physical effects, has many formal analogies with the mechanism of spontaneous chiral symmetry breaking in QCD. The well-known BCS effect involves quarks at the Fermi surface, since the essence of the Cooper instability lies in the zero free energy cost required to excite a pair [33]. In presence of imbalanced Fermi surfaces, a condition which can arise in a superconductor in presence of an external magnetic field or for quark matter in the interior of a neutron star, the phase space for formation of Cooper pairs is however reduced and different pairing mechanisms may come into play [34]. One of the most plausible outcomes is the formation of pairs with nonzero total momentum, leading to a spatially inhomogeneous gap (for a dedicated review, see [35]). The study of these crystalline superconducting phases has been mostly conducted through effective model analyses considering different shapes for the inhomogeneous gap, with the most popular being a single plane wave, the so-called Fulde-Ferrell ansatz [36], although real sinusoidal solutions have been investigated as well (the LOFF case [37]).

In a recent numerical analysis considering more general solutions, it has been determined that the preferred one-dimensional shape for the color-superconducting gap in presence of imbalanced Fermi surfaces is a solitonic structure that can be well fitted by Jacobi elliptic functions [38]. Although numerical investigations mainly considered one-dimensional modulations for the gap function, Ginzburg-Landau analyses have determined that the formation of higher-dimensional crystalline structures may lead to an even bigger gain in the free energy [39, 40, 41, 42]. In particular, for the case of crystalline color-superconductivity the system is expected to form a full three-dimensional structure, and it appears that the cubic shape is the most favored.

Inhomogeneous phases play an important role in theories defined in one spatial dimension, which are often used as toy models to understand qualitative features of their higher dimensional counterparts. Of particular interest for us are the 1+1-dimensional Gross-

Neveu (GN) model [43] and its chiral counterpart, the NJL_2 model, which share with QCD the phenomenon of spontaneous chiral symmetry breaking and have the advantage of being for the most part analytically solvable [44, 45, 46, 47, 48, 49].

Until recently, the phase diagram of the GN model was expected to feature a phase transition from an homogeneous chirally broken to a chirally restored phase, similar to the naive picture developed for the QCD phase diagram. This picture has been dramatically revised by a recent analysis which has revealed the presence of a crystalline phase, characterized by a spatially modulated chiral condensate. In particular, it has been shown that in the GN model, similarly to what happens for one-dimensional superconducting gaps, the chiral order parameter assumes a solitonic shape and can be parametrized in terms of Jacobi elliptic functions [45, 46, 50]. On the other hand, for the NJL_2 model it has been argued that a chiral transformation can map the vacuum results into any finite chemical potential, resulting in a phase for low temperatures extending to arbitrarily high μ where the chiral order parameter assumes a plane wave shape (a so-called “chiral spiral”) [44, 48, 49, 51].

It is known in general that one-dimensional models will always favor the formation of inhomogeneous condensates as long as an attractive interaction is present, due to the effect of nesting of the Fermi surface [52, 53, 54]. As such, they can only hint on the importance of inhomogeneous phases, but in order to assess the role of these phases in higher dimensions a full analysis on the system of interest is required. In particular, for a 3+1-dimensional system crystalline phases are expected to form only for sufficiently strong couplings in the relevant channels [55, 54]. The outcome for QCD is therefore unclear, but since in the intermediate density region we still expect a strong coupling regime, inhomogeneous phases cannot be ruled out a priori.

Let us then come back to our main topic of interest for the present work, namely the possibility for spatially inhomogeneous chiral symmetry breaking phases, characterized by a spatially modulated shape of the chiral condensate, in the QCD phase diagram. The usual picture for chiral symmetry breaking involves the pairing between quarks and antiquarks, which becomes disfavored at high chemical potentials since the excitation of antiparticles becomes increasingly expensive in terms of free energy. At finite densities however we can expect a significant contribution to the $\bar{q}q$ condensate coming from quark-hole paring [56, 57, 54, 58]. In particular, we can imagine that the favored pairing pattern would involve quarks and holes carrying finite momenta, both pointing in the same direction, and that the resulting condensate would then also be characterized by a nonzero momentum, resulting in spatial inhomogeneities.

In order to investigate this kind of condensate, we turn back to quark matter in 3+1 dimensions. The idea of a crystalline chiral condensate has already been proposed several years ago for QCD at high densities [56], although a successive weak coupling analysis showed that at asymptotic densities this kind of phase is favored over color superconductivity only if the number of colors N_c is assumed to be unrealistically large [57, 59].

This kind of analysis however cannot lead to any conclusive result in the intermediate density regime, where the coupling is not yet expected to be small. While of course an investigation using ab-initio methods based on full QCD would eventually be able to provide a definite answer, lattice simulations cannot currently confirm or rule out the

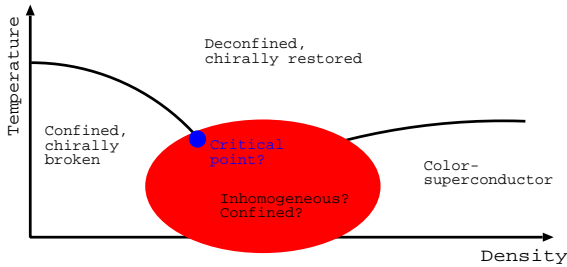


Figure 1.1.: Sketch of the QCD phase diagram. Starting from the confining and chirally broken phase at low temperatures and densities, if we increase the chemical potential a crystalline phase may appear before the onset of color-superconductivity. The position of the critical point might be affected by the presence of such phase.

possibility for the appearance of chiral crystalline phases [60].

For this region, effective models have been employed to study the impact of spatial modulations of the chiral condensate on the phase diagram. Most analyses until now have been performed by enforcing simple shapes of the chiral order parameter. In particular, the most widely employed is the so-called “chiral density wave”, which amounts to a simple plane wave modulation. In spite of this simplistic ansatz, the phase diagram has been shown to be dramatically modified when allowing for the formation of crystalline phases, with the appearance of an inhomogeneous “island” around the usual phase transition line from the chirally broken to the symmetric phase [61, 54, 62].

The main goal of the present work is to extend this kind of analysis, by allowing for more general shapes of the chiral condensate and determine how the phase structure is modified. For this, we will employ the Nambu–Jona-Lasinio (NJL) model, which has been already extensively applied to study the dynamics of spontaneous chiral symmetry breaking in quark matter. A complementary investigation using the similar Quark-Meson (QM) model will be performed as well. Our analysis will then be extended by considering some common extensions of the model, namely the coupling with the Polyakov loop and the inclusion of repulsive vector interactions. We will also investigate the effects of inhomogeneous phases on the position of the critical point, whose existence is one of the main questions revolving around the QCD phase diagram [63, 64, 4]. A sketch of the possible phase diagram we have in mind is presented in Fig. 1.1.

Finally, we would like to recall another recent theoretical development proposed in order to achieve a better understanding of the finite density behavior of QCD, revolving around the concept of the so-called “Quarkyonic” matter. For this, the limit of QCD for a large number of colors ($N_c \rightarrow \infty$) is taken, leading to the suppression of several effects [65, 66], and thus allowing to give qualitative estimates on some features of the phase diagram. It has then been argued that at low temperatures and intermediate chemical potentials matter may behave in a new way, with a system characterized by the presence of a Fermi sea with quark degrees of freedom whose excitations are however confined [67].

Although an early definition of quarkyonic matter was that of a confined, yet chirally restored matter, the current understanding is that chiral symmetry is still broken in this quarkyonic phase, although in a spatially inhomogeneous way. In particular, it has been argued that in this framework the interaction at high densities involves particles on the Fermi surface, and the effective problem of chiral symmetry breaking is dimensionally reduced. This in turn leads to the formation of “quarkyonic chiral spirals”, in analogy with the NJL_2 model [58, 68]. As the chemical potential increases, the Fermi sphere is expected to be deformed in patches, allowing for the formation of additional chiral spirals, which superimpose to form increasingly complex crystalline structures [69, 70]. Since throughout this work we will allow for crystalline structures in more than one spatial dimension, we will seek to confront qualitatively our results with these predictions.

The thesis is structured as follows: in Chapter 2, after briefly reviewing the QCD Lagrangian and its symmetries of interest for us, we introduce the NJL and the QM model and describe the procedure for implementing spatial modulations of the chiral condensate in mean-field approximation. More details on the formalism, as well as the numerical implementation, are reported in appendices B and I. In Chapter 3 we present numerical results for the various shapes of the chiral condensate we considered, and determine which one is energetically favored in the model ground state. Once having determined the favored shape for the chiral condensate, we perform a more detailed analysis of the model phase diagram in Chapter 4. Chapter 5 is devoted to the discussion of the effects of introducing vector interactions and an effective coupling with the Polyakov loop on chiral crystalline phases. Finally, in Chapter 6 we investigate the phase structure of the model at higher chemical potentials, in order to compare with recent quarkyonic matter studies.

Most of the results presented in Chapters 4, 5 and 6 have already been published in [71, 72, 73].

2. Formalism

In this chapter we present our formalism. After briefly reviewing the symmetries of QCD we are mainly interested in, we introduce the Nambu–Jona-Lasinio model and describe the procedure for tackling inhomogeneous chiral condensates. Our conventions are presented in Appendix A, while more details on our calculations are shown in Appendix B and Appendix I.

2.1. QCD and symmetries

The concept of symmetry is a powerful tool that can be used to characterize properties of a theory, and is as such widely employed in modern physics. In particular, a common practice when studying theories which are not easily solvable is to introduce simplified models featuring the same symmetries, since their qualitative behavior can be expected to be very similar.

Since we are interested in describing strongly interacting matter, our starting point is the QCD Lagrangian:

$$\mathcal{L}_{QCD} = -\frac{1}{4}F_{\mu\nu}^a F_a^{\mu\nu} + \bar{\psi}(i\gamma^\mu D_\mu - \hat{m})\psi. \quad (2.1)$$

The first part of Eq. (2.1) contains the gauge field stress tensor

$$F_{\mu\nu}^a = \partial_\mu A_\nu^a - \partial_\nu A_\mu^a - g f_{bc}^a A_{\mu,b} A_{\nu,c}, \quad (2.2)$$

and thus describes the gluon contribution, whereas the second part is the Dirac Lagrangian for the quark fields ψ , including the covariant derivative D_μ which provides the minimal coupling between matter and gauge bosons:

$$D_\mu = \partial_\mu + ig A_\mu^a \lambda_a, \quad (2.3)$$

here g is the strong coupling constant, λ_a are Gell-Mann matrices acting on quarks, which lie in the fundamental representation of the color gauge group, and a, b, c are color indices.

The matrix $\hat{m} = \text{diag}\{m_u, m_d, m_s, \dots\}$ contains the bare (or current) quark masses. While up and down quarks are characterized by similar and comparatively small current masses ($m_u \approx m_d \approx 5$ MeV), we know that charm, beauty and top quarks have masses above 1 GeV and are as such not expected to play a role in low and intermediate energy phenomena. The strange mass on the other hand sits on an intermediate value of approximately 100 MeV, so that this quark degree of freedom might become relevant at intermediate densities and temperatures.

If we aim to build a simple effective model to describe low energy QCD phenomenology, we can nevertheless restrict ourselves to the two lightest quark flavors. In this case, if we consider their bare masses to be equal ($m_u = m_d$), it can be seen that QCD exhibits an $SU_V(N_f = 2)$ global symmetry, that is, its Lagrangian is invariant under transformations given by

$$\psi \rightarrow e^{i\boldsymbol{\tau} \cdot \boldsymbol{\theta}/2} \psi, \quad (2.4)$$

where $\boldsymbol{\tau}$ is a vector containing Pauli matrices acting on flavor space. If the bare quark masses are additionally set to zero (*i. e.* we consider the so-called *chiral limit*, $m_u = m_d = 0$), we have an additional $SU_A(2)$ global symmetry, resulting in an invariance under the transformation

$$\psi \rightarrow e^{i\gamma^5 \boldsymbol{\tau} \cdot \boldsymbol{\theta}/2} \psi. \quad (2.5)$$

These two global symmetries can be rewritten as $SU_L(2) \times SU_R(2)$. This is the so-called chiral symmetry of QCD, reflecting the fact that left-handed and right-handed fields transform independently (for a pedagogical introduction, see *e. g.* [74]). Since degenerate chiral partners are not observed in the hadron spectrum, chiral symmetry is expected to be spontaneously broken by the QCD vacuum.

Strictly speaking, QCD is not exactly chirally symmetric (we know that $0 \neq m_u \neq m_d \neq 0$), and indeed we do not observe experimentally massless Goldstone bosons [75] associated with its spontaneous breaking. One can nevertheless speak of an approximate symmetry, and expect the effects of the explicit breaking to be small. This is reflected for example in the small mass of the pion, which can then be interpreted as pseudo-Goldstone boson in this context.

Knowing that our main focus is on the low temperature and intermediate chemical potential region of the phase diagram of strongly interacting matter, we choose to employ an effective model which shares some of the QCD symmetries, in spite of featuring simplified interactions. In particular, since we are interested in the phenomenon of spontaneous chiral symmetry breaking, we will mostly make use of the well-known Nambu–Jona-Lasinio (NJL) model. For completeness, we will also perform a partial investigation using the similar Quark-Meson (QM) model.

2.2. The NJL model

In this section we introduce the NJL model, characterized by a chirally invariant non-renormalizable four-fermion interaction (for dedicated reviews, see *e. g.* [76, 77, 78, 18]).

The original work of Nambu and Jona-Lasinio dates back to before QCD, when the model aimed to provide a field-theoretical description of nucleons, featuring a mechanism for dynamical mass (gap) generation in analogy with the microscopic theory of superconductivity [79, 80]. With the advent of QCD, the fermionic fields in the Lagrangian have been reinterpreted as quarks, incorporating additional quantum numbers, *i. e.* color degrees of freedom. The NJL model shares the same global symmetries with Quantum

Chromodynamics, but features no gluons and therefore no running coupling and no confinement.

In its simplest form, the two-flavor NJL Lagrangian reads [80]

$$\mathcal{L}_{NJL} = \bar{\psi}(i\gamma^\mu\partial_\mu - \hat{m})\psi + G_S ((\bar{\psi}\psi)^2 + (\bar{\psi}i\gamma^5\tau_a\psi)^2) , \quad (2.6)$$

where the first part is nothing but the free Dirac Lagrangian, while the second part describes the four-fermion interactions. The interaction term features a scalar ($\bar{\psi}\psi$) and a pseudo-scalar ($\bar{\psi}i\gamma^5\tau_a\psi$) term, both characterized by the same coupling constant G_S , describing an attractive interaction in these quark–anti-quark channels. In our formalism, the field ψ represents quarks which in 3+1 dimensions are described by 4-component Dirac spinors. In the two-flavor approximation which we will employ in this work, quarks have $N_f = 2$ isospin and $N_c = 3$ color degrees of freedom. Here $\{\gamma^\mu\}$ and γ^5 are Dirac matrices and τ_a are Pauli matrices acting on the two-dimensional isospin space. The flavor index a runs from 1 to 3. The matrix \hat{m} contains the bare masses for the two quark flavors, which in this work are assumed to be degenerate:

$$\hat{m} = \text{diag}\{m_u, m_d\} = m \text{ diag}\{1, 1\} . \quad (2.7)$$

Due to the nature of the 4-fermion vertex in Eq. (2.6), the NJL model is non-renormalizable. This is reflected in the dimensionful coupling constant G_S , which carries the units of an inverse energy squared. The model will therefore require some regularization procedure to render its results finite, and the outcomeing phenomenology will depend on the prescription used. In this sense, the model is to be interpreted as an effective low-energy theory for strongly interacting quarks, and is as such not expected to be reliable above a given scale, identified by the regulator used. The value of the regulator Λ , together with the coupling constant G_S , are model parameters which will need to be fixed. This is typically done by fitting vacuum observables, as described in Appendix C.

2.2.1. Mean-field approximation

Throughout this work, we will make use of the widely employed mean-field (or equivalently Hartree) approximation. This basically amounts to replacing in the Lagrangian Eq. (2.6) the field bilinears we are interested in by their expectation values, and neglecting higher order fluctuations [81, 78, 18]. The resulting action becomes gaussian in the fermionic fields, which may be then integrated out. Specifically, we introduce the expectation values for the scalar and pseudoscalar condensate, $\langle\bar{\psi}\psi\rangle = \phi_S(x)$ and $\langle\bar{\psi}i\gamma^5\tau^a\psi\rangle = \phi_P^a(x)$ respectively, and write

$$\bar{\psi}\psi = \phi_S(x) + \delta\phi_S, \quad \bar{\psi}i\gamma^5\tau^a\psi = \phi_P^a(x) + \delta\phi_P^a . \quad (2.8)$$

After neglecting $\mathcal{O}(\delta\phi^2)$ terms, the mean-field Lagrangian becomes

$$\mathcal{L}_{MF} = \bar{\psi}S^{-1}\psi - \mathcal{V} , \quad (2.9)$$

where we identified in the first part of the expression the mean-field inverse quark propagator

$$S^{-1}(x) = i\gamma^\mu \partial_\mu - m + 2G_S(\phi_S(x) + i\gamma^5 \tau_a \phi_P^a(x)), \quad (2.10)$$

and the second field-independent part gives the contribution of the condensates,

$$\mathcal{V} = G_S(\phi_S(x)^2 + \phi_P^a(x)^2). \quad (2.11)$$

It is useful to rewrite the mean-field Lagrangian as

$$\mathcal{L}_{MF} = \bar{\psi} \gamma^0 (i\partial_0 - \mathcal{H}) \psi - \mathcal{V}, \quad (2.12)$$

where we isolated the temporal derivative in the inverse quark propagator and introduced the hermitian effective mean-field Hamiltonian operator

$$\mathcal{H} = \gamma^0 [-i\gamma^i \partial_i + m - 2G_S(\phi_S + i\gamma^5 \tau_a \phi_P^a)]. \quad (2.13)$$

For computational reasons, in the following we will restrict ourselves to a diagonal structure in isospin space, thus not allowing for charged pion condensation (which is not expected to happen in any case at zero isospin chemical potential):

$$\phi_P^a = \phi_P^3 \delta_{a3}, \quad (2.14)$$

and relabel the resulting $\phi_P^3(x)$ mean field as $\phi_P(x)$. The mean-field \mathcal{H} can then be reduced to a direct product in flavor space of two isospectral Hamiltonians \mathcal{H}_\pm :

$$\mathcal{H} = \gamma^0 [-i\gamma^i \partial_i + m - 2G_S(\phi_S + i\gamma^5 \tau_3 \phi_P)] = \mathcal{H}_+ \otimes \mathcal{H}_-, \quad (2.15)$$

where

$$\mathcal{H}_\pm = \gamma^0 [-i\gamma^i \partial_i + m - 2G_S(\phi_S \pm i\gamma^5 \phi_P)]. \quad (2.16)$$

It is worth mentioning at this point that although in principle the mean fields may carry an explicit spatial and temporal dependence, most model analyses performed so far neglect both possibilities. For the present work, we will still consider our condensates to be static (*i.e.* time-independent), but allow them to be spatially dependent:

$$\phi_S(x) \rightarrow \phi_S(\mathbf{x}), \quad \phi_P(x) \rightarrow \phi_P(\mathbf{x}). \quad (2.17)$$

As it will become evident in the following, this generalization greatly complicates the calculations, and the problem for an arbitrary three-dimensional spatial modulation will in general not be treatable. Indeed, all of our results in the following are obtained by enforcing an ansatz for a given shape of the chiral condensate. For later convenience, we also introduce an inhomogeneous "mass" function

$$M(\mathbf{x}) = m - 2G_S(\phi_S(\mathbf{x}) + i\phi_P(\mathbf{x})), \quad (2.18)$$

from which the condensate part in \mathcal{L}_{MF} can be rewritten as

$$\mathcal{V} = \frac{|M(\mathbf{x}) - m|^2}{4G_S}. \quad (2.19)$$

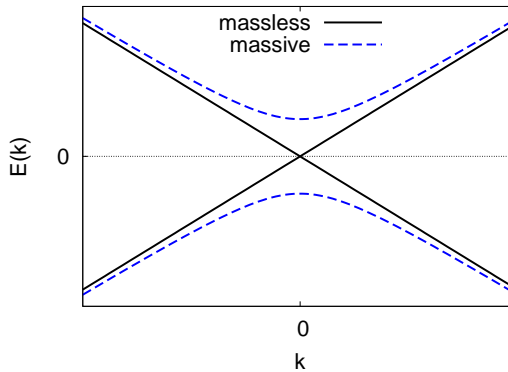


Figure 2.1.: Dispersion relation $E(k)$ for massless (solid line) and massive (dashed line) quarks

We can also obtain an expression for the mean-field Hamiltonian in terms of the combination M and its complex conjugate, instead of the single mean-fields. For that, we explicit the Dirac structure using the chiral representation for the gamma matrices (see Appendix A for our conventions) and arrive at the following expression for \mathcal{H}_+ in coordinate space:

$$\mathcal{H}_+ = \gamma^0 [-i\gamma^i \partial_i + m - 2G_S(\phi_S + i\gamma^5 \phi_P)] = \begin{pmatrix} i\sigma^i \partial_i & M(\mathbf{x}) \\ M^*(\mathbf{x}) & -i\sigma^i \partial_i \end{pmatrix}, \quad (2.20)$$

where σ^i are 2x2 Pauli matrices. The lower component \mathcal{H}_- can be obtained by simply swapping M with M^* . Since the two are isospectral, in the following we will always consider \mathcal{H}_+ only and call it \mathcal{H} .

While the mean-field approach we developed in this section will clearly fail to describe accurately critical phenomena, we expect to be able to obtain from it some insight on the phase structure of the model. In particular, we aim to get a qualitative picture of how the phase diagram is modified when allowing for the formation of crystalline phases. For this, after briefly reviewing its vacuum phenomenology, we will discuss the extension of the model to finite temperatures and densities.

2.2.2. Vacuum phenomenology: dynamical chiral symmetry breaking

Due to the attractive interaction in the quark-antiquark channel, the NJL model exhibits spontaneous chiral symmetry breaking in vacuum. This implies that it is energetically favorable for the system to develop a gap in the energy spectrum, or equivalently a “constituent” mass for the quarks. Since the vacuum is not expected to spontaneously break translational invariance, in this section we will focus on homogeneous chiral condensates only.

This property can be intuitively understood by picturing the filled Dirac sea characterizing the vacuum state of the model (Fig. 2.1). In presence of a gap, the negative energy



Figure 2.2.: Dyson equation for the NJL quark propagator in Hartree approximation. Thin lines denote bare propagators, thick lines full ones.

branch gets shifted downwards and the overall energy of the system is lowered. This effect will compete with the positive contribution coming from the condensation energy \mathcal{V} , and an equilibrium value for the gap will be determined by the balance between these two.

The phenomenon of spontaneous chiral symmetry breaking is also apparent when calculating the Dyson equation for the quarks (Fig. 2.2), which in Hartree approximation leads to the so-called “gap equation”

$$M_{vac} = m + 2i G_S \int \frac{d^4 p}{(2\pi)^4} \text{Tr } S(p) , \quad (2.21)$$

where the trace operation comes from the presence of a fermion loop and M_{vac} is the so-called vacuum “constituent” quark mass. Since for a spatially homogeneous chiral condensate in this approximation the self-energy is local, one simply obtains a constant shift in the fermion mass, *i. e.* quarks acquire an effective mass due to the interaction with the background mean-field chiral condensate. This “gap equation” is analogous to the ones typically encountered in (color-)superconductivity studies when determining the gap in the energy spectrum, and has to be solved self-consistently to determine the value of the constituent quark mass.

The NJL model can therefore account for the phenomenon of spontaneous chiral symmetry breaking in vacuum, through which quarks acquire their effective mass dressed by strong interactions. A very rough first estimate for this constituent mass for the two light quarks can be simply given by one third of the nucleon mass, $M_{vac} = M_N/3 \approx 310$ MeV.

2.2.3. Extension to finite temperature and chemical potential

Other than successfully describing vacuum phenomenology, the NJL model can be employed to study quark matter properties at finite temperature and density. In particular, we are interested in studying how medium effects like the presence of a Fermi sea of quarks affect the chiral condensate. For this, following standard methods of thermal field theory, we switch to a periodic imaginary time and use the conventional Matsubara formalism. The preferred ground state of the system can then be determined by minimizing the grand canonical thermodynamic potential Ω of the model.

The thermodynamic potential per unit volume as a function of temperature T and quark chemical potential μ can be written as a functional trace over the logarithm of the inverse quark propagator [82]. In particular, within our mean-field approximation, we can write the thermodynamic potential as an effective action in the expectation values introduced in

Sec. 2.2.1 using the path integral formalism. For a system in a four-volume $V_4 = \frac{1}{T} \times V$, it is given by the following functional integral over the fermionic fields $\bar{\psi}, \psi$ of the euclidean action \mathcal{S}_E :

$$\begin{aligned}\Omega(T, \mu; \phi_{S,P}) &= -\frac{T}{V} \log \int \mathcal{D}\bar{\psi} \mathcal{D}\psi \exp(\mathcal{S}_E) \\ &= -\frac{T}{V} \log \int \mathcal{D}\bar{\psi} \mathcal{D}\psi \exp \left(\int_{V_4} d^4 x_E (\mathcal{L}_{MF}(t = -i\tau, \mathbf{x}) + \mu \bar{\psi} \gamma^0 \psi) \right)\end{aligned}\quad (2.22)$$

where a finite chemical potential has been introduced through the addition of a term $\mu \bar{\psi} \gamma^0 \psi$ in the definition of the inverse propagator (or equivalently of the mean-field Lagrangian). As previously mentioned, since the mean-field Lagrangian is bilinear in the Grassmann variables $\psi, \bar{\psi}$, the gaussian integral in Eq. (2.22) can be readily evaluated, leading to

$$\log \int \mathcal{D}\bar{\psi} \mathcal{D}\psi \exp \left(\int_{V_4} d^4 x_E (\bar{\psi} S^{-1} \psi - \mathcal{V}) \right) = \log \text{Det} S^{-1} - \int_{V_4} d^4 x_E \mathcal{V}. \quad (2.23)$$

The logarithm of the determinant of the inverse quark propagator, which is an operator in Dirac, euclidean four-volume (or equivalently four-momentum), flavor and color space, can be turned into the trace of the logarithm of the propagator. This relation is obvious if the operator can be diagonalized, which is indeed our case. One thus arrives at the following expression:

$$\Omega = -\frac{T}{V} \text{Tr}_{Dirac,color,flavor,V_4} \log \left(\frac{S^{-1}}{T} \right) + \frac{T}{V} \int_{V_4} d^4 x_E \mathcal{V}. \quad (2.24)$$

In standard NJL, the inverse propagator is diagonal in color space, so the trace over it will simply amount to a factor of N_c . In flavor space, as mentioned before, the two components \mathcal{H}_\pm are isospectral and will contribute equally. One thus obtains an additional N_f factor.

In order to calculate the other traces, we have to diagonalize the remaining parts of the inverse quark propagator. For this, we first switch to momentum space by writing spinor fields and condensates as Fourier series. For a system in a finite volume V , we have

$$\psi(x) = \frac{1}{\sqrt{V}} \sum_{p_n} \psi_{p_n} e^{-ip_n x} = \frac{1}{\sqrt{V}} \sum_{\omega_n} \sum_{\mathbf{p}_n} \psi_{p_n} e^{-i(\omega_n \tau - \mathbf{p}_n \cdot \mathbf{x})}, \quad (2.25)$$

$$\bar{\psi}(x) = \frac{1}{\sqrt{V}} \sum_{p_n} \bar{\psi}_{p_n} e^{+ip_n x}. \quad (2.26)$$

When Fourier-transforming to momentum space, the physical quantities will depend on spatial three-momenta and discrete frequencies ω_n , due to the anti-periodic boundary conditions imposed on the time direction in order to introduce a finite temperature:

$$it = \tau \in [0, T], \quad p_n = \begin{pmatrix} i\omega_n \\ \mathbf{p}_n \end{pmatrix}. \quad (2.27)$$

For static condensates, the time component of the associated four-momentum is zero, that is,

$$M(\mathbf{x}) = \sum_{k_n} M_{k_n} e^{-ik_n x} = \sum_{\mathbf{k}_n} M_{k_n} e^{+i\mathbf{k}_n \cdot \mathbf{x}}, \quad k_n = \begin{pmatrix} 0 \\ \mathbf{k}_n \end{pmatrix}. \quad (2.28)$$

We can then plug in these Fourier expansions in the mean-field Lagrangian Eq. (2.9) and obtain the following expression for the inverse propagator in momentum space (the procedure is worked out in detail in the Appendix B):

$$\begin{aligned} S_{p_m, p_n}^{-1} &= \gamma^0 \left[i\omega_n \delta_{\mathbf{p}_n, \mathbf{p}_m} - \gamma^0 \boldsymbol{\gamma} \cdot \mathbf{p}_n \delta_{\mathbf{p}_n, \mathbf{p}_m} - \gamma^0 \sum_{\mathbf{k}_n} M_{k_n} \delta_{\mathbf{p}_n, \mathbf{p}_m + \mathbf{k}_n} + \mu \delta_{\mathbf{p}_n, \mathbf{p}_m} \right] \delta_{\omega_m, \omega_n} \\ &= \gamma^0 [i\omega_n \delta_{\mathbf{p}_n, \mathbf{p}_m} - \mathcal{H}_{\mathbf{p}_n, \mathbf{p}_m} + \mu \delta_{\mathbf{p}_n, \mathbf{p}_m}] \delta_{\omega_m, \omega_n}, \end{aligned} \quad (2.29)$$

which is diagonal in the Matsubara frequencies since the chiral condensate is assumed to be static.

Using once again the chiral representation for the Dirac matrices, a generic element of the mean-field Hamiltonian in momentum space will look like

$$\mathcal{H}_{\mathbf{p}_m, \mathbf{p}_n} = \begin{pmatrix} -\boldsymbol{\sigma} \cdot \mathbf{p}_m \delta_{\mathbf{p}_m, \mathbf{p}_n} & \sum_{\mathbf{q}_k} M_{\mathbf{q}_k} \delta_{\mathbf{p}_m, \mathbf{p}_n + \mathbf{q}_k} \\ \sum_{\mathbf{q}_k} M_{\mathbf{q}_k}^* \delta_{\mathbf{p}_m, \mathbf{p}_n - \mathbf{q}_k} & \boldsymbol{\sigma} \cdot \mathbf{p}_m \delta_{\mathbf{p}_m, \mathbf{p}_n} \end{pmatrix}. \quad (2.30)$$

In presence of an inhomogeneous chiral condensate, the diagonalization of \mathcal{H} is a highly non-trivial task, since quarks may exchange momenta by scattering off the condensate, as can be seen from the off-diagonal elements in Eq. (2.30). Consequently, quark momenta are not fixed and the mean-field propagator is not diagonal in momentum space.

What we have then for the thermodynamic potential is

$$\Omega = -TN_f N_c \sum_n \text{Tr}_{Dirac, \mathbf{p}} \text{Log} \left(\frac{1}{T} (i\omega_n - \mathcal{H} + \mu) \right) + \frac{1}{V} \int_V d\mathbf{x} \mathcal{V}, \quad (2.31)$$

where we already performed the trace in color and flavor space, and are left with a trace over Dirac and three-momentum space as well as a sum over Matsubara frequencies ω_n .

As previously noted, \mathcal{H} is an Hermitian operator and can therefore be diagonalized. In the following we will call E its eigenvalues in Dirac and momentum space. For brevity we will sometimes include the chemical potential in the definition of \mathcal{H} , and the resulting eigenvalues will be labeled $E - \mu \equiv E_\mu$. Since the inverse propagator Eq. (2.29) is diagonal in the Matsubara frequencies, we can make use of the well-known relation (up to an irrelevant temperature-independent constant) [82]

$$T \sum_n \text{Log} \left(\frac{i\omega_n + E_\mu}{T} \right) = \frac{E_\mu}{2} + T \text{Log} \left(1 + e^{-E_\mu/T} \right) = T \text{Log} \left[2 \cosh \left(\frac{E_\mu}{2T} \right) \right], \quad (2.32)$$

to perform the discrete frequency sum in Eq. (2.31). Our final expression for the thermodynamic potential is therefore (again, up to an irrelevant constant)

$$\begin{aligned}
\Omega(T, \mu; M(\mathbf{x})) &= -TN_f N_c \sum_E \log \left(2 \cosh \left(\frac{E - \mu}{2T} \right) \right) + \frac{1}{V} \int_V \frac{|M(\mathbf{x}) - m|^2}{4G_S} \\
&= \Omega_{kin} + \Omega_{cond},
\end{aligned} \tag{2.33}$$

where we have also identified for later convenience the kinetic contribution Ω_{kin} , described by the $\log(\cosh)$ term, as well as the condensate energy Ω_{cond} . In conclusion, the expression for the thermodynamic potential basically amounts to a sum over the eigenvalues of the effective Hamiltonian operator defined in Eq. (2.30), whose structure in Dirac and momentum space depends on the given shape of the chiral condensate.

In order to determine the thermodynamically favored shape of the mean-field $M(\mathbf{x})$, we must perform a functional minimization of Ω with respect to M . Alternatively, we can look for extrema of the thermodynamic potential by performing a functional derivative with respect to M and look for its zeros. This leads to in-medium gap equations, which have again to be solved self-consistently:

$$\frac{\delta \Omega}{\delta M(\mathbf{x})} = 0 \quad \longrightarrow \quad M(\mathbf{x}) = f(M(\mathbf{x})). \tag{2.34}$$

Since, as will become clear in the following when we define our numerical approach, in general the gap equations will become complicated matrix equations, we will mainly work by minimizing directly the thermodynamic potential. Details on this procedure and results will be described in Chapter 3.

2.2.4. Regularization

The expression obtained for the NJL thermodynamic potential Eq. (2.33) is formally divergent. This is due to the presence of an integral over all single particle energies, including the occupied states in the (infinitely filled) Dirac sea, which characterizes the vacuum state of the model.

In order to render our results finite, it is therefore necessary to regularize these diverging contributions in Ω . Since the NJL model is non-renormalizable, divergencies cannot be consistently absorbed at all orders in the free parameters and results will depend on the regularization scheme introduced to render the vacuum contribution finite.

The expression obtained for Ω_{kin} includes however both vacuum and medium contributions. If we blindly choose to regularize the full expression, we risk of introducing unwanted artifacts. A possible outcome is for example an artificial μ dependence of the order parameter [83], analogous to the one obtained in [38] on isospin chemical potential. In order to prevent this, we note that if the energy spectrum of the effective Hamiltonian Eq. (2.13) is symmetric around $E = 0$, it is possible to rewrite the thermodynamic potential isolating the Dirac sea contribution. One can namely write the kinetic part of Eq. (2.33) as

$$\begin{aligned}
\Omega_{kin} &= -N_f N_c T \sum_{E \gtrless 0} \log \left(2 \cosh \left(\frac{E - \mu}{2T} \right) \right) \\
&= -N_f N_c \sum_{E > 0} \left\{ E + T \log \left[\left(1 + \exp \left(-\frac{E - \mu}{T} \right) \right) \left(1 + \exp \left(-\frac{E + \mu}{T} \right) \right) \right] \right\} \\
&\equiv -N_f N_c \sum_{E > 0} [f_{vac}(E) + f_{med}(E; T, \mu)] ,
\end{aligned} \tag{2.35}$$

where only the first T and μ -independent term f_{vac} is divergent. The f_{med} term describes the medium contributions to the thermodynamic potential, and is finite since temperature and chemical potential provide a natural cutoff for it. This becomes evident if one considers the zero temperature limit, where the medium term contains a step function ending at $E = \mu$:

$$f_{med} = T \log \left[\left(1 + \exp \left(-\frac{E - \mu}{T} \right) \right) \left(1 + \exp \left(-\frac{E + \mu}{T} \right) \right) \right] \xrightarrow{T \rightarrow 0} (\mu - E) \theta(\mu - E) . \tag{2.36}$$

Our preferred regularization scheme throughout this thesis is a Pauli-Villars regularization which we apply only to the diverging vacuum term. This amounts to the replacement [77]

$$f_{vac}(x) \rightarrow f_{PV}(x) = \sum_{j=0}^3 c_j \sqrt{x^2 + j\Lambda^2} , \tag{2.37}$$

with $c_0 = 1$, $c_1 = -3$, $c_2 = 3$, $c_3 = -1$ and a regulator Λ .

The regularized thermodynamic potential will therefore be given by

$$\Omega_{kin} = -N_f N_c \sum_{E > 0} [f_{PV}(E) + f_{med}(E; T, \mu)] . \tag{2.38}$$

It is well known that most covariant regularization schemes result in rather small constituent quark masses, which may lead to unphysical features. Because of this, we will fix our parameters to the pion decay constant in the chiral limit but instead of the value of the vacuum chiral condensate, we will enforce a given constituent quark mass.

For completeness, we will discuss different regularization schemes, as well as more details on the parameter fitting, in appendix C.

2.3. The Quark-Meson model

Since the NJL model requires to specify a regularization scheme which can in principle affect the results, aside from investigating different regularization schemes, as an additional cross-check we will also consider a slightly different model which shares many features with it, but is (at least in principle) renormalizable. In this section we therefore introduce the Quark-meson(QM) model [84, 85], which is described by the Lagrangian density

$$\mathcal{L}_{QM} = \bar{\psi} (i\gamma^\mu \partial_\mu - g(\sigma + i\gamma_5 \tau^a \pi^a)) \psi - U(\sigma, \pi^a), \quad (2.39)$$

where the meson kinetic contributions together with the “mexican hat” potential driving the spontaneous breaking of chiral symmetry are contained in

$$U(\sigma, \pi^a) = -\frac{1}{2} (\partial_\mu \sigma \partial^\mu \sigma + \partial_\mu \pi^a \partial^\mu \pi^a) + \frac{\lambda}{4} (\sigma^2 + \pi^a \pi^a - v^2)^2 - c\sigma. \quad (2.40)$$

Here ψ is again a $4N_f N_c$ -dimensional quark spinor, σ the scalar field of the sigma meson and π^a the pseudo-scalar fields of the pion triplet. In mean-field approximation we treat the fields σ and π^a as classical and replace them by their expectation values [85, 86]. We can then use low-energy relations to connect the parameters c , g , λ and v^2 with hadronic observables. For the thermodynamic potential in mean-field approximation we only include the contributions of the fermionic fluctuations and approximate

$$\begin{aligned} \Omega_{QM}(T, \mu; \sigma(\mathbf{x}), \pi^a(\mathbf{x})) &= -\frac{T}{V} \log \int \mathcal{D}\bar{\psi} \mathcal{D}\psi \mathcal{D}\sigma \mathcal{D}\pi^a \exp \left(\int_{x \in [0, \frac{1}{T}] \times V} (\mathcal{L}_{QM} + \mu \bar{\psi} \gamma^0 \psi) \right) \\ &\xrightarrow{\text{MF}} -\frac{TN_c}{V} \sum_n \text{Tr}_{D,f,V} \text{Log} \left(\frac{1}{T} (i\omega_n + \mathcal{H}_{QM} - \mu) \right) \\ &\quad + \frac{1}{V} \int_V d\mathbf{x} U(\sigma(\mathbf{x}), \pi^a(\mathbf{x})), \end{aligned} \quad (2.41)$$

where $\sigma(\mathbf{x})$ and $\pi^a(\mathbf{x})$ are non-vanishing expectation values of the respective fields. Limiting ourselves, as done previously, to cases with $\pi^1(\mathbf{x}) = \pi^2(\mathbf{x}) = 0$, the Hamiltonian reads

$$\mathcal{H}_{QM} = -i\gamma^0 \gamma^i \partial_i + \gamma^0 (g\sigma(\mathbf{x}) + ig\gamma^5 \tau^3 \pi^3(\mathbf{x})), \quad (2.42)$$

and we have to evaluate the same functional trace-logarithm as in the case of the NJL model, but now with the identification $M(\mathbf{x}) = g(\sigma(\mathbf{x}) + i\pi^3(\mathbf{x}))$.

As previously mentioned, the QM model is renormalizable, which means that the divergences in the functional trace-logarithm can be absorbed by the model parameters. Instead of a proper renormalization [87] we will however follow Refs. [85, 86], where it has been assumed that the vacuum contributions can be well approximated by $\frac{1}{V} \int_V U(\sigma(\mathbf{x}), \pi^a(\mathbf{x}))$ with the parameters directly adopted to phenomenology. As a result, we can evaluate the thermodynamic potential on the same level as for the NJL model.

3. Diagonalization of the Hamiltonian: zero temperature results

As outlined in the previous chapter, the evaluation of the model thermodynamic potential basically boils down to obtaining the spectrum of the mean field Hamiltonian (Eq. (2.13)). As it turns out, the diagonalization of \mathcal{H} for an arbitrary spatial dependence of the mean fields is a non-straightforward task, and in order to proceed several simplifying assumptions will be required.

In particular, to render the problem numerically accessible we will focus on one- and two-dimensional spatial modulations of the chiral condensate. These lower-dimensional structures are simpler to implement due to the Lorentz-invariance of the system which allows to work with dimensionally reduced effective Hamiltonians. In the present chapter, the practical implementation of the diagonalization procedure will be outlined and numerical results at zero temperature will be discussed.

All results obtained in this section are obtained in the chiral limit $m = 0$ and regularized using the Pauli-Villars prescription described in Sec. 2.2.4, with a parameter set fitted to obtain a vacuum constituent quark mass of $M_{vac} = 300$ MeV (values are reported in Appendix D.1).

3.1. Homogeneous chiral condensates

As a starting point which can be used as comparison with our results for inhomogeneous phases, let us briefly review the well established homogeneous case. If the chiral condensate is spatially constant, its Fourier expansion Eq. (2.28) will obviously contain only the zeroth term, all the other coefficients being zero:

$$M_{k_n} = M_0 \delta_{\mathbf{k}_n, 0}. \quad (3.1)$$

The Hamiltonian is then diagonal in momentum space, a generic element on its diagonal being given by

$$\mathcal{H}_{\mathbf{p}, \mathbf{p}} = (\gamma^0 \boldsymbol{\gamma} \cdot \mathbf{p} + \gamma^0 M_0). \quad (3.2)$$

The eigenvalues of one of these 4 by 4 blocks on the momentum diagonal $\mathcal{H}_{\mathbf{p}, \mathbf{p}}$ are $E_{\mathcal{H}}(\mathbf{p}) = \pm \sqrt{\mathbf{p}^2 + M^2}$, twice degenerate (for brevity we renamed M_0 to M). This is the standard dispersion relation obtained in NJL, describing a system of free massive quasiparticles (see Fig. 2.1). The thermodynamic potential is then given by

$$\Omega(T, \mu) = -N_f N_c T \sum_{E_{\mathcal{H}}(p)} \log \left[2 \cosh \left(\frac{E_{\mathcal{H}} - \mu}{2T} \right) \right] + \frac{1}{4G_S V} \int_V |M|^2, \quad (3.3)$$

Switching from the energy sum to a momentum integral we obtain the familiar expression

$$\begin{aligned} \Omega(T, \mu; M)_{homog} = & -2N_f N_c \int \frac{d^3 p}{(2\pi)^3} \{ \sqrt{\mathbf{p}^2 + M^2} + T \log \left[1 + \exp \left(-\frac{\sqrt{\mathbf{p}^2 + M^2} - \mu}{T} \right) \right] \\ & + T \log \left[1 + \exp \left(-\frac{\sqrt{\mathbf{p}^2 + M^2} + \mu}{T} \right) \right] \} + \frac{M^2}{4G_S}, \end{aligned} \quad (3.4)$$

which is the standard result for homogeneous phases in NJL.

We can rewrite Eq. (3.4) in a way that will be useful for later comparison. For this, we change integration variable from momentum to energy $E = \sqrt{\mathbf{p}^2 + M^2}$. We arrive then at

$$\Omega(T, \mu, M) = -N_f N_c \int_0^\infty dE \rho_{hom}(E) [f_{vac}(E) + f_{med}(E; T, \mu)] + \frac{M^2}{4G_S}, \quad (3.5)$$

where f_{vac} and f_{med} have been defined in Sec. 2.2.4 and we introduced an effective density of states for homogeneous phases ρ_{hom} , given by

$$\rho_{hom}(E) = \frac{1}{\pi^2} \theta(E - M) E \sqrt{(E^2 - M^2)}, \quad (3.6)$$

with the step function reflecting the presence of a gap M in the energy spectrum (cf. Fig. 2.1). At this point, we can regularize by substituting $f_{vac} \rightarrow f_{PV}$ as outlined in Sec. 2.2.4. Results for homogeneous phases are presented in Fig. 3.1: at zero temperature, the value of the chiral condensate (or equivalently of the constituent quark mass) remains constant as a function of chemical potential until the value $\mu = M$ is reached. Beyond that value, a Fermi sea of massive quarks starts forming and medium effects lower the value of the constituent mass. Soon chiral restoration is reached through a first-order phase transition, where the chiral condensate value jumps to zero. This is the standard scenario for chiral restoration: in presence of a Fermi sea, the excitation of antiquarks becomes more and more energetically costly, until the formation of a chiral condensate is eventually disfavored.

3.2. Inhomogeneous chiral condensates: general approach

The numerical diagonalization of \mathcal{H} for an arbitrary spatially modulated chiral condensate is a highly non-trivial task. Since the mean-field Hamiltonian has to be diagonalized in momentum space, one is in principle dealing with an infinite matrix with a continuous

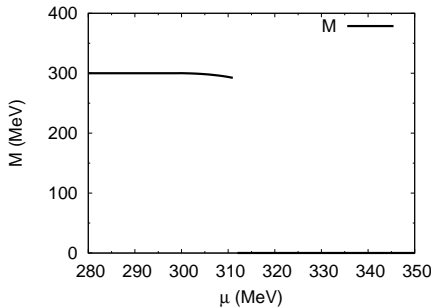


Figure 3.1.: Results for the value of the constituent quark mass as a function of chemical potential at $T = 0$ for an homogeneous chiral condensate

set of elements, and the nested Dirac structure effectively quadruples the size of the problem. The numerical implementation of such a diagonalization is as such not completely straightforward.

In order to be able to perform our analysis, we therefore follow the procedure developed in [38] in the similar context of crystalline color-superconductivity and assume that the spatially modulated chiral condensate forms a periodic structure in coordinate space. This allows us to exploit the symmetries of the system and in particular Bloch's theorem to factorize the momentum integration in the expression for the thermodynamic potential. Indeed, for an arbitrary periodic modulation we can define a reciprocal lattice (RL) in momentum space, and for quarks scattering with this crystalline condensate we know that momenta which do not differ by an element of the RL will not be coupled (a more detailed discussion of this property is shown in Appendix H). This in turn implies that \mathcal{H} can be decomposed into a block diagonal form, where each block $\mathcal{H}(k)$ is labeled by an element of the first Brillouin zone (BZ):

$$\mathcal{H} = \sum_{k \in BZ} \mathcal{H}(k). \quad (3.7)$$

It is then possible to decompose the eigenvalue sum in Eq. (2.33) into a momentum integration over the BZ times a sum over the discrete eigenvalues of each block [38]. It is worth noting that $\mathcal{H}(k)$ is still infinite in momentum space, and a numerical cutoff will have to be introduced. This will be discussed in more detail in Appendix I.

In the following, we will briefly outline the dimensional reduction procedure and present results for different kinds of modulations of the chiral condensate. A recent analysis using Ginzburg-Landau (GL) arguments has shown that close to the location of the chiral critical point, the preferred shape for the chiral condensate is that of a one-dimensional crystal [88]. We will instead focus on what happens at zero temperature, where GL analyses are unable to provide reliable results. Another GL prediction states that all possible kinds of inhomogeneous modulations should share a common phase transition line to the chirally restored phase, as long as the transition is a second-order one [89]. We will also check

numerically the validity of this statement against our results.

3.2.1. Lower-dimensional modulations

For general periodic structures, although the numerical diagonalization procedure is now in principle straightforward, its practical implementation still turns out to be computationally demanding. In order to simplify the problem, we therefore limit the generality of our ansatz Eq. (2.28) to lower-dimensional modulations. In this case, the momentum integration required for the evaluation of the thermodynamic potential may be split into the parts \mathbf{p}_{\parallel} along the direction of the modulation and \mathbf{p}_{\perp} perpendicular to it. One thus obtains, for a d -dimensional modulation,

$$\Omega_{kin} = -N_f N_c \int \frac{d^{3-d} p_{\perp}}{(2\pi)^{3-d}} \frac{1}{V_{\parallel}} \sum_E T \log \left[2 \cosh \left(\frac{E(\mathbf{p}_{\perp}, \mathbf{p}_{\parallel}) - \mu}{2T} \right) \right], \quad (3.8)$$

where $E(\mathbf{p}_{\perp}, \mathbf{p}_{\parallel})$ are the eigenvalues of $\mathcal{H}(\mathbf{p} = \mathbf{p}_{\parallel} + \mathbf{p}_{\perp})$. The expression for Ω_{kin} still contains the eigenvalues E of the full effective Hamiltonian in three spatial dimensions. Following [90], we will show that the problem can however be dimensionally reduced for lower-dimensional modulations by help of Lorentz symmetry. For this, suppose we have a representation $S(\Lambda)$ for the Lorentz transformation Λ that acts on the momentum operator of free spinors $P^{\mu} = (H, P_i)^{\mu}$ as

$$S(\Lambda) P^{\mu} S^{-1}(\Lambda) = \Lambda^{\mu}_{\nu} P^{\nu}. \quad (3.9)$$

If the system is translationally invariant in one or more directions, the corresponding momenta P_{\perp} commute with the Hamiltonian \mathcal{H} and we can label its eigenstates also by \mathbf{p}_{\perp} , the eigenvalue of P_{\perp} . Now take $\psi_{\lambda,0}$ to be the eigenvector with $\mathcal{H}\psi_{\lambda,0} = \lambda\psi_{\lambda,0}$ and $P_{\perp}\psi_{\lambda,0} = 0$, Λ^{μ}_{ν} to be the Lorentz transformation that boosts $(\lambda, \mathbf{0})^{\mu}$ to $\left(\lambda\sqrt{1 + \mathbf{p}_{\perp}^2/\lambda^2}, \mathbf{p}_{\perp}\right)^{\mu}$ and define

$$\psi_{\lambda\sqrt{1+\mathbf{p}_{\perp}^2/\lambda^2}, \mathbf{p}_{\perp}} = \left(\sqrt{1 + \mathbf{p}_{\perp}^2/\lambda^2}\right)^{-\frac{1}{2}} S^{-1}(\Lambda) \psi_{\lambda,0}. \quad (3.10)$$

The prefactor implements the proper normalization for the conventional choice of $S(\Lambda)$ [91] and it is straightforward to check that

$$P^{\mu} \psi_{\lambda\sqrt{1+\mathbf{p}_{\perp}^2/\lambda^2}, \mathbf{p}_{\perp}} = \left(\lambda\sqrt{1 + \mathbf{p}_{\perp}^2/\lambda^2}, \mathbf{p}_{\perp}\right)^{\mu} \psi_{\lambda\sqrt{1+\mathbf{p}_{\perp}^2/\lambda^2}, \mathbf{p}_{\perp}}. \quad (3.11)$$

Therefore the whole eigenvalue spectrum can be constructed from the subspace spanned by $\{\psi_{\lambda,0}\}$ and for the kinetic part of the thermodynamic potential we obtain

$$\Omega_{kin}(T, \mu; M(\mathbf{x})) = -T N_f N_c \frac{1}{V_{\parallel}} \sum_{\lambda} \int \frac{d\mathbf{p}_{\perp}}{(2\pi)^{d_{\perp}}} \log \left(2 \cosh \left(\frac{\lambda\sqrt{1 + \mathbf{p}_{\perp}^2/\lambda^2} - \mu}{2T} \right) \right) \quad (3.12)$$

In general we are therefore able to constrain ourselves to a lower dimensional model if we want to determine the quasi-particle spectrum for an inhomogeneous phase with a lower dimensional modulation: the eigenvalue spectrum for the full 3+1-dimensional problem can be obtained by simply boosting the eigenvalues of a dimensionally reduced Hamiltonian $\mathcal{H}(\mathbf{p}_\perp = 0)$. If the lower-dimensional problem is still not analytically treatable, we can project again the p_\parallel momenta onto the BZ for a given lattice structure and rewrite the kinetic term as

$$\Omega_{kin} = -N_f N_c \int \frac{d^{3-d} p_\perp}{(2\pi)^{3-d}} \int_{BZ} \frac{d^d k}{(2\pi)^d} \sum_E T \log \left[2 \cosh \left(\frac{E(\mathbf{p}_\perp, \mathbf{k}) - \mu}{2T} \right) \right], \quad (3.13)$$

where d is the dimension of the spatial modulation, \mathbf{k} labels the BZ momenta, $E(\mathbf{p}_\perp, \mathbf{k})$ are the boosted eigenvalues of the dimensionally reduced $\mathcal{H}(\mathbf{k})$.

3.3. One-dimensional modulations

As shown in the previous section, if we restrict ourselves to lower-dimensional spatial modulations of the chiral condensate, the diagonalization of the mean-field Hamiltonian can be significantly simplified. The simplest case one can consider at this point is obviously a one-dimensional modulation of the chiral order parameter:

$$M(\mathbf{x}) \rightarrow M(z). \quad (3.14)$$

The kind of system we are considering therefore features a chiral condensate varying in one spatial direction only, while remaining constant along the two transverse ones. This can be interpreted as some kind of “lasagne” phase, similar to the one considered in the context of nuclear matter studies, with constant slices in the xy plane and modulations in the z direction only.

In coordinate space, the effective dimensionally reduced Hamiltonian for an arbitrary one-dimensional modulation is given by

$$\mathcal{H}_{1D} = \begin{pmatrix} i\partial_z & M(z) & & \\ M(z)^* & -i\partial_z & M(z) & \\ & -i\partial_z & i\partial_z & \\ M(z)^* & M(z)^* & & \end{pmatrix}. \quad (3.15)$$

In the following sections we will consider different kinds of one-dimensional modulations, diagonalize the corresponding Hamiltonian and minimize the thermodynamic potential with respect to the variational parameters characterizing the shape of the chiral condensate.

3.3.1. Chiral density wave

The simplest possible one-dimensional shape for the chiral order parameter is given by a single plane wave (the so-called “Chiral density wave”, CDW), whose wave vector \mathbf{Q} can be taken to point in the z direction without loss of generality: $\mathbf{Q} = Q\hat{e}_z$. This kind of ansatz is analogous to the Fulde-Ferrell solutions introduced in the context of (color-) superconductivity, and can be implemented in our analysis by limiting the Fourier expansion for the order parameter to the first term only:

$$M(z) = \sum_{n=1} M_n e^{inQz} = M_1 e^{iQz}. \quad (3.16)$$

This solution is therefore characterized by the magnitude of its wave vector Q and by its amplitude M_1 . In the simpler case of a one-dimensional system, in order to minimize the energy the wave number of the modulation would equal the diameter of the Fermi sphere [52, 53, 54]. This exact relation is lost in higher dimensions, although the wave vector is still expected to be of the same order of magnitude as the chemical potential.

The thermodynamic potential for this modulation is given by

$$\Omega(T, \mu; Q, M_1) = -N_f N_c \int \frac{d^2 p_\perp}{(2\pi)^2} \int_0^Q \frac{dk}{2\pi} \sum_{\lambda_k > 0} \{f_{vac}(E) + f_{med}(E; T, \mu)\} + \frac{M_1^2}{4G_S}, \quad (3.17)$$

with $E = \text{sgn}(\lambda_k) \sqrt{\lambda_k^2 + p_\perp^2}$ boosted eigenvalue, λ_k being the eigenvalue of the dimensionally reduced Hamiltonian

$$\mathcal{H}_{p_n, p_m}^{CDW} = \gamma^0 [\gamma^z p_n^z \delta_{p_n, p_m} + M_1 \delta_{p_n, p_m + Q}], \quad (3.18)$$

where all momenta are now one-dimensional ones along the z direction.

For the particular case of the chiral density wave, an analytical expression for the eigenvalue spectrum has been obtained [54, 49], so that no numerical diagonalization is required. In particular, it is possible to encode its shape in a spectral density function $\rho_{CDW}(E)$. The thermodynamic potential can thus be written, similarly to Eq. (3.5), as

$$\begin{aligned} \Omega_{kin} &= -N_f N_c \sum_{E>0} [f_{vac}(E) + f_{med}(E; T, \mu)] \\ &= -N_f N_c \int_0^\infty dE \rho_{CDW}(E) [f_{vac}(E) + f_{med}(E; T, \mu)], \end{aligned} \quad (3.19)$$

where E are the boosted energies for the full 3+1D system and the density of states is given by

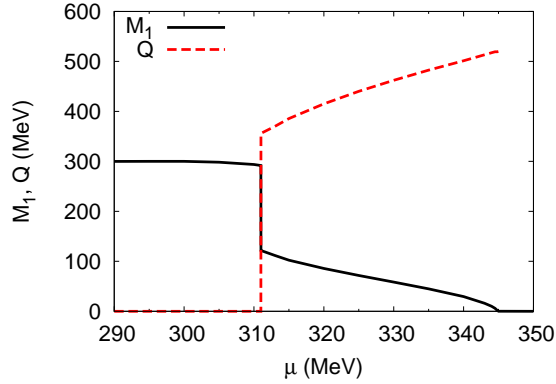


Figure 3.2.: Results of the minimization of the thermodynamic potential for the variational parameters Q and M_1 characterizing the CDW modulation.

$$\begin{aligned} \rho_{CDW}(E) = & \frac{E}{2\pi^2} \left\{ \theta(E - \tilde{Q} - M_1) \sqrt{(E - \tilde{Q})^2 - M_1^2} \right. \\ & + \theta(E - \tilde{Q} + M_1) \theta(E + \tilde{Q} - M_1) \sqrt{(E + \tilde{Q})^2 - M_1^2} \\ & \left. + \theta(\tilde{Q} - M_1 - E) \left(\sqrt{(E + \tilde{Q})^2 - M_1^2} - \sqrt{(E - \tilde{Q})^2 - M_1^2} \right) \right\}, \quad (3.20) \end{aligned}$$

where for compactness we introduced $\tilde{Q} = 2Q$.

The results of the minimization of the thermodynamic potential at $T = 0$ for the variational parameters M_1 and Q are shown in Fig. 3.2. It is possible to see that the inhomogeneous phase kicks in through a first-order phase transition at a given chemical potential slightly smaller than the one at which the chiral restoration for homogeneous phases would occur. At that given value, the free energy associated with a nonzero Q (which turns out to be of the same order as μ , as expected) becomes lower than the one of the homogeneous phase, for which $Q = 0$. As a result, chiral restoration occurs then at a higher chemical potential compared to homogeneous phases, and is realized via a second order transition as the amplitude of the order parameter gradually melts to zero.

3.3.2. Sinusoidal modulation

As a next step, we can build up the simplest real one-dimensional modulation by considering the sum of the first positive and negative harmonics, both characterized by the same amplitude ($M_1 = M_{-1}$):

$$M(z) = \sum_{n=\pm 1} M_n e^{inQz} = 2M_1 \cos(Qz) \equiv M \cos(Qz). \quad (3.21)$$

The effective Hamiltonian is then

$$\mathcal{H}_{p_n, p_m}^{cos} = \gamma^0 [\gamma^z p_n^z \delta_{p_n, p_m} + M_1 \delta_{p_n, p_m + Q} + M_1 \delta_{p_n, p_m - Q}] . \quad (3.22)$$

Unlike for the CDW ansatz, in this case no analytical expression for the spectral density could be found, so that \mathcal{H} had to be diagonalized numerically in Dirac and momentum space (details on the calculations are presented in Appendix I).

Numerical results of the minimization of the thermodynamic potential are presented in Fig. 3.3. It is possible to see that the order parameters have a very similar behavior to those for the chiral density wave, although for the cosine the onset of the inhomogeneous phase occurs at a slightly lower value of chemical potential. Chiral restoration occurs again via a second order phase transition, occurring (at least within our numerical precision of around 0.5 MeV) at the same value of chemical potential as for the CDW modulation, consistently with GL predictions [89].

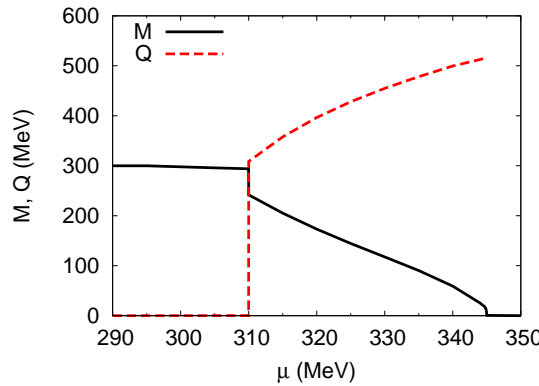


Figure 3.3.: Results of the minimization of the thermodynamic potential for the variational parameters Q and $M = 2M_1$ characterizing the real sinusoidal modulation.

3.3.3. Solitonic solutions

For the case of real one-dimensional modulations of the chiral order parameter, it is possible to introduce a more general ansatz which does not require a numerical diagonalization of the model Hamiltonian. For this, we first note that \mathcal{H}_{1D} (Eq. (3.15)) can be block-diagonalized into

$$\mathcal{H}'_{1D} = \begin{pmatrix} H_{GN}(M(z)) & \\ & H_{GN}(M(z)^*) \end{pmatrix} , \quad (3.23)$$

where

$$H_{GN}(M(z)) = \begin{pmatrix} -i\partial_z & M(z) \\ M(z)^* & i\partial_z \end{pmatrix} . \quad (3.24)$$

This means that the model Hamiltonian can be rewritten as a direct sum of two Hamiltonians (Eq. (3.24)), which are formally identical to that of the 1+1-dimensional chiral Gross-Neveu model. In turn, this suggests that we can reuse specific solutions already investigated in detail when studying lower-dimensional models, and analytical expressions for the eigenvalue spectrum of the problem can be obtained.

In particular, we will focus on a real ansatz for the order parameter, which can be expressed in terms of Jacobi elliptic functions:

$$M(z) = \Delta\nu \frac{\text{sn}(\Delta z|\nu)\text{cn}(\Delta z|\nu)}{\text{dn}(\Delta z|\nu)}. \quad (3.25)$$

This kind of solution is characterized by its amplitude Δ and by the so-called elliptic modulus ν , which determines the shape of the modulation (a brief reminder on elliptic functions is presented in Appendix E).

For this particular kind of solution, the pseudoscalar part of the chiral condensate is zero and the density of states can be calculated starting from the eigenvalue spectrum of the GN model [45] and reads (more details on the calculation are presented in appendix E.1)

$$\begin{aligned} \rho_{\text{soliton}}(E) = \frac{E\Delta}{\pi^2} \left\{ \right. & \theta(\sqrt{\tilde{\nu}}\Delta - E) \left[\mathbf{E}(\tilde{\theta}|\tilde{\nu}) + \left(\frac{\mathbf{E}(\nu)}{\mathbf{K}(\nu)} - 1 \right) \mathbf{F}(\tilde{\theta}|\tilde{\nu}) \right] \\ & + \theta(E - \sqrt{\tilde{\nu}}\Delta)\theta(\Delta - E) \left[\mathbf{E}(\tilde{\nu}) + \left(\frac{\mathbf{E}(\nu)}{\mathbf{K}(\nu)} - 1 \right) \mathbf{K}(\tilde{\nu}) \right] \\ & \left. + \theta(E - \Delta) \left[\mathbf{E}(\theta|\tilde{\nu}) + \left(\frac{\mathbf{E}(\nu)}{\mathbf{K}(\nu)} - 1 \right) \mathbf{F}(\theta|\tilde{\nu}) + \frac{\sqrt{(E^2 - \Delta^2)(E^2 - \tilde{\nu}\Delta^2)}}{E\Delta} \right] \right\}, \end{aligned} \quad (3.26)$$

where \mathbf{K} and \mathbf{F} are the complete and incomplete elliptic integrals of 1st kind, respectively, and \mathbf{E} are the (complete or incomplete) elliptic integrals of 2nd kind. Furthermore we introduced the notations $\tilde{\nu} = 1 - \nu$, $\tilde{\theta} = \arcsin(E/(\sqrt{\tilde{\nu}}\Delta))$, and $\theta = \arcsin(\Delta/E)$.

The thermodynamic potential can therefore be cast into

$$\begin{aligned} \Omega(T, \mu; \Delta, \nu) = & -N_f N_c \int_0^\infty dE \rho_{\text{soliton}}(E) [f_{\text{vac}}(E) + f_{\text{med}}(E; T, \mu)] \\ & + \frac{1}{4G_S L} \int_0^L dz |M(z)|^2, \end{aligned} \quad (3.27)$$

where $L = 4\mathbf{K}(\nu)/\Delta$ is the period of the modulation.

Results on the parameters Δ and ν are shown on the left side of Fig. 3.4. Although the onset of the inhomogeneous phase occurs at a similar (albeit slightly lower) value of chemical potential compared to the other one-dimensional modulations considered, the nature of the phase transition is different. This can be seen by looking at the shape of the solutions obtained, and in particular by observing that for $\nu = 1$ the mass modulation

of Eq. (3.25) becomes a hyperbolic tangent. This particular shape has an infinite period and features a single kink at $z = 0$, and is as such degenerate with the homogeneous solutions in the thermodynamic limit. At the onset of the inhomogeneous phase, the elliptic modulus ν varies smoothly from 1 to a slightly smaller value as infinitely distant solitons come close together, and the transition is therefore second order. On the right side of the inhomogeneous window, chiral symmetry is again restored via a second order phase transition as the amplitude of the order parameter gradually melts to zero (a more detailed discussion of the behavior of solitonic order parameters will be given in Sec. 4.2). Since the parameter dependence of the chiral condensate for the solitonic solutions is different from the previous modulations considered, a naive comparison of the results for the order parameters Δ and ν might be misleading. In order to provide a better comparison with the solutions calculated in the previous sections, we therefore show on the right side of Fig. 3.4 the combination $\Delta\nu$, which may be roughly interpreted as an amplitude for the solitonic modulations¹ (cfr. Eq. (3.25)), and a wave vector $Q = 2\pi/L$ associated with the period of the elliptic functions, $L = 4\mathbf{K}(\nu)/\Delta$. There it can be seen that Q has a steep but continuous increase from 0 to a finite value at the onset of the inhomogeneous phase, reflecting the nature of the second-order phase transition.

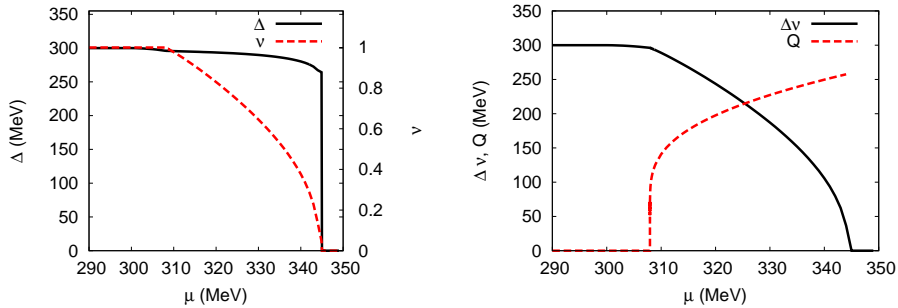


Figure 3.4.: Left: Results of the minimization of the thermodynamic potential for the variational parameters Δ and ν characterizing the solitonic solutions. Right: combination $\Delta\nu$ and wave vector $Q = 2\pi/L$.

3.4. Two-dimensional modulations

Having considered several one-dimensional modulations, we now move on to two-dimensional structures. Without loss of generality, we assume the chiral condensate to vary in the xy -plane and to be constant in the z -direction. The corresponding dimensionally-reduced effective Hamiltonian reads

¹Another possible quantity which may be considered is $\sqrt{\langle M(z)^2 \rangle}$, which will be shown in chapter 4

$$\mathcal{H}_{2D} = \begin{pmatrix} i\partial_x + \partial_y & M(x, y) & & \\ i\partial_x - \partial_y & & M(x, y) & \\ M(x, y)^* & & -i\partial_x - \partial_y & \\ & M(x, y)^* & -i\partial_x + \partial_y & \end{pmatrix}, \quad (3.28)$$

which in momentum space becomes

$$\mathcal{H}_{2D} = \begin{pmatrix} -p_x + ip_y & M & & \\ -p_x - ip_y & & M & \\ M^* & & p_x - ip_y & \\ & M^* & p_x + ip_y & \end{pmatrix}, \quad (3.29)$$

where we omitted the Kronecker deltas stating which momenta are coupled since here we are mainly interested in showing the Dirac structure. It is intended of course that the blocks containing M will in general be outside the momentum diagonal, and their position will depend on the type of modulation considered. This Hamiltonian can be block-diagonalized only for real $M(x, y)$, i.e. for $\phi_P(\mathbf{x}) = 0$ [90]. In this case we can cast the problem into the form

$$\mathcal{H}'_{2D} = \begin{pmatrix} M & -p_x - ip_y & & \\ -p_x + ip_y & -M & & \\ & & -M & -p_x - ip_y \\ & & -p_x + ip_y & M \end{pmatrix}. \quad (3.30)$$

Unlike for the one-dimensional case, in two spatial dimensions different crystalline shapes may be realized. We will therefore consider different lattice geometries and assume the mass functions to have simple symmetric shapes consistent with these structures (details in Appendix H.1). The Fourier expansion of the order parameter is given by

$$M(x, y) = \sum_{m,n} M_{m,n} e^{i\mathbf{q}_{m,n} \cdot \mathbf{x}}, \quad (3.31)$$

where the two indices m and n label the two-dimensional momenta of the reciprocal lattice. Although the diagonalization procedure for two-dimensional modulations is in principle straightforward as for the one-dimensional ones, it turns out to be computationally much more demanding, and numerical uncertainties are bigger (more details are presented in Appendix I).

3.4.1. Egg carton

The first two-dimensional case we will consider is a square lattice with a unit cell spanned by two perpendicular vectors of length a in x and y direction. The corresponding elements of the RL are then given by $\mathbf{q}_{m,n} = Q(m\hat{e}_x + n\hat{e}_y)$ with $Q = 2\pi/a$ and integers m and n . While the general mass function consistent with this lattice structure would be given by Eq. (3.31) with arbitrary Fourier coefficients $M_{m,n}$, we restrict ourselves to a simple ansatz for a real symmetric mass function with a small number of non-vanishing

Fourier coefficients. Specifically we choose $M_{1,1} = M_{1,-1} = M_{-1,1} = M_{-1,-1} = M/4$ and $M_{m,n} = 0$ in all other cases. This yields

$$M(x, y) = M \cos(Qx) \cos(Qy), \quad (3.32)$$

which has an egg-carton-like shape (see Fig. 3.5, left) and is symmetric under discrete rotations by $\pi/2$.

Results for the numerical minimization in the parameters Q and M are shown on the right side of Fig. 3.5. It is possible to see how the variational parameters for this kind of two-dimensional modulation behave rather similarly to those associated with the simple one-dimensional structures previously considered. In particular, the onset to the inhomogeneous phase where the wave vector Q jumps to a finite value via a first order phase transition lies at a value of chemical potential which is very close² to the one found for the one-dimensional solutions. Once again, as expected from GL arguments, the second-order chiral restoration transition is exactly at the same chemical potential value as for the one-dimensional modulations.

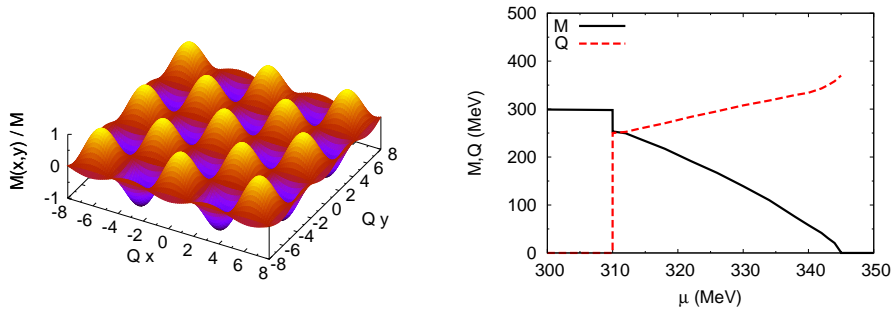


Figure 3.5.: “Egg-carton” modulation, Eq. (3.32). Left: shape of the mass function $M(x, y)$ in coordinate space. Right: results of the numerical minimization of the thermodynamic potential for the variational parameters Q and M .

3.4.2. Honeycomb

The second case we consider is a mass function with hexagonal symmetry. Here we start from a unit cell spanned by two vectors of length a , enclosing an angle of $\pi/3$. Choosing the first one to be aligned with the x -axis, the elements of the RL are given by $\mathbf{q}_{m,n} = Q(m\hat{e}_x + \frac{2n-m}{\sqrt{3}}\hat{e}_y)$, with integers m and n , and $Q = 2\pi/a$ as before. For the mass function we choose $M_{m,n} = M/6$ on the corners of a regular hexagon, $(m, n) \in \{(1, 0), (-1, 0), (0, 1), (0, -1), (1, 1), (-1, -1)\}$, and $M_{m,n} = 0$ in all other cases. This yields

$$M(x, y) = \frac{M}{3} \left[2 \cos(Qx) \cos\left(\frac{1}{\sqrt{3}}Qy\right) + \cos\left(\frac{2}{\sqrt{3}}Qy\right) \right], \quad (3.33)$$

²The onsets of all the crystalline phases considered lie within a window of around 3 MeV in chemical potential, $\mu \sim 308 - 311$ MeV.

which is symmetric under discrete rotations by $\pi/3$ (see Fig. 3.6, left). Note that the normalization of the amplitude was chosen to match the homogeneous case $M(x, y) = M$ when Q goes to zero.

Results of the numerical minimization are presented in Fig. 3.6 right. Once again, the first-order onset of the inhomogeneous phase lies at a very similar value of chemical potential as for the other modulations considered, and, as expected, chiral restoration occurs at the same point as for the others.

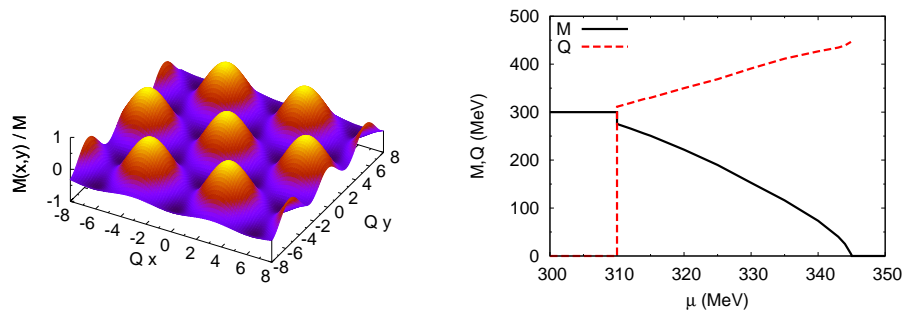


Figure 3.6.: Honeycomb ansatz, Eq. (3.33). Left: shape of the mass modulation in coordinate space. Right: results of the numerical minimization of the thermodynamic potential for the variational parameters Q and M .

3.5. Comparison of free energies

As seen from the numerical results of the minimization procedure presented in the previous sections, at zero temperature each crystalline structure considered in this chapter turned out to be favored over homogeneous solutions in a chemical potential window which is roughly the same for all modulations studied. We stress again that these calculations have been performed by enforcing each time a given shape of the spatial modulation, characterized by a set of variational parameters.

In order to determine what is the favored crystalline shape for the ground state of the model, it is therefore necessary to compare the free energies associated with the different modulations considered. The solution characterized by the lowest free energy (in our case, of thermodynamic potential Ω) at the minimum for a given value of chemical potential will be the thermodynamically favored one.

As a first step, we will confront the free energies of the different one-dimensional modulations we introduced. We will then successively investigate whether two-dimensional structures turn out to be favored over one-dimensional ones.

3.5.1. Most favored 1D modulation

We present in Fig. 3.7 the free energies associated with the different one-dimensional structures considered, together with the homogeneous counterparts. We always subtract

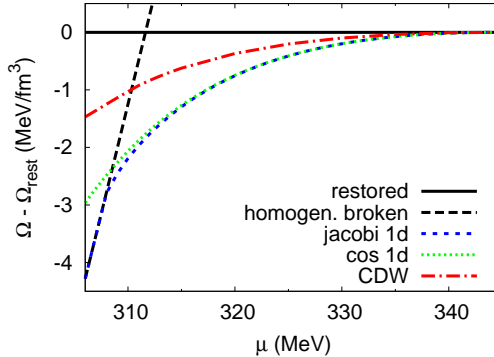


Figure 3.7.: Thermodynamic potential relative to the restored phase for the one-dimensional modulations of the chiral condensate at $T = 0$. The lowest free energy is found for the one-dimensional Jacobi elliptic function.

the free energy of the unbroken phase, so that all curves reach zero as chiral symmetry is restored.

From our results, it is possible to see that close to the onset of the inhomogeneous phase, the solitonic solutions introduced in Sec. 3.3.3 turn out to be the most favored. After a rather narrow chemical potential window they become however degenerate with the one-dimensional cosine discussed in Sec. 3.3.2. This should not come as a surprise, for Jacobi elliptic functions are a very general ansatz which can assume a sinusoidal shape as the elliptic modulus goes to zero, and this behavior of the free energies simply implies that the favored shape for the chiral condensate towards the chiral restoration transition is indeed that of a single cosine. We can therefore claim that, among all one-dimensional modulations considered, the soliton lattice introduced in Sec. 3.3.3 is the most favored.

On the other hand, another interesting results is that the complex CDW modulation discussed in Sec. 3.3.1 turns out to be always disfavored when compared to real ones throughout the whole inhomogeneous window. This might come as a surprise, since we have shown that the eigenvalue problem is reduced to that for the NJL_2 model, where the plane wave solution is believed to be the favored one [44]. In our case however, it can be seen that the Hamiltonian is actually a direct product of two NJL_2 ones, so that the structure of the thermodynamic potential becomes different. In particular, in [90] it has been shown in the context of a Ginzburg-Landau expansion that the NJL thermodynamic potential can be written as a sum of the NJL_2 thermodynamic potential and its conjugate. This particular structure leads to a bigger gain in free energy for a real sinusoidal modulation compared to the complex plane wave. We also note that the same behavior has been found in the context of superconductivity, where GL analyses have determined that the favored shape for the order parameter in higher dimensional systems is a real one as well [37, 40].

The results of Fig. 3.7 also allow us to comment on the importance of higher harmonics in our general Fourier analysis outlined in Eq. (2.28). Indeed, one can interpret the Jacobi

μ	ν	M_3/M_1	M_5/M_1	M_7/M_1	M_9/M_1
307.5	0.99999	-0.238386	0.080631	-0.0282258	0.00992179
308.0	0.99955	-0.129363	0.019598	-0.0029789	0.00045285
309.0	0.98920	-0.062376	0.004167	-0.0002784	0.00001861
310.0	0.97740	-0.046727	0.002295	-0.0001128	0.00000554
315.0	0.90805	-0.020578	0.000432	-0.0000091	0.00000002
320.0	0.83034	-0.011740	0.000132	-0.0000016	0.00000000

Table 3.1.: Values of the higher order nonzero harmonics for a generic one-dimensional modulation at different values of chemical potential close to the onset of the inhomogeneous phase ($T = 0$). Results are normalized to the value of the first harmonic ($n = 1$) in order to show their relative weights. Even harmonics are found to be zero.

elliptic function solutions as a very general kind of ansatz which can in principle include an arbitrarily high number of harmonics, and the comparison of free energies shows that the presence of higher frequencies plays a relevant role only in a narrow chemical potential window close to the onset of the inhomogeneous phase. This is clearly visible from table 3.1, where the results for the first harmonics obtained via a Fourier decomposition of the Jacobi elliptic functions at given values of chemical potential are shown.

It is nevertheless worth mentioning that, in spite of their marginal role for the free energy gain as a function of chemical potential, higher harmonics are crucial for producing the solitonic shapes which can allow for a smoother interpolation between the homogeneous chirally broken and the inhomogeneous phase. In that sense, their presence affects the order of the phase transition, which turns out to be second order only for the solitonic solutions. Finally, when looking at the shape of the density of the system (a thorough investigation will be presented in Sec. 4.2), it becomes clear that the narrow chemical potential window discussed above will result in a rather broad range for the average density of the system $\langle n \rangle$, so that an $\Omega(\langle n \rangle)$ plot will look rather different from Fig. 3.7.

3.5.2. Most favored: 1D vs 2D

This section is devoted to the comparison of the free energies associated with the two-dimensional shapes considered with the one obtained from the most favored one-dimensional solitonic solutions. From Fig. 3.8 it is possible to see that the “egg-carton” ansatz of Sec. 3.4.1 turns out to be favored over the hexagonal solution of Sec. 3.4.2. Both two-dimensional structures considered are however disfavored when compared to the one-dimensional solitons.

In this context it is instructive to introduce a rectangular structure, which interpolates continuously between a square lattice and a one-dimensional periodic modulation. Specifically, we can generalize the “egg-carton” ansatz of Eq. (3.32) by allowing for different wave vectors along the two perpendicular directions of the modulation, leading to

$$M(x, y) = M \cos(Q_x x) \cos(Q_y y), \quad (3.34)$$

which reduces to a single cosine varying in one spatial dimension when one of the two wave numbers goes to zero.

Starting from this ansatz, we minimize the thermodynamic potential with respect to the amplitude M for fixed wave numbers Q_x and Q_y , and then study the result as a function of Q_x and Q_y . Since we know already that the square-lattice solution along the line $Q_x = Q_y$ is disfavored against the one-dimensional cosine, we are mainly interested in the question whether the former corresponds to a local minimum or to a saddle point in the $Q_x - Q_y$ plane.

Our result for $\mu = 325$ MeV is presented in Fig. 3.9, showing that the solution at $Q_x = Q_y$ is a local minimum. One can also see that in the vicinity of the minimum the potential remains rather flat along the direction perpendicular to the line $Q_x = Q_y$. Going along this valley, we find two saddle points at $(Q_x, Q_y) \approx (175 \text{ MeV}, 400 \text{ MeV})$ and $(400 \text{ MeV}, 175 \text{ MeV})$. Unfortunately, the computing time rises strongly with decreasing wave numbers, so that we could not continue this analysis to values of Q_x or Q_y lower than 100 MeV. However, it is not hard to imagine how beyond the saddle points the valley approaches the absolute minima at vanishing Q_x or Q_y , corresponding to a one-dimensional cosine.

At this point, one may ask whether our observation that the two-dimensional crystalline structures are disfavored against the one-dimensional ones is caused by the restricted ansatz for the mass functions. Taking into account more Fourier modes would lead to additional variational parameters and could thus lower the free energy. It is however unlikely that this would change our results considerably. As seen in the previous section, the difference in free energy between the Jacobi elliptic function and the one-dimensional cosine is negligible in a large chemical-potential range and always much smaller than the difference to the two-dimensional solutions. We therefore expect that the corrections to the considered two-dimensional shapes are small as well.

In order to check this, we extend the simple ‘‘egg carton’’ ansatz (Eq. (3.32)) into

$$M(x, y) = \sum_{n=1}^3 M_n \cos(nQx) \cos(nQy). \quad (3.35)$$

The minimization of the thermodynamic potential with respect to the variational parameters (M_1, M_2, M_3, Q) leads, within numerical errors, to $M_2 = M_3 = 0$ throughout the whole inhomogeneous window. Although numerical uncertainties are more significant than for the one-dimensional case, it is safe to say that the inclusion of those higher harmonics considered above does not lead to an appreciable gain in free energy.

It appears therefore that the preferred shape for the model ground state features a one-dimensional soliton lattice formed by the chiral condensate which can be described in terms of Jacobi elliptic functions, as discussed in Sec. 3.3.3. It is worth recalling at this point that these are mean-field results, and that it is known that one-dimensional crystalline structures are washed out by thermal fluctuations at finite temperature [92]. This statement refers to the fact that the modulation is not rigid, but fluctuates locally, as

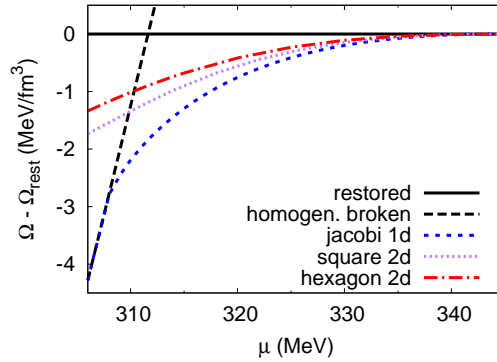


Figure 3.8.: Thermodynamic potential relative to the restored phase for the two-dimensional modulations of the chiral condensate and the solitonic one-dimensional solutions at $T = 0$. The lowest free energy is once again found for the one-dimensional Jacobi elliptic function.

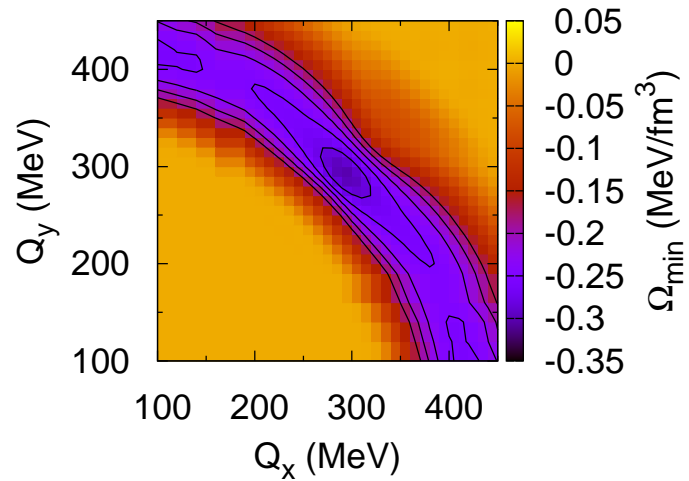


Figure 3.9.: Value of the thermodynamic potential at $T = 0$ and $\mu = 325$ MeV for a rectangular lattice, Eq. (3.34), as a function of Q_x and Q_y . At each point, Ω was minimized with respect to M .

in a liquid crystal. The system's spatially modulated nature is however still encoded in the behavior of long range correlations [93]. Keeping this property in mind, in the following we will nevertheless stick to our mean-field results and investigate in more details the properties of these solitonic solutions.

4. Solitonic solutions

Since, as shown on the previous chapter, the preferred shape for the chiral condensate among all those considered is the one-dimensional solitonic lattice expressed in terms of Jacobi elliptic functions, we present here some additional results obtained using this particular kind of ansatz. In particular, the full (T, μ) phase diagram and density profiles plots will be shown. The procedure for tackling these solitons away from the chiral limit will also be outlined.

We briefly recall that for this ansatz the mass modulation is given by

$$M(z) = \Delta\nu \frac{\text{sn}(\Delta z|\nu)\text{cn}(\Delta z|\nu)}{\text{dn}(\Delta z|\nu)}, \quad (4.1)$$

and is characterized by its amplitude Δ as well as by the elliptic modulus parameter ν .

Since the shape of the mass function now varies with ν , in order to provide some insight on the average magnitude of the chiral condensate for this kind of ansatz we show in Fig. 4.1 the chemical potential dependence of $\sqrt{\langle M(z)^2 \rangle}$ at $T = 0$. It is possible to see that the onset of the inhomogeneous phase is marked by a rapid drop in the average mass as infinitely spaced solitons come together in a very narrow window of chemical potential (see also Appendix E). Another visible feature from this plot is the presence of small medium effects before the onset of the inhomogeneous phase, as μ becomes bigger than the vacuum constituent quark mass $M_q = 300$ MeV and quarks start forming an homogeneous Fermi sea. In order to provide a more realistic description of the phase transition, it would perhaps be more desirable to jump from the vacuum directly into the inhomogeneous phase, a condition which can be achieved by tuning our parameters to obtain a slightly bigger vacuum constituent quark mass. This refitting will be pursued later on, for now we note that this effect is in any case rather small, and we expect that most of our results are qualitatively unaffected by it.

4.1. Phase diagram

In this section we investigate the model phase structure with the introduction of the solitonic modulations of the chiral condensate. For this, we extend the analysis of Sec. 3.3.3 to finite temperature and determine where the solitonic solutions are favored over the homogeneous ones. As can be seen in Fig. 4.2, when allowing for such solutions, an inhomogeneous “island” appears around the would-be first order phase transition line that was obtained when restricting to homogeneous phases only. It is worth noting that the location of this phase does not coincide with the spinodal region¹ appearing around

¹That is, the region where the model thermodynamic potential has different minima, associated with chirally broken and restored solutions.

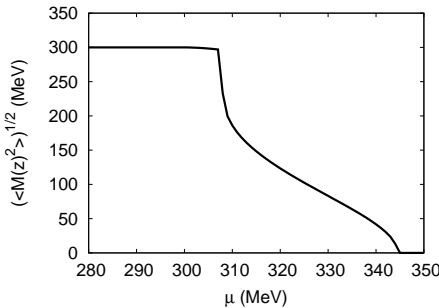


Figure 4.1.: $\sqrt{\langle M(z)^2 \rangle}$ for the solitonic ansatz of Eq. (4.1) as a function of μ for $T = 0$.

the first order transition line for homogeneous phases, although its size is affected by the strength of the chiral phase transition [90].

Contrary to previous studies on simpler modulations like the chiral density wave, it can be seen that the inhomogeneous phase is surrounded everywhere by second-order transition lines joining at a Lifshitz point (LP), whose position coincides with the location of the critical point [90, 89]. Since we numerically checked that at zero temperature these solitonic solutions are the most favored among all those considered, and a complementary GL analysis has shown that higher dimensional modulations are disfavored in the vicinity of the critical point [88], we expect the phase diagram presented in Fig. 4.2 to be the most accurate, at least within the NJL model in mean-field approximation².

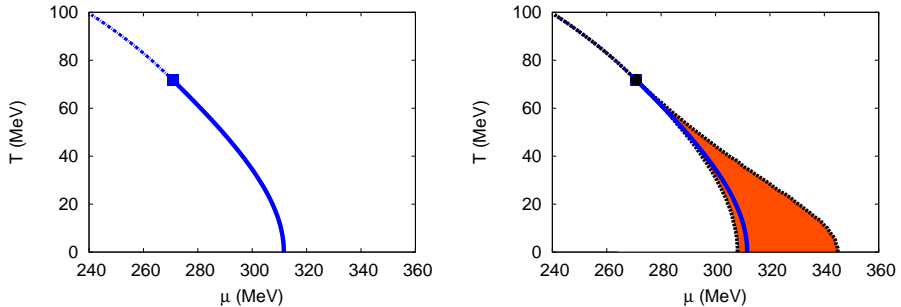


Figure 4.2.: Model (T, μ) phase diagram. Left: homogeneous phases only, the solid line denotes a first-order phase transition turning into a second-order one (dotted line) at the critical point (square). Right: phase diagram including solitonic inhomogeneous condensates: the shaded area denotes the inhomogeneous phase, surrounded by second-order (dotted) lines joining at a Lifshitz point (circle).

²We note however that this result might be modified if we allow for the formation of color-superconducting phases.

4.2. Density profiles

Unlike for the CDW ansatz, in the case of the real solitonic solutions the density of the system is spatially modulated, following the shape of the chiral condensate. In this section we present some exemplary shapes for this spatially modulated density inside the inhomogeneous phase. For simplicity, we limit ourselves to the chiral limit and work at zero temperature, although this is not essential.

In mean-field the density profile is given by the expectation value (a more detailed derivation is presented in Appendix F)

$$n(\mathbf{x}) = \langle \psi^\dagger(\mathbf{x})\psi(\mathbf{x}) \rangle = \frac{1}{2V} \sum_E \psi_E^\dagger(\mathbf{x})\psi_E(\mathbf{x}) (n_+(E) - n_-(E)) , \quad (4.2)$$

where the $\psi_E(\mathbf{x})$ are eigenfunctions of the Hamiltonian \mathcal{H} (Eq. (2.13)) for the eigenvalues E and $n_\pm(E)$ are the Fermi occupation numbers:

$$n_\pm = (1 + \exp((E \mp \mu)/T))^{-1} . \quad (4.3)$$

For the one-dimensional solitonic modulations, $\psi^\dagger(z)\psi(z)$ will only depend on the one-dimensional eigenvalues λ of the GN Hamiltonian (Eq. (3.24)) and we can write

$$n(z) = \frac{2N_c}{V} \int d\lambda \rho_{1D}(\lambda) \int \frac{dp_\perp}{(2\pi)^{d_\perp}} \psi_\lambda^\dagger(z)\psi_\lambda(z) (n_+(E) - n_-(E)) , \quad (4.4)$$

where $\rho_{1D}(\lambda)$ is the spectral density of the one-dimensional GN model [45, 46, 50, 49] and

$$\psi_\lambda^\dagger(z)\psi_\lambda(z) = \frac{(\lambda/\Delta)^2 + \frac{1}{2}((M(z)/\Delta)^2 + \nu - 2)}{(\lambda/\Delta)^2 - \mathbf{E}(\nu)/\mathbf{K}(\nu)} . \quad (4.5)$$

The resulting density profiles at $T = 0$ and four different chemical potentials are shown in the lower part of Fig. 4.3. Comparing them with the corresponding mass functions $M(z)$, which are displayed in the upper part of the figure, we find that the density distributions follow closely the positions of the solitons, i.e., of the zero-crossings of the mass functions. In a bag-model like picture, this can be interpreted as the quarks being squeezed by the bag pressure of the domains with broken chiral symmetry into the regions of space where chiral symmetry is almost restored. From a topological point of view, these quarks are related to zero energy modes localized on the domain-wall.

These features are seen most clearly at $\mu = 307.5$ MeV, which is just above the phase boundary from the homogeneous broken phase. Here the solitons are well separated, leading to strongly localized density peaks as functions of z . When μ is increased the solitons quickly start to overlap and the density profiles become more and more washed out. At the second-order transition to the restored phase, the order parameter melts and the density profile smoothly approaches the uniform density of the restored phase. This is illustrated by the example of $\mu = 345$ MeV, which is close to the phase boundary. Note, however, that already at $\mu = 325$ MeV the density variations are relatively small. We

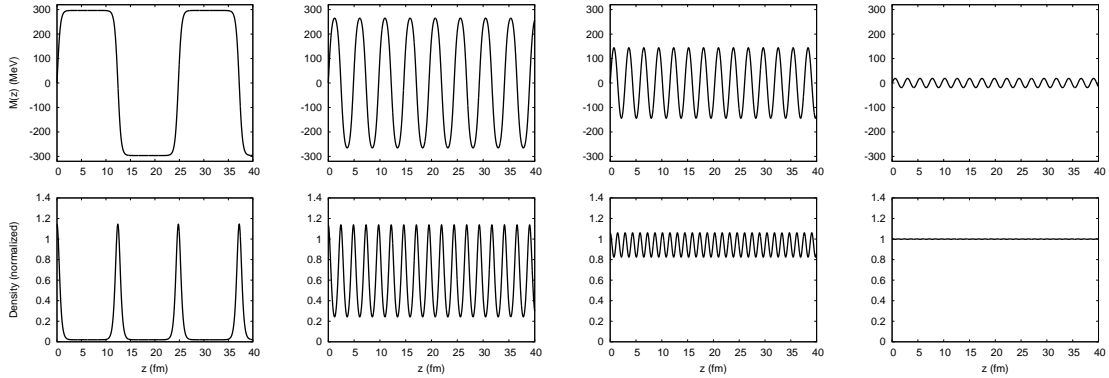


Figure 4.3.: Spatially dependent constituent mass function $M(z)$ (upper row) and corresponding density profile (lower row) for $T = 0$ and, from left to right, $\mu = 307.5, 309, 325$, and 345 MeV. The density is normalized to the density in the restored phase, $n_{rest} = \frac{2N_c}{3\pi^2} \mu^3$.

can therefore state that the density of the system approaches a constant value as we move towards the chiral restoration transition. In particular, we expect it to be constant in the proximity of the Lifshitz point.

4.3. Finite quark masses

All the results so far have been obtained in the chiral limit. When considering the solitonic solutions, the extension of the model to include explicit breaking of chiral symmetry is nevertheless straightforward. It can be seen that the introduction of finite current quark masses ($m \neq 0$) leads to a generalization of the order parameter to [46]

$$M_{\text{soliton},m}(z) = \Delta \left(\nu \text{sn}(b|\nu) \text{sn}(\Delta z|\nu) \text{sn}(\Delta z + b|\nu) + \frac{\text{cn}(b|\nu) \text{dn}(b|\nu)}{\text{sn}(b|\nu)} \right). \quad (4.6)$$

Here b is an additional parameter to be varied together with Δ and ν when minimizing the thermodynamic potential. It can be seen [46, 90] that for the solitonic solutions the inclusion of finite current quark masses simply amounts to modifying the density of states in the expression for Ω_{kin} into

$$\rho_{\text{soliton},m}(E) = \frac{E}{\sqrt{E^2 - \delta\Delta^2}} \rho_{\text{soliton}}(\sqrt{E^2 - \delta\Delta^2}) \theta(E - \sqrt{\delta}\Delta), \quad (4.7)$$

where $\delta \in [0, \infty]$ is defined through the relation $\text{sn}(b|\nu) = \frac{1}{\sqrt{1+\delta}}$. The chiral limit, i.e. $m = 0$, corresponds to $\delta = 0$ or equivalently $b = \mathbf{K}(\nu)$.

The resulting phase diagram for a bare quark mass of $m = 5$ MeV is reported in Fig. 4.4. Since there is no exact order parameter to distinguish the homogeneous broken from the

restored phase in this case, there are strictly speaking only two phases, a homogeneous and an inhomogeneous one, and, hence, no Lifshitz point. Nevertheless we can easily identify the remnant of the LP as a cusp in the phase boundary. For simplicity, we will call this point a Lifshitz point as well. From Fig. 4.4 it can be seen that the inclusion of a finite current quark mass reduces the size of the inhomogeneous window, which however is not destroyed. The Lifshitz point is shifted towards lower temperatures and higher chemical potentials. Above the LP, chiral restoration occurs through a smooth crossover without the formation of an inhomogeneous condensate.

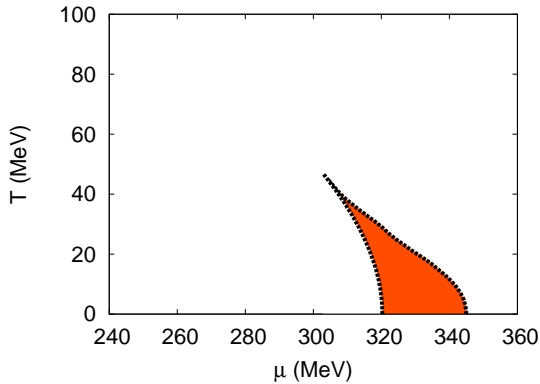


Figure 4.4.: Phase diagram with solitonic solutions for a bare quark mass of $m = 5$ MeV. The shaded area indicates the inhomogeneous phase.

4.4. Quark-Meson model results

For completeness, we present here the phase diagram obtained when allowing for the solitonic solutions in the quark-meson model. In the following, we will only consider the chiral limit. Since we are not considering vacuum fluctuations explicitly (see Sec. 2.3), the phase diagram for homogeneous phases features a first order line reaching up to the $\mu = 0$ axis, with no critical point. Consequently, the inhomogeneous phase reaches the temperature axis as well, as shown in Fig. 4.5. It is known that either the introduction of a realistic pion mass or the proper inclusion of vacuum fluctuations have the effect of moving the critical point back into the phase diagram [87], and for the case of finite pion masses it has been shown that the inhomogeneous phase follows the critical point and the Lifshitz point reappears³ [90].

³We note however that in the Quark-Meson model the Lifshitz point does not necessarily coincide with the critical point, unless the mass of the sigma meson is equal to twice the constituent quark mass. This result can be obtained from a GL analysis.

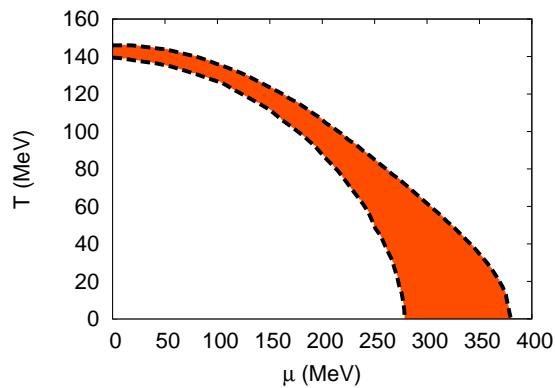


Figure 4.5.: Phase diagram of the Quark-Meson model when including the solitonic solutions. The inhomogeneous phase (shaded area) extends up to the temperature axis.

5. Effects of model extensions on inhomogeneous phases

This chapter is devoted to the discussion of the effects on the inhomogeneous “island” discussed in the previous chapter of some common extensions of the NJL model. In particular, we will focus on the introduction of vector interactions and of an effective coupling with the Polyakov loop. Similarly to the previous chapter, we will mostly consider the one-dimensional solitonic solutions.

5.1. Inclusion of vector-channel interactions

In view of finite density investigations, an important extension of the original NJL model is given by the inclusion of an isoscalar vector-channel interaction term. This kind of interaction naturally arises in the NJL model when motivating the interaction from a one-gluon exchange in QCD [76] and was already shown to be of particular importance in the Walecka model at finite densities [94]. More recently, its influence on the location and emergence of critical points in the phase diagram has attracted new interest [95, 96, 97, 98].

The model Lagrangian is given by

$$\mathcal{L} = \bar{\psi} (i\gamma^\mu \partial_\mu - m) \psi + G_S \left((\bar{\psi} \psi)^2 + (\bar{\psi} i\gamma^5 \tau^a \psi)^2 \right) - G_V (\bar{\psi} \gamma^\mu \psi)^2. \quad (5.1)$$

When performing the mean-field approximation, one must introduce additional condensates, related to the expectation values of this new operator $(\bar{\psi} \gamma^\mu \psi)$. The spatial part of this vector condensate is usually neglected, since for homogeneous matter one does not expect the system to break translational invariance. Of course this assumption is no longer valid if translational symmetry is already spontaneously broken by the formation of a crystalline condensate, in the following we will however for computational reasons perform this approximation as well.

We are then left with only the temporal part of the vector condensate,

$$n(x) = \langle \bar{\psi} \gamma^0 \psi \rangle, \quad (5.2)$$

which has the form of a quark number density $(\psi^\dagger \psi)$, in the same way as the term containing the chemical potential in Eq. (2.22). Performing the mean-field approximation, we obtain

$$(\bar{\psi} \gamma^\mu \psi)^2 \simeq -n(x)^2 + 2n(x)\bar{\psi} \gamma^0 \psi. \quad (5.3)$$

5.1.1. Homogeneous case

As mentioned in the previous section, the term including the density mean field has the same shape in \mathcal{L}_{MF} as the one containing the chemical potential. In presence of an homogeneous chiral condensate (and consequently baryon density), it is therefore possible to simply reabsorb this new term in a redefinition of the quark chemical potential, which becomes then a new quantity to be determined self-consistently [81, 99, 18, 96]. For this, we introduce a “renormalized” chemical potential

$$\tilde{\mu} = \mu - 2G_V n, \quad (5.4)$$

and the thermodynamic potential becomes simply

$$\begin{aligned} \Omega(T, \mu; M) = & -N_f N_c \int_0^\infty dE \rho_{hom}(E; M) [f_{vac}(E) + f_{med}(E; T, \tilde{\mu})] \\ & + \frac{(M - m)^2}{4G_S} - \frac{(\mu - \tilde{\mu})^2}{4G_V}. \end{aligned} \quad (5.5)$$

where f_{med} has the exact same shape as in standard NJL without vector interactions, but with μ replaced by $\tilde{\mu}$. The equilibrium value for the constituent quark mass and the renormalized chemical potential can be obtained by solving the equations giving the stationary conditions:

$$\frac{\delta \Omega}{\delta M} = 0, \quad \frac{\delta \Omega}{\delta \tilde{\mu}} = 0. \quad (5.6)$$

It is worth mentioning at this point that the second stationary condition in Eq. (5.6) is known to lead to a maximum for $\tilde{\mu}$ instead of a minimum. As such, this must not be interpreted as a minimization of the free energy, but rather as a constraint for thermodynamical consistency [18].

In this work, the value of G_V is treated as a free parameter, which will be varied in order to study its effect on the phase diagram. Starting from a color-current interaction and performing a Fierz transformation one would get $G_V/G_S = 1/2$, whereas fits to the vector meson spectrum typically yield larger values [76, 100]. In the following we will therefore vary G_V between zero and G_S . We will also restrict ourselves to repulsive vector interactions, similar as in the Walecka model [94].

Results for homogeneous order parameters in the chiral limit are shown in Fig. 5.1. The inclusion of repulsive vector interactions shifts the phase transition line towards higher chemical potentials and lowers the position of the critical point (CP). Above a given value of G_V between $G_S/5$ and $G_S/2$, the chiral restoration transition becomes second order everywhere, and the critical point disappears from the phase diagram.

5.1.2. Inhomogeneous case: solitonic solutions

The problem of including vector interactions for the solitonic solutions discussed in the previous chapter cannot be solved exactly in a straightforward manner. Indeed, for this

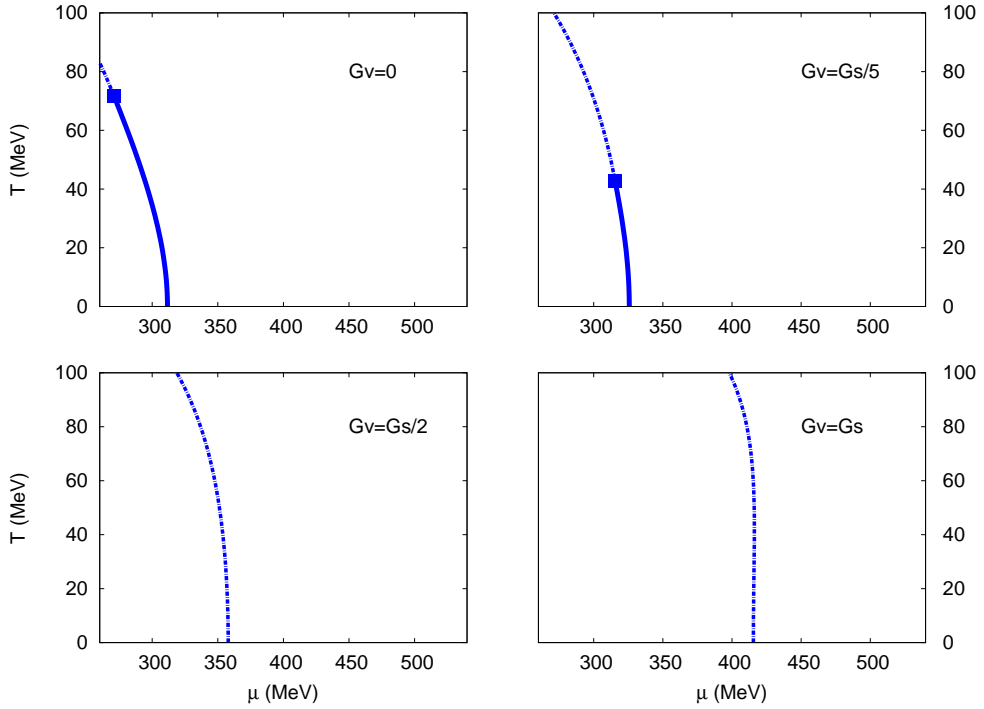


Figure 5.1.: The phase diagram for homogeneous phases in the chiral limit for different values of the vector coupling G_V . The blue solid lines represent the first-order phase transition, which turns to second order (blue dot-dashed lines) at the critical point (square).

kind of spatially modulated chiral condensate, as seen in Sec. 4.2 the density is not constant and the renormalized chemical potential becomes a spatially dependent quantity as well. In order to be able to reuse the known analytical results for the density of states in the expression for the thermodynamic potential, we choose to sacrifice complete self-consistency and approximate the density by its spatial average,

$$n(\mathbf{x}) \rightarrow \bar{n} \equiv \langle n(\mathbf{x}) \rangle_{\mathbf{x}} = \frac{1}{V} \int_V d\mathbf{x} n(\mathbf{x}). \quad (5.7)$$

As a consequence, $\tilde{\mu}$ becomes constant as well, and the problem reduces to the known case without vector interactions at a shifted value of the chemical potential given by

$$\tilde{\mu} = \mu - 2G_V \bar{n}, \quad (5.8)$$

Of course, at first sight, it seems rather questionable whether the replacement Eq. (5.7) is a good approximation in an inhomogeneous phase. However, by looking at the density profiles for the solitonic solutions discussed in Sec. 4.2, we can argue that it can be justified in the vicinity of the second-order phase boundary to the restored phase, and in particular

for the Lifshitz point.

Within this setup the average density is given by

$$\bar{n} = N_f N_c \int_0^\infty dE \rho_{\text{soliton}}(E) (n_+ - n_-), \quad (5.9)$$

with the usual occupation numbers $n_\pm = 1/(1 + \exp((E \mp \tilde{\mu})/T))$. We emphasize that, besides explicitly depending on $\tilde{\mu}$ via the occupation numbers, \bar{n} is a functional of $M(\mathbf{x})$ via the density of states $\rho_{\text{soliton}}(E)$.

At this stage it is worth noting that for most quantities all dependence on G_V can be absorbed into $\tilde{\mu}$. In particular the form of the gap equation (Eq. (5.6)) and, hence, its solutions $M(\mathbf{x})$ are identical to the case without vector interaction upon replacing $\mu \rightarrow \tilde{\mu}$. As obvious from Eq. (5.9), the same is true for the average density \bar{n} . As a consequence, the mass functions $M(\mathbf{x})$ at a given \bar{n} do not depend on G_V . For homogeneous phases this is a well-known result [18]. The remaining effect of G_V is on the one hand side to map $\tilde{\mu}$ onto μ via Eq. (5.8), and on the other hand to shift the value of the thermodynamic potential of a solution by $-G_V \bar{n}^2$. This will be important for the explanation of our results later on.

In Fig. 5.2 we present the $\mu - T$ phase diagrams for various values of G_V , focusing on the region where the domain-wall soliton lattice is preferred. The calculations have been performed in the chiral limit. For comparison we have also indicated the transition lines one obtains when the analysis is limited to homogeneous phases.

As previously discussed, for $G_V = 0$ the Lifshitz point precisely agrees with the critical point of the purely homogeneous analysis. It turns out, however, that this is no longer true for $G_V > 0$: whereas with increasing vector coupling the critical point moves downwards in temperature and eventually disappears from the phase diagram, we observe that the Lifshitz point is only shifted in the μ -direction, while remaining at the same temperature. Consequently, unlike the first-order boundary in the purely homogeneous case, the existence of the inhomogeneous phase is not inhibited by the vector interaction. At vanishing temperature the transition from the homogeneous broken to the inhomogeneous phase is only slightly varying with G_V , whereas the transition from the inhomogeneous to the restored phase significantly shifts, thus enhancing the domain where inhomogeneous phases are favored.

The observed G_V -dependence of the phase diagram can easily be understood when we recall that the stationary condition (Eq. (5.6)) depends on G_V only through $\tilde{\mu}$. Consequently its solutions $M(\mathbf{x})$ at given $(\tilde{\mu}, T)$ are independent of G_V and thus equal to the solutions at $G_V = 0$ where $\tilde{\mu} = \mu$. At $G_V > 0$, we can then translate these solutions into solutions at shifted values of μ , which are obtained from Eq. (5.8). For a given mass function this mapping is unique since the average density \bar{n} also depends on G_V only through $\tilde{\mu}$, see Eq. (5.9).

The consequences of this mapping can be elaborated further for the phase transition lines. We first consider the case of second-order phase transitions as found in our calculation. When approaching the second-order transition from any direction, for each extremum in

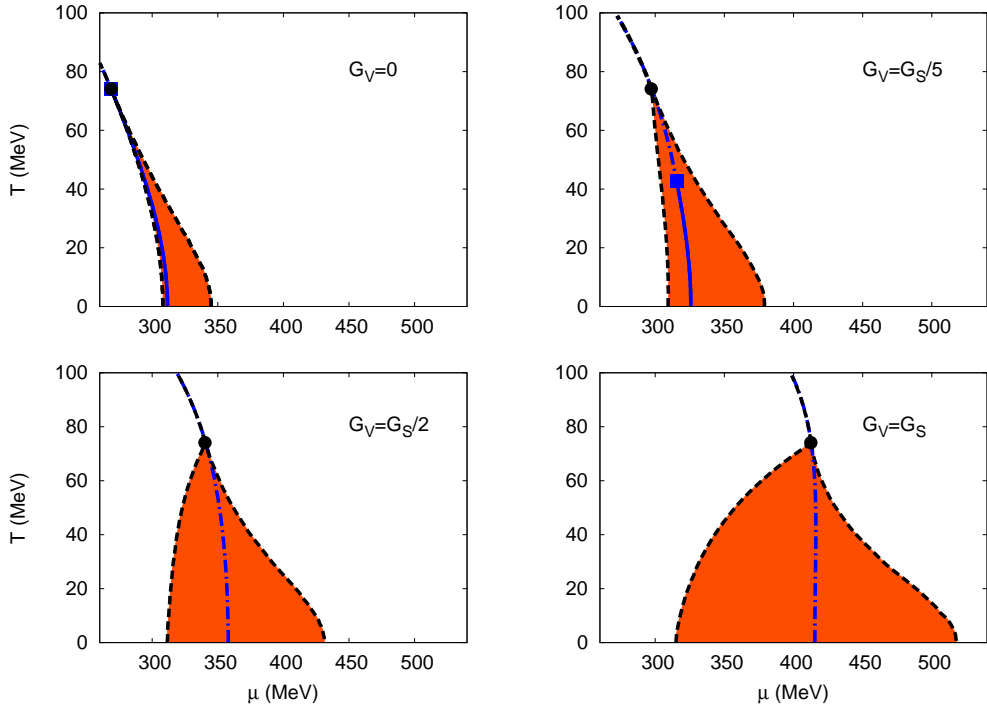


Figure 5.2.: The phase diagram in the chiral limit for different values of the vector coupling when allowing for the domain-wall soliton lattice. The black dashed lines represent the second-order transition lines joining at the Lifshitz point (dot), the shaded region represents the inhomogeneous phase. The blue solid lines represent the first-order phase transition obtained when limiting to homogeneous order parameters, which turns to second order (blue dot-dashed lines) at the critical point (square).

the thermodynamic potential that is relevant for the transition the density approaches the same value and consequently all extrema are mapped to the same value of μ . Since there is only one extremum left on one side of the phase transition, we only have to make sure that the additional extremum on the other side cannot be mapped beyond the phase transition line, thus generating a spinodal region. For the transitions into the restored phase this is guaranteed by the fact that the restored solution has the highest possible density at given $\tilde{\mu}$ and that the density increases with $\tilde{\mu}$. Therefore no other solution can be mapped beyond the transition line for $G_V > 0$. Similarly the homogeneous broken solution has the lowest density at given $\tilde{\mu}$ and therefore no inhomogeneous solution can be mapped below the transition line when going from the inhomogeneous into the homogeneous broken phase. Consequently all second-order transition lines for $G_V = 0$ are mapped onto second-order transition lines for $G_V > 0$. In particular, this explains why the Lifshitz point stays at the same temperature, as the mapping leaves T untouched.

From the arguments given above, it follows immediately that the phase diagram in the $\tilde{\mu}$ - T plane is independent of G_V . Moreover, since in this case $\bar{n}(T, \tilde{\mu})$ is uniquely given by Eq. (5.9) and therefore also independent of G_V , this means that the \bar{n} - T phase diagram is independent of G_V as well. This diagram is presented in Fig. 5.3.

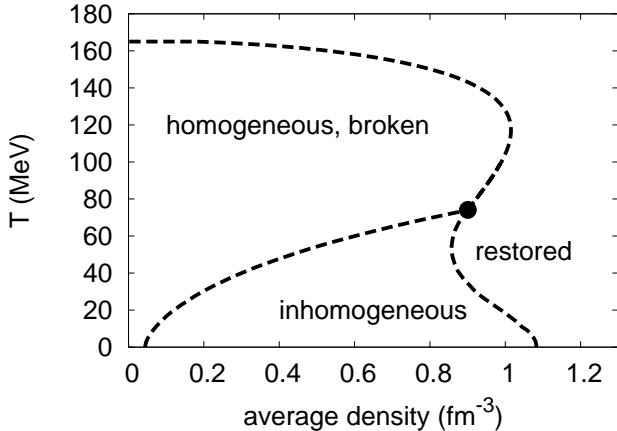


Figure 5.3.: The phase diagram in the $\bar{n} - T$ plane. The transition lines do not depend on G_V for $G_V > 0$.

A slight complication of this picture arises if there is a first-order phase transition at $G_V = 0$, which occurs when limiting to homogeneous phases. In this case we have a spinodal region enclosing the first-order phase transition line, where the thermodynamic potential has several extrema at the same value of μ : two local minima and one local maximum. As before, this means that at $G_V > 0$ we have several solutions at the same value of $\tilde{\mu}$. However, since the local extrema correspond to different masses and therefore to different densities, they will now be mapped onto different values of μ by Eq. (5.4): more precisely, solutions with lower masses will be shifted to higher values of μ than solutions with higher masses. As a consequence, the spinodal region shrinks with increasing G_V , i.e., at fixed temperature the first-order transition gets weakened and eventually becomes second order. This explains why the CP moves to lower temperatures and finally disappears from the phase diagram, as seen in the previous section. (see also Ref. [96] for a detailed discussion of this effect).

Finally, we would like to comment on the slopes of the three phase transition lines in the Lifshitz point. For $G_V = 0$ all of them are equal, i.e., the phase boundaries are tangential. In the $\tilde{\mu} - T$ plane, this remains of course true for $G_V > 0$. However, when we employ Eq. (5.8) to map $\tilde{\mu}$ onto μ we have to keep in mind that the average density \bar{n} at given T and $\tilde{\mu}$ depends on the constituent quark mass M . The latter vanishes identically at the two phase boundaries to the restored phase, but is nonzero at the boundary between the homogeneous broken and the inhomogeneous phase, approaching zero only towards the Lifshitz point. Depending on the corresponding critical exponent, this can affect the slope

of this boundary in such a way that it meets the two others with a non-vanishing angle at $G_V > 0$. As one can see in Fig. 5.2, this is indeed the case.

As previously discussed, the assumption of a uniform density profile is most questionable at the transition from the homogeneous broken to the inhomogeneous phase at low temperatures. In fact, at $G_V > 0$, a local density approximation would result in a lower value of $\tilde{\mu}$ within the solitons. This reflects the repulsive nature of the vector interaction, which disfavors localized density peaks. We therefore expect that the formation of well separated solitons, as we find near the boundary to the homogeneous broken phase at $T = 0$, eventually becomes inhibited by the vector interaction. Related to this, the second-order phase transition from the homogeneous broken to the inhomogeneous phase may partially turn into a first-order transition at $G_V > 0$. On the other hand, our assumption of a uniform density becomes gradually better with increasing μ or T and is fully justified at the phase transition line to the restored phase. In particular the phase boundary itself and the Lifshitz point are not affected by the approximation. This will be shown more rigorously in Appendix G by means of a Ginzburg-Landau analysis.

5.1.3. Chiral density wave

Complementary support for the results of the previous section can be obtained from investigations of the chiral density wave defined in Eq. (3.16). Although, at least at $G_V = 0$, this kind of modulation is disfavored compared to the domain-wall soliton, a constant density profile is no assumption here, but a property of the state. This is most easily seen by applying a global chiral transformation of the form $\psi \rightarrow \exp(i\gamma_5\tau_3 qz_0/2)\psi$ with some constant z_0 . While the density $\langle\psi^\dagger(\mathbf{x})\psi(\mathbf{x})\rangle$ is invariant under this transformation, it leads to a phase shift in $M(\mathbf{x})$ which is equivalent to a translation by z_0 in the z-direction. Hence the density must be uniform. The replacement Eq. (5.7) is therefore an exact manipulation for the CDW, which will allow us to comment on the corresponding approximation for the solitons. We can therefore perform a completely self-consistent mean-field calculation, leading to the phase diagrams shown in Fig. 5.4. The calculations have again been performed in the chiral limit and for $G_V = 0$ (left panel) and $G_V = G_S$ (right panel). The regions where the CDW is favored against the homogeneous broken and restored phases are indicated by the shaded areas. For comparison we have also indicated the boundaries of the regime where the solitons are favored (dashed lines).

As previously discussed, the transition from the CDW to the chirally restored phase is second order and agrees exactly with the transition from the soliton lattice to the restored phase. In particular, this also holds for the Lifshitz point. On the other hand, the transition from the homogeneous broken phase to the state where the CDW is preferred is first order. For this reason, given the arguments of the previous section, it is directly depending on G_V , not only through $\tilde{\mu}$. As a result, the phase boundary, which at $G_V = 0$ almost coincides with the corresponding phase boundary of the soliton phase, moves away from it at $G_V = G_S$. This effect is however rather mild. Moreover we find that the first-order transition line from the homogeneous broken to the CDW phase is much less affected by the vector interaction than the second-order transition line from the CDW to the restored phase. The qualitative behavior of the phase diagram as a function of G_V

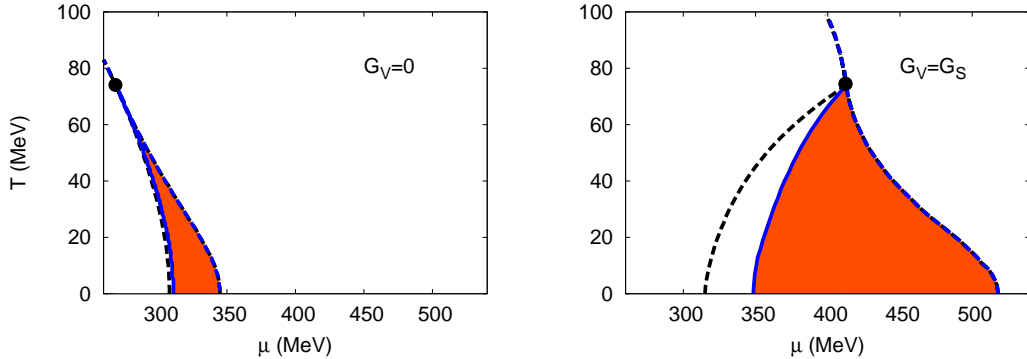


Figure 5.4.: Phase diagrams in the $\mu - T$ plane at $G_V = 0$ (left) and $G_V = G_S$ (right). The dashed lines have the same meaning as in Fig. 5.2 and represent the second-order phase boundaries between the homogeneous broken phase, the restored phase and the inhomogeneous phase with domain-wall solitons, respectively. The shaded area indicates the region where the CDW is favored compared to homogeneous phases (but not to the solitons). Here the blue solid line represents the first-order phase boundary from the broken homogeneous phase to the CDW, while the phase boundary from the CDW to the restored phase is second order and coincides with the boundary from the soliton phase to the restored phase.

is therefore similar to our results for the soliton lattice. Since we expect the CDW to be disfavored compared to the solitons, we can take the CDW result as a lower limit for the area occupied by an inhomogeneous phase. This suggests that the effect of assuming a uniform density profile for the solitons is not drastic.

5.1.4. Quark number susceptibilities

The divergence of susceptibilities near a critical point has led to suggestions for how to locate the CP in the QCD phase diagram experimentally [64] and therefore attracted significant interest also in model studies. Since the critical point as a cornerstone of the phase diagram is essentially replaced by the Lifshitz point in our study, we first want to discuss the behavior in its vicinity. For simplicity we will limit ourselves to the number susceptibility

$$\chi_{nn} = -\frac{\partial^2 \Omega}{\partial \mu^2} = \frac{\partial \bar{n}}{\partial \mu}, \quad (5.10)$$

which corresponds to the change in density with μ when going along a line of constant temperature. For this reason the behavior of χ_{nn} near the Lifshitz point is in fact determined by the behavior when going from the homogeneous broken to the restored phase and not by the inhomogeneous phase. Consequently, since the Lifshitz point coincides with the CP for $G_V = 0$, we find the same divergent behavior as when limiting to homo-

geneous phases for $G_V = 0$. This is illustrated on the right hand side of Fig. 5.5, showing a $1/\sqrt{\mu_{\text{cr}} - \mu}$ -like singularity when approaching the Lifshitz point from the left. However, for $G_V > 0$ the behavior is qualitatively altered: The would-be CP when limiting to homogeneous phases is hidden inside the domain of a inhomogeneous phase and the Lifshitz point does not correspond to the endpoint of the second-order phase transition line when limiting to homogeneous phases. For this reason the number susceptibility does not diverge near the Lifshitz point for $G_V > 0$. This can easily be understood in the context of a Ginzburg-Landau expansion, as discussed in Appendix G.

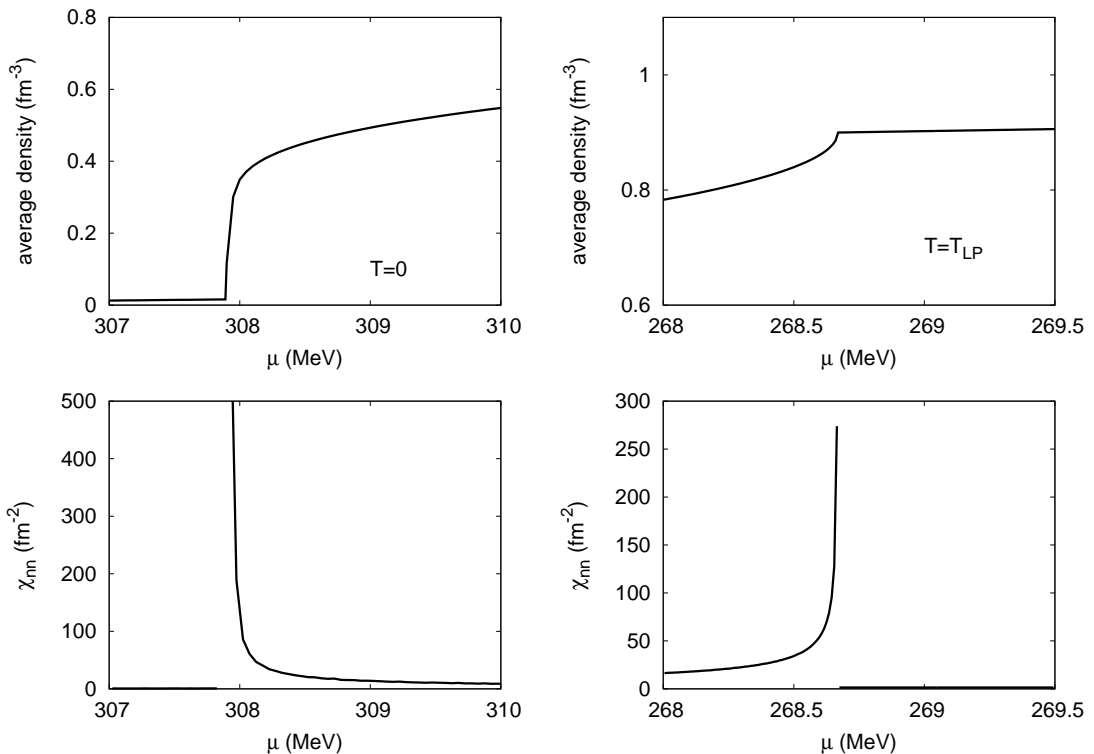


Figure 5.5.: Averaged density (upper panel) and number susceptibility (lower panel) for vanishing temperatures (left) and for the temperature at the Lifshitz point (right) as a function of chemical potential and for $G_V = 0$.

Focusing on $G_V = 0$ first and investigating the number susceptibility numerically in the regime where soliton lattices are energetically preferred, we find the results shown in Figs. 5.5 and 5.6 (left). Since all transition are second order, the averaged number density changes continuously when varying temperature and chemical potential. At the transition from the homogeneous broken to the inhomogeneous phase the change is however very rapid as discussed in the following and χ_{nn} diverges. This is most prominent at $T = 0$ and decreases when going towards the Lifshitz point.

In order to get an intuition for the qualitative behavior of χ_{nn} we consider the GN model

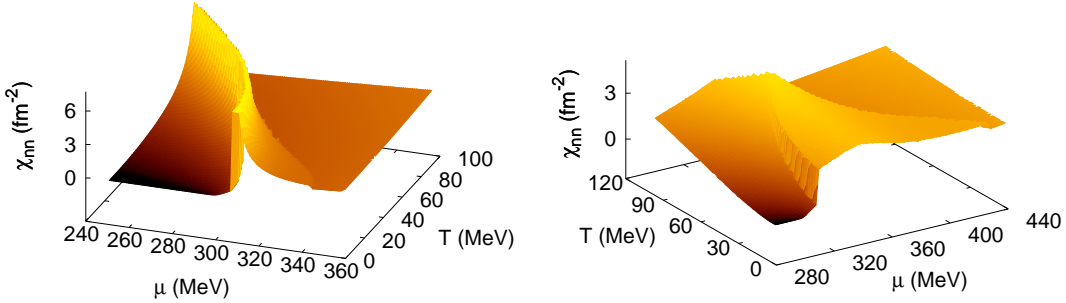


Figure 5.6.: Number susceptibility in the $\mu - T$ plane at $G_V = 0$ (left) and $G_V = G_S/2$ (right). For $G_V = 0$ the number susceptibility diverges at the transition from broken to inhomogeneous phase.

and focus on the density as a function of chemical potential $n_{GN}(\mu)$ at vanishing temperatures. As can be extracted from Refs. [45, 50] it is given by

$$n_{GN} = \frac{\pi^2}{2\nu\mathbf{K}(\nu)} M_{vac}, \quad (5.11)$$

where M_{vac} as the fermion mass in the vacuum sets the scale and the elliptic modulus as a function of chemical potential is given through the implicit relation $\pi\sqrt{\nu}\mu = 2\mathbf{E}(\nu)M_{vac}$. At the transition from homogeneous to inhomogeneous phase at $\mu_{cr} = \frac{2}{\pi}M_{vac}$ the number density then behaves like

$$n_{GN} \simeq -\frac{\pi^2 M_{vac}}{\log(\mu/\mu_{cr} - 1)}, \quad (5.12)$$

which leads to a $[(\mu - \mu_{cr}) \log^2(\mu - \mu_{cr})]^{-1}$ -like singularity in the number susceptibility. A straightforward generalization of Eq. (5.12) to three spatial dimensions suggests that for $G_V = 0$ the change $\Delta\bar{n}$ in the average number density near the transition from the broken homogeneous to the inhomogeneous phase at $\mu = \mu_{cr}(T)$ should be given by

$$\Delta\bar{n} = -\frac{c\mu_{cr}^3}{\log(\mu/\mu_{cr} - 1)}, \quad (5.13)$$

with some temperature-dependent coefficient c . Indeed, our numerical results are consistent with this behavior, thus explaining the divergence of χ_{nn} at $\mu = \mu_{cr}$.

In contrast, for $G_V > 0$ the mapping $\tilde{\mu} \rightarrow \mu$ via Eq. (5.8) leads to a qualitatively different behavior. For this case we find

$$\chi_{nn} = \frac{\partial n}{\partial \tilde{\mu}} / \frac{\partial \mu}{\partial \tilde{\mu}} = \frac{1}{1 + 2G_V \frac{\partial n}{\partial \tilde{\mu}}} \frac{\partial n}{\partial \tilde{\mu}} \bigg|_{\tilde{\mu}(\mu)}. \quad (5.14)$$

Therefore a divergence in $\partial n/\partial \mu$ at $G_V = 0$ does not result in a divergent number susceptibility for $G_V > 0$, but merely leads to a jump of order $1/2G_V$. This is illustrated on the right hand side of Fig. 5.6.

5.1.5. Finite current quark masses and vector interaction

For completeness we present in Fig. 5.7 results for the phase diagram of the solitonic solutions at a non-vanishing current quark mass $m = 5$ MeV and various values of G_V .

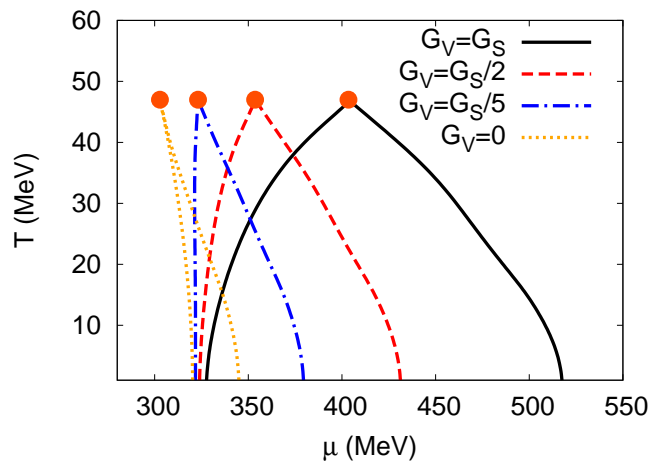


Figure 5.7.: $\mu - T$ phase diagram for different values of G_V and a current quark mass $m = 5$ MeV. The dots indicate the Lifshitz points above which the second order transition lines join and turn into a crossover.

It has already been shown in Sec. 4.3 that the Lifshitz Point shifts to smaller temperatures and larger chemical potentials with increasing m . The dependence on G_V however stays qualitatively the same as in the chiral limit: the Lifshitz point is only shifted in the μ -direction upon increasing G_V and the domain of inhomogeneous phases in the $\mu - T$ diagram is stretched. The explanation for this behavior is identical to the one given in Sec. 5.1.2 for the chiral limit.

5.2. Effects of Polyakov loop dynamics

The NJL model describes a system of self-interacting quarks and does not include gluonic degrees of freedom. As such, it does not confine, and is known to feature unphysical effects like the possibility for the decay of a meson into free quarks.

In order to mimic features of confinement, in particular to suppress the contribution of free constituent quarks in the confined phase, and in order to include gluonic contributions to the pressure, the NJL model can be coupled to an effective description of the Polyakov

loop [101, 102]. The resulting model is known as the Polyakov-loop extended Nambu–Jona-lasinio (PNJL) model.

The Polyakov loop is defined by

$$L(\mathbf{x}) = \mathcal{P} \exp \left[i \int_0^{1/T} d\tau A_4(\tau, \mathbf{x}) \right], \quad (5.15)$$

where $A_4(\tau, \mathbf{x}) = iA_0(t = -i\tau, \mathbf{x})$ is the temporal part of a gauge field $A_\mu = gA_\mu^a \frac{\lambda^a}{2}$ at imaginary time. In pure Yang-Mills theory, the traced expectation values of L and its hermitean conjugate,

$$\ell = \frac{1}{N_c} \langle \text{Tr}_c L \rangle, \quad \bar{\ell} = \frac{1}{N_c} \langle \text{Tr}_c L^\dagger \rangle, \quad (5.16)$$

can be related to the free energies of a static quark or antiquark, $\ell \sim e^{-F_q/T}$, $\bar{\ell} \sim e^{-F_{\bar{q}}/T}$ [103, 104], and are therefore order parameters for the confinement-deconfinement transition.

To include the Polyakov-loop dynamics in the NJL model, the quarks are minimally coupled to a background gauge field by introducing a covariant derivative D_μ :

$$\partial_\mu \rightarrow D_\mu = \partial_\mu + iA_0\delta_{\mu 0}. \quad (5.17)$$

Furthermore, a local potential $\mathcal{U}(\ell, \bar{\ell})$ is added to the thermodynamic potential, which is essentially constructed to reproduce ab-initio results of pure Yang-Mills theory at finite temperature [101, 105].

The PNJL Lagrangian thus reads

$$\mathcal{L}_{PNJL} = \bar{\psi}(i\gamma^\mu D_\mu - \hat{m})\psi + G_S ((\bar{\psi}\psi)^2 + (\bar{\psi}i\gamma^5\tau_a\psi)^2) + \mathcal{U}(\ell, \bar{\ell}). \quad (5.18)$$

In the most simple approach, the gauge field is taken to be a space-time independent mean field A_4 , and the effect of the covariant derivative in the kinetic part amounts to the replacement [102]

$$\begin{aligned} N_c f_{med}(E) \rightarrow f_{med}^{PNJL}(E) &= T \log \left(1 + e^{-3(E-\mu)/T} + 3\ell e^{-(E-\mu)/T} + 3\bar{\ell} e^{-2(E-\mu)/T} \right) \\ &+ T \log \left(1 + e^{-3(E+\mu)/T} + 3\bar{\ell} e^{-(E+\mu)/T} + 3\ell e^{-2(E+\mu)/T} \right). \end{aligned} \quad (5.19)$$

However, as can be seen from Eqs. (5.15) and (5.16), a constant mean field A_4 would always result in complex conjugate values for ℓ and $\bar{\ell}$. This should be considered as an artifact, since their interpretation as being related to the free energies of quarks and antiquarks means that ℓ and $\bar{\ell}$ should be real and, at finite chemical potential, different from each other. In order to by-pass this problem, we therefore follow the viewpoint of Ref. [95] that, after the replacement Eq. (5.19), ℓ and $\bar{\ell}$ should be treated as independent real mean fields, rather than the components of A_4 . This is also consistent with the fact that the potential \mathcal{U} which is added to the thermodynamic potential is given in terms of ℓ and $\bar{\ell}$ as well. For simplicity we take Fukushima's parametrization [95],

$$\mathcal{U}(\ell, \bar{\ell}) = -bT \left(54e^{-a/T} \ell \bar{\ell} + \log[1 - 6\ell \bar{\ell} - 3(\ell \bar{\ell})^2 + 4(\ell^3 + \bar{\ell}^3)] \right), \quad (5.20)$$

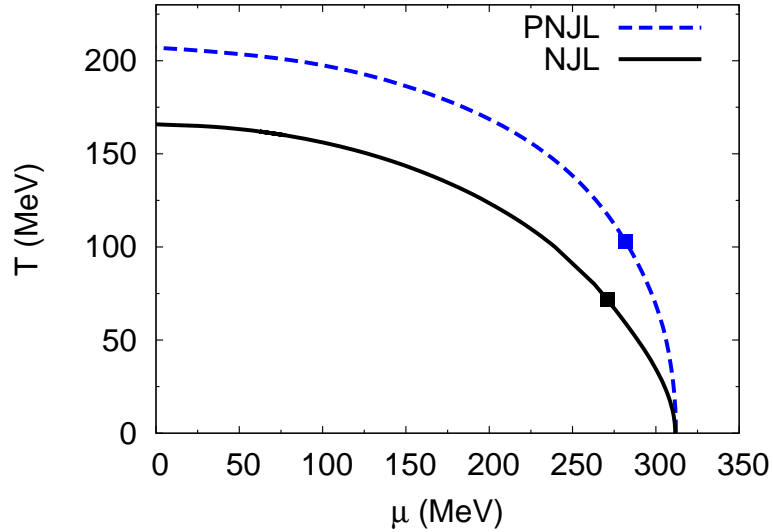


Figure 5.8.: Phase diagram of the NJL (solid line) and PNJL (dashed line) model for homogeneous phases.

with two parameters a and b . Other prescriptions, like the polynomial [101] or the logarithmic [105] potential, would lead to very similar results.

5.2.1. Homogeneous case

The PNJL thermodynamic potential for homogeneous condensates is given by

$$\Omega(T, \mu, M) = -N_f \int_0^\infty dE \rho_{hom}(E) [N_c f_{vac}(E) + f_{med}^{PNJL}(E; T, \mu)] + \frac{M^2}{4G_S} + \mathcal{U}(\ell, \bar{\ell}), \quad (5.21)$$

and the thermodynamically stable states can be determined by solving the in-medium gap equations

$$\frac{\partial \Omega}{\partial M} = 0, \frac{\partial \Omega}{\partial \ell} = 0, \frac{\partial \Omega}{\partial \bar{\ell}} = 0. \quad (5.22)$$

When including the coupling with the Polyakov loop, one and two-quark excitations are suppressed in the confined phase, as can be seen from Eq. (5.19). This results to a stretch of the chiral phase transition curve towards higher temperatures, as shown Fig. 5.8. There it is also possible to see that the position of the phase transition at $T = 0$ is unchanged in PNJL. This is due to the fact that at vanishing temperature the Polyakov-loop dynamics decouples completely from the quark sector due to the way the PNJL model is constructed.

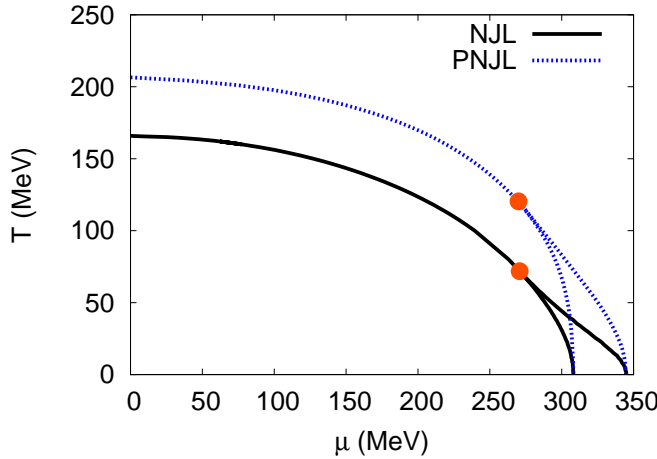


Figure 5.9.: Phase diagram of the NJL (solid line) and PNJL (dashed line) model allowing for one-dimensional spatial modulations of the order parameter.

5.2.2. Inhomogeneous case

When dealing with inhomogeneous phases, ℓ and $\bar{\ell}$ are naturally expected to be spatially dependent, presumably following the density profile in some way. Nevertheless, similar to the treatment of $\tilde{\mu}$ in the previous sections, we will assume spatially independent values of ℓ and $\bar{\ell}$, even in the inhomogeneous phase. This is not only to keep the technical side of the calculation trackable, but also the assumptions made in order to derive Eq. (5.19) and the unknown kinetic contributions to Eq. (5.20) suggest such a conservative approach as a first step. Within this kind of approximation, the thermodynamic potential can then be obtained from Eq. (5.21) by replacing the density of states and the condensate term with the appropriate ones for the kind of modulation considered.

Since we consider the NJL model with $G_V = m = 0$ as our starting point, we shall limit ourselves to this case when studying the role of the Polyakov loop. We employ the same parameter set as in Ref. [95] (values are reported in Appendix D.3).

In Fig. 5.9 we compare the phase diagrams for the NJL model with that of the PNJL model, allowing for phases with the one-dimensional solitonic modulation in both cases. Similar to what happens for homogeneous phases, the most notable effect of the coupling with the Polyakov loop is a stretch of the phase diagram in the T -direction. We point out here that a Ginzburg-Landau analysis suggests that the coupling with the Polyakov loop might lead to another splitting between the critical point and the Lifshitz point, similar to the case of vector interactions. A numerical cross-check shows however that, at least with our parameter set, this effect is so small that it is not possible to distinguish the position of the two points. A more detailed analysis of this behavior is therefore postponed to future work.

In Fig. 5.10 the value of ℓ is presented via color coding in the region of the phase diagram where the inhomogeneous phase is favored. We find that ℓ and $\bar{\ell}$ are rather small in the

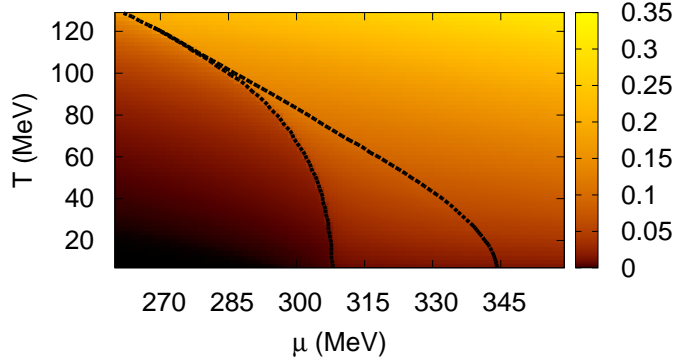


Figure 5.10.: Polyakov loop expectation value ℓ in the μ - T plane in the vicinity of the inhomogeneous phase.

entire inhomogeneous phase, reaching their maximum values $\ell \approx 0.15$ and $\bar{\ell} \approx 0.2$ near the Lifshitz point. In this context we recall that at vanishing temperature the Polyakov-loop dynamics decouples completely from the quark sector, and as a consequence $\ell = \bar{\ell} = 0$ at $T = 0$, independent of the density. While it is unclear whether this feature of the model is realistic, it means that our assumption of space-independent Polyakov-loop expectation values cannot have a large effect. Even if ℓ and $\bar{\ell}$ followed the density profile, the results would not be very different, because at low temperatures their values are very small anyway, whereas at higher temperatures the density differences get washed out.

5.2.3. PNJL and large N_c

Aside from providing a more realistic description of confined quark matter, the PNJL model can be used to investigate the influence of the number of colors on the phase diagram [106]. For this, the coupling to the Polyakov loop is crucial, since the NJL mean-field results without it are N_c -independent. The study of Ref. [106] was restricted to homogeneous phases, and its main focus was to see how the region of confined but chirally restored matter develops. Some time ago, this was thought to be a possible manifestation of quarkyonic matter, whereas according to the present picture chiral symmetry is inhomogeneously broken in the quarkyonic phase [58, 69, 70]. Therefore, since the latter has been derived in the large- N_c limit, it is particularly interesting to combine the approach of [106] with our formalism, and to study the behavior of the inhomogeneous phase in the PNJL model at large N_c .

As the exact implementation of the Polyakov-loop expectation value is not unique at arbitrary N_c , we follow Ref. [106] and change the function f_{med} in the thermodynamic potential into

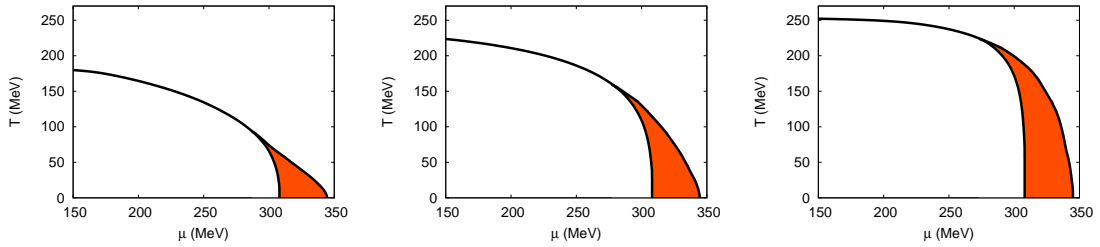


Figure 5.11.: PNJL phase diagram varying the number of colors: $N_c = 3$ (left), $N_c = 10$ (center), $N_c = 50$ (right). The shaded region indicates the inhomogeneous phase.

$$f_{med} = \theta(E_p - \mu)\ell T \left(e^{-(E_p - \mu)/T} + e^{-(E_p + \mu)/T} \right) + \theta(\mu - E_p) \left[(\mu - E_p) + \ell T \left(e^{-(\mu - E_p)/T} + e^{-(\mu + E_p)/T} \right) \right], \quad (5.23)$$

which basically amounts to a leading-order expansion for small ℓ and is as such expected to be accurate at large N_c in the confined phase. We furthermore rescale the Polyakov loop potential and the coupling constants via

$$G_S \rightarrow \frac{3G_S}{N_c}, \quad \mathcal{U}(\ell, \bar{\ell}) \rightarrow \frac{N_c^2 - 1}{8} \mathcal{U}(\ell, \bar{\ell}). \quad (5.24)$$

Our results for $N_c = 3, 10$ and 50 with the domain-wall solitonic ansatz are shown in Fig. 5.11. By increasing the number of colors, the inhomogeneous phase is enlarged and stretches towards higher temperatures, approaching the upper limit given by the pure glue transition temperature ($T_c = 270$ MeV in our parametrization of the Polyakov loop potential). The transition lines between homogeneous and inhomogeneous phases become more and more vertical, assuming a shape resembling the expected form for the phase diagram in the large N_c limit [67]. The size of the inhomogeneous phase is not dramatically enhanced in the μ direction, since as previously mentioned in the PNJL model the Polyakov loop decouples from the NJL sector at $T = 0$. Therefore, since the latter is N_c -independent in mean-field approximation, the transitions at $T = 0$ are unchanged.

6. Inhomogeneous phases at higher densities

This chapter focuses on the study of inhomogeneous phases at higher chemical potentials. The main motivation behind this comes from recent quarkyonic matter studies, suggesting that at sufficiently high densities chiral symmetry might be spontaneously broken in an inhomogeneous way [58], and in particular through the formation of increasingly complex crystalline structures [69, 70].

In the following we therefore push the model to its validity limits and check what is the favored shape for the ground state of the model at high chemical potentials, beyond the inhomogeneous island discussed in the previous sections. A thorough discussion on the reliability of these results is included as well.

6.1. An inhomogeneous “continent”

As shown in Fig. 6.1, above some critical chemical potential a second inhomogeneous phase appears in the model phase diagram. This phase seems to extend to arbitrarily high μ , with steadily growing amplitude and wave number of the spatial modulation. This inhomogeneous “continent” is present for all kinds of spatial modulations we considered, and its onset is again given by a second-order phase transition. In this case, we recall again that GL analyses reveal that the phase boundary is the same for all inhomogeneous solutions [89]. Within some parametrizations, especially when one chooses a stronger coupling to enforce a larger value of the constituent quark mass in vacuum, the continent turns out to be even directly connected to the inhomogeneous island discussed until now, as can be seen in Fig. 6.2.

Since the continent appears at relatively high chemical potentials and is characterized by large wave numbers for the chiral condensate, the first natural interpretation for it is that of an artifact of the regularization used. While this might indeed be the case, we will argue that the effect is at least non-trivial. In order to achieve some better understanding on the observed behavior, it might be worth analyzing in detail the mechanisms that within the model lead to the formation of an inhomogeneous condensate. Since, as argued above, we expect these considerations to be roughly independent of the particular ansatz chosen for the spatial modulation, we focus on the simplest possible case, namely the CDW (Eq. (3.16)).

In this case, we obtain for the thermodynamic potential

$$\Omega - \Omega_{rest} = -N_f N_c \int_0^\infty dE [\rho_{CDW}(E, M, Q) - \rho_{rest}(E)][f_{vac}(E, \Lambda) + f_{med}(E)] + \frac{M^2}{4G}, \quad (6.1)$$

where we have subtracted the free energy of the restored phase and explicitly indicated the dependence of the different terms on the Pauli-Villars cutoff Λ , the amplitude M and

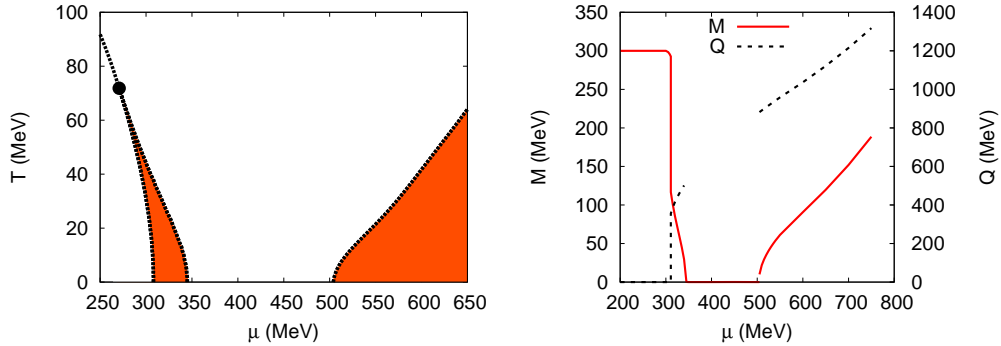


Figure 6.1.: Left: Phase diagram with inhomogeneous island and continent. Right: Amplitude and wave number for the CDW ansatz at $T = 0$.

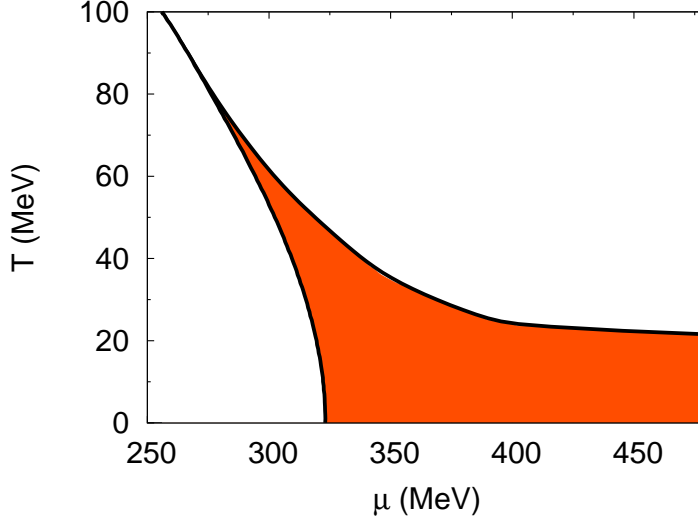


Figure 6.2.: Phase diagram for solitonic solutions with a parameter set fitted to give a vacuum constituent quark mass of $M_{vac} = 330$ MeV. The inhomogeneous phase (shaded area) extends up to arbitrarily high chemical potentials.

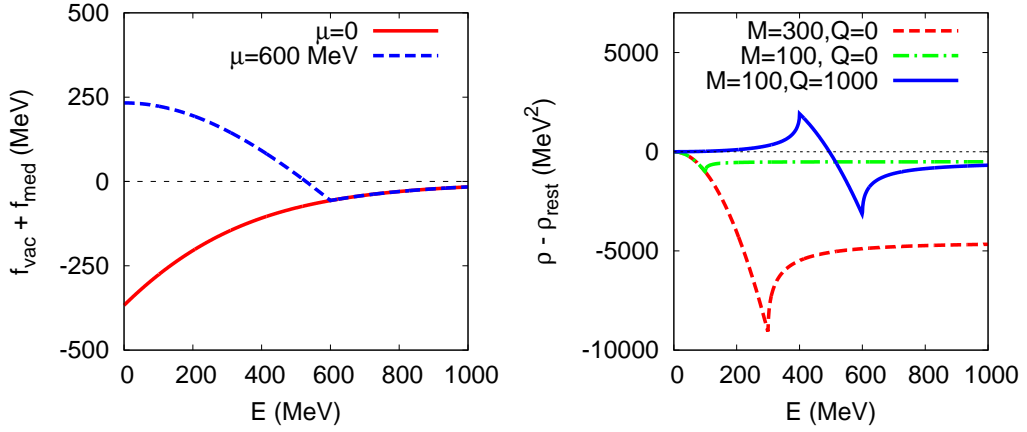


Figure 6.3.: Functions entering the integrand in the thermodynamic potential, Eq. (6.1). Left: The red solid line represents the Pauli-Villars regularized function f_{vac} , corresponding to the Dirac sea contribution, while the blue dashed line indicates the sum $f_{vac} + f_{med}$ at $T = 0$ and $\mu = 600$ MeV. The two lines coincide above $E = \mu$, since the medium does not contribute beyond that point. Right: Density of states $\rho(E, M, Q)$ relative to the restored case, $\rho_{rest}(E) \equiv \rho(E, 0, 0)$, for homogeneous condensates with $M = 300$ MeV (red dashed line), $M = 100$ MeV (green dash-dotted line), and for a CDW with $M = 100$ MeV, $Q = 1000$ MeV (blue solid line).

the wave number Q of the CDW. In particular we note that only the function f_{vac} depends on the regularization whereas only the density of states depends on the wave number.

Since the condensate term always disfavors (homogeneous or inhomogeneous) chiral symmetry breaking, a necessary condition for a non-trivial phase is that the first term is negative, *i. e.* the integral must be positive. The functions which enter the integrand are displayed in Fig. 6.3 for several cases. As shown in the left panel, the Pauli-Villars regularized vacuum function f_{vac} (red solid line) is negative for all energies. Hence, in vacuum, the density of states minus its value for the chirally restored solution should be negative as well to obtain a positive integrand. Indeed, as seen on the right, for $Q = 0$ the difference $\rho - \rho_{rest}$ is always negative and its absolute value increases with increasing M . Thus, a larger constituent quark mass leads to an increase of the free-energy gain in the kinetic term, which is stabilized by the condensate term at some optimum value of M . This is the usual mechanism for spontaneous chiral symmetry breaking in vacuum.

In contrast to f_{vac} , the function f_{med} is positive. Hence, when medium effects are included, the sum $f_{vac} + f_{med}$ becomes less and less negative at small energies until it eventually changes sign. As an example the case $T = 0$, $\mu = 600$ MeV is shown in the left panel of Fig. 6.3 (blue dashed line). Since at $T = 0$ the medium only contributes to energies $E < \mu$, the sum $f_{vac} + f_{med}$ remains negative at large energies, but altogether the formation of homogeneous condensates, related to a negative function $\rho - \rho_{rest}$, becomes

progressively disfavored by the medium contributions, thus leading to chiral restoration if we restrict ourselves to $Q = 0$.

The situation changes, however, when we allow for a CDW with $Q > 2M$. In this case $\rho - \rho_{rest}$ is *positive* at small energies and changes sign at $E \approx Q/2 - M^2/(2Q)$ (see Fig. 6.3, blue solid line on the right). Hence, by properly choosing Q , it can be achieved that the factors $f_{vac} + f_{med}$ and $\rho - \rho_{rest}$ have the same sign for all energies, thus more or less optimizing the free energy gain in the kinetic part of the thermodynamic potential. As $f_{vac} + f_{med}$ changes sign slightly below $E = \mu$ at large μ , this estimate yields $Q \approx 2\mu$ for the favored value.

These arguments support the statement that the formation of an inhomogeneous chiral condensate is a medium-induced effect [58, 61, 54]. In our case it is technically related to the fact that both, $\rho - \rho_{rest}$ with $Q > 2M$ and f_{med} , are positive at small energies. Therefore, since none of these functions but only the vacuum term is affected by the regularization, the appearance of the continent does not immediately look like a regularization artifact.

Of course, the dynamical formation of the inhomogeneous condensate eventually depends on the interplay of f_{vac} and f_{med} , and the explicit expression for the Dirac sea term will naturally influence the quantitative details. For example, by allowing for a larger cutoff Λ , the vacuum part becomes larger and the second continent is shifted to higher chemical potentials. However, the same is true for the standard chiral phase transition between homogeneous phases, where this is usually not considered to be a major problem.

The existence of the inhomogeneous continent is not restricted to Pauli-Villars regularization, but the very same behavior is also present when the vacuum term is regularized following the Schwinger proper-time prescription (described in Appendix C.2.3). On the other hand, when the thermodynamic potential is regularized by introducing a three-momentum cutoff, it is clear that a restriction of the in- and outgoing momenta also restricts the size of the wave number to which they can couple. Hence, large values of Q are strongly disfavored and the second inhomogeneous phase, if it exists at all, cannot extend to arbitrary large values of μ . However, unlike the previous examples, this is *obviously* a regularization effect, since the suppression of large Q is directly caused by the cutoff, and for this reason the authors of Ref. [70] introduce a form factor which restricts the quark momenta to the vicinity of the Fermi surface, rather than to small absolute values.

An example where large values of Q are suppressed in a seemingly more physical way is the quark-meson model. For the CDW ansatz, which in the QM model reads

$$\sigma(\mathbf{x}) = f_\pi \cos(\mathbf{Q} \cdot \mathbf{x}), \quad \pi^3(\mathbf{x}) = f_\pi \sin(\mathbf{Q} \cdot \mathbf{x}), \quad (6.2)$$

the kinetic term of the mesons in Eq. (2.40) yields a contribution

$$\Omega_{kin}^{mesons} = \frac{1}{2} f_\pi^2 Q^2, \quad (6.3)$$

which suppresses large values of Q (see Ref. [26] for more details). As a result, a numerical investigation seems to indicate that the inhomogeneous continent is not present in the QM model.

From this one might naively conclude that the emergence of the continent in the NJL model is due to the absence of derivative terms in the Lagrangian. However, it is well known that in the NJL model the contribution Eq. (6.3) is already contained in the vacuum part of the thermodynamic potential, which carries a dependence on Q through the energy spectrum [26, 54, 107]. Indeed, if one expands

$$\Omega_{vac}(M, Q) = \Omega_{vac}(M, 0) + \beta_{vac,2} Q^2 + \beta_{vac,4} Q^4 + \dots \quad (6.4)$$

one can show in a regularization independent way that the so-called spin stiffness is given by

$$\beta_{vac,2} = \frac{1}{2} f_\pi^2, \quad (6.5)$$

giving rise to a term like Eq. (6.3) in the thermodynamic potential. Hence, if we were allowed to neglect all other terms in Eq. (6.4), we could conclude that large values of Q and, thus, the inhomogeneous continent are suppressed in the same way as in the QM model. However, in the continent region, Q is certainly not small (compared with M or f_π). In any case, it is clear that the stability against large values of Q cannot be discussed in terms of a Taylor expansion for small Q .

We therefore look at the higher orders in the series in order to get an idea how these additional contributions (which become more and more relevant at higher values of Q) influence the previous considerations. In particular the coefficient of the Q^4 -term is dimensionless and therefore expected to stay finite, even if the cutoff is sent to infinity. For instance, if we employ proper-time regularization (see Appendix C.2.3), we obtain

$$\beta_{vac,4} = -2N_f N_c e^{-M^2/\Lambda^2} \frac{\Lambda^2 - M^2}{192\Lambda^2 \pi^2} = -\frac{N_f N_c}{81\pi^2} + \mathcal{O}\left(\frac{M^2}{\Lambda^2}\right). \quad (6.6)$$

The most important observation is that this term is negative, *i.e.* it weakens the effect of the Q^2 -term. Although the value of the coefficient is relatively small, the Q^4 -term dominates the Q^2 -term when Q is of the order of 10 times f_π .

In Fig. 6.4 we compare the full proper-time regularized vacuum thermodynamic potential with the results of a Taylor expansion to the orders Q^2 and Q^4 . In agreement with our considerations above, the Q^2 -result gets reduced by the higher orders. Although the effect is overestimated by the Q^4 -term, this leads to a much more moderate increase of Ω_{vac} in the continent region. As a consequence, the vacuum contributions do not disfavor the formation of a CDW strongly enough in this region to compete with the favoring effects of the medium contributions.

A very systematic investigation of the large- Q behavior of the vacuum effective potential has been performed more than 20 years ago in Ref. [108]. Although it turned out that the exact behavior beyond the universal Q^2 -order is strongly regularization dependent, in all cases considered, Ω_{vac} eventually becomes negative, meaning that even the vacuum is unstable against the formation of a CDW with very large Q . While this is clearly unphysical and should therefore be ignored, there is no reason why corrections to the Q^2 -terms should not be present at all. Unfortunately, these corrections are very model dependent and theoretical input from outside is needed to pin them down. In fact, inhomogeneous

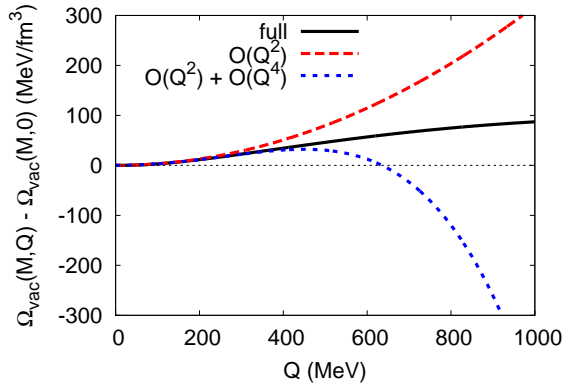


Figure 6.4.: Proper-time regularized vacuum thermodynamic potential for a CDW with fixed amplitude $M = 100$ MeV as a function of the wave number Q , using parameters from [54]. The value for $Q = 0$ has been subtracted. The full result (black solid line) is compared with the Taylor series truncated at order Q^2 (red dashed line) and order Q^4 (blue dotted line).

phases at arbitrary large μ have been predicted for the $1 + 1$ -dimensional Gross-Neveu model [50] as well as for QCD in the large- N_c limit [56]¹. Therefore, the continent may be not as exotic as it appears.

6.2. Favored phase at high densities

As mentioned in the introduction, recent quarkyonic-matter studies suggest that increasing the chemical potential leads to the formation of higher-dimensional chiral crystalline structures with growing geometrical complexity [70]. While no definite scale was given, this could be a hint that the chemical potentials considered so far are too low for two-dimensional crystals to be favored. This motivates us to extend our investigations to higher values of μ .

Of course, we have to keep in mind that the NJL model is a low-energy effective model with a limited range of validity. In particular, since the continent appears in a region where the chemical potential is of the order of the regulator masses, we have to be cautious not to overinterpret the results. However, as thoroughly discussed in the previous section, although the inhomogeneous continent is sensitive to regularization effects, it is not obviously created by them.

Here we simply take the inhomogeneous continent as a “model laboratory” to study the competition of one- and two-dimensional chiral crystals as a function of μ . To this end, we use a slightly modified parameter set with a vacuum constituent quark mass of 330 MeV (parameter values are reported in Appendix D.1). Without modifying any other qualitative behavior of the model, this has the advantage that the inhomogeneous island

¹For $N_c = 3$, they are, however, disfavored against color superconductivity [57].

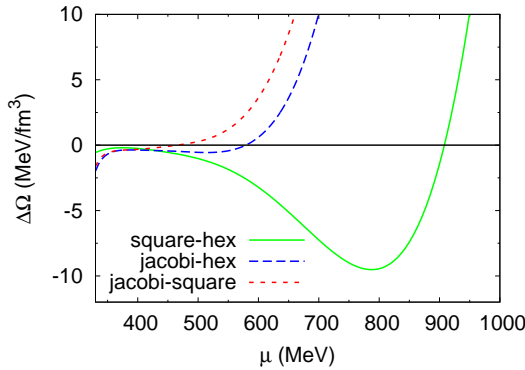


Figure 6.5.: Free-energy differences between inhomogeneous phases with different modulations, evaluated at $T = 0$.

merges with the continent (as shown in Fig. 6.2), so that the comparison of the different crystalline phases can be performed on a continuous interval, without being interrupted by the restored phase.

In Fig. 6.5 the differences between the free energies of three inhomogeneous phases with different modulations are displayed as functions of μ . As we have seen before, at low chemical potentials the two-dimensional crystals are disfavored against the one-dimensional domain-wall soliton lattice. Above $\mu \approx 450$ MeV, however, the two-dimensional square lattice leads to a lower free energy. At $\mu \approx 600$ MeV, the hexagon surpasses the one-dimensional modulation as well, and finally becomes the most favored shape at $\mu \approx 900$ MeV. Thus, while being aware that the model cannot be trusted blindly in this high density region, it is nevertheless remarkable that we recover the same sequence of crystalline phases as described in Ref. [70].

7. Conclusions

In this work we have investigated inhomogeneous chiral symmetry breaking phases within the NJL model.

As a first step, we developed within the usual mean-field approach a systematic way for evaluating the grand canonical thermodynamic potential associated with different kinds of spatial modulations of the chiral condensate, involving the diagonalization of an effective Hamiltonian operator. By limiting ourselves to lower-dimensional modulations and exploiting the Lorentz invariance of the system, we have been able to reduce the calculation of the energy spectrum of the model to the diagonalization of simpler Hamiltonians. The assumption of an underlying crystalline structure furthermore allowed us to factorize our problem in a similar way to what is described by Bloch's theorem in solid state physics, so that a comprehensive numerical analysis could be performed.

With these tools at hand, we determined the appearance of an inhomogeneous island in the phase diagram, in agreement with previous studies on chiral crystalline phases [61, 54, 62].

The emergence of this island at intermediate densities, close to and beyond the usual chiral restoration transition for homogeneous phases suggests that in presence of a Fermi sea of quarks the dominant mechanism for chiral condensation becomes no longer the usual quark-antiquark pairing, but rather the formation of quark-hole pairs, characterized by a finite momentum.

We then compared the free energies of different kinds of spatial modulations, in order to determine which crystalline shape is favored in the inhomogeneous phase. One of our main results is the finding that at zero temperature and intermediate chemical potentials, in the region where the chiral phase transition would take place if the analysis was restricted to homogeneous condensates, the most favored shape of the chiral condensate is that of a one-dimensional domain-wall lattice expressed in terms of Jacobi elliptic functions, leading to a solitonic shape of the chiral condensate close to the transition from the chirally broken phase. The would-be first order phase transition obtained when restricting the analysis to homogeneous phases only is then completely surrounded by an inhomogeneous phase, which is delimited by second-order lines joining at a Lifshitz point, which coincides with the previous location of the critical point.

In this region, we find that two-dimensional modulations are disfavored against one-dimensional ones, indicating that their greater kinetic energy cost is not sufficiently compensated by a larger gain in condensation energy. Supporting this consideration, we find that a hexagonal structure, is even less favored than the simpler square lattice in this regime. Moreover, since a Ginzburg-Landau analysis has revealed that also close to the Lifshitz point phases with higher-dimensional modulations are disfavored against one-dimensional ones [88], we do not expect that higher-dimensional structures appear at

finite temperature, at least in mean-field approximation. A numerical analysis to confirm these expectations would of course be desirable. Even though in light of our results it appears that higher dimensional structures are disfavored when compared to one-dimensional ones, without a complete numerical study we cannot rule out the possibility that three-dimensional crystalline structures might form the favored ground state for quark matter. In particular, the picture of particles sitting in localized “bags” (a generalization of the results of Sec. 4.2 to three-dimensional structures) looks particularly attractive, and with an appropriate description of confinement it could in principle be employed to describe nuclear matter starting from its quark content.

Although being favored in mean-field approximation, it is worth recalling that strictly speaking one-dimensional modulations of the order parameter are washed out by thermal fluctuations at finite temperature [92]. This statement refers to the fact that the modulation is not rigid, but fluctuates locally. The system’s spatially modulated nature is however still encoded in the behavior of long range correlations [93].

Once having determined the favored shape for the chiral condensate, we have analyzed the role of the isoscalar-vector interaction and the dynamics of the Polyakov loop on this kind of inhomogeneous ground state. When extending the model including a repulsive vector interaction, we found significant qualitative modifications of the phase structure: in contrast to the critical point when limiting to homogeneous phases, the Lifshitz point is not shifted towards smaller temperatures when increasing the strength of the vector interaction, but remains at the same temperature and density. Moreover, the domain of inhomogeneous ground states in the $\mu-T$ phase diagram increases. Since the Lifshitz point therefore no longer coincides with the critical point, the critical behavior in its vicinity and also near the phase transition lines to the inhomogeneous phase changes. This is underlined by the fact that the number susceptibilities remain finite, *i.e.* there are no singularities.

Our investigation of this part is complemented by an extensive numerical study, including the determination of density profiles in the inhomogeneous phase, the phase diagram when only allowing for chiral spirals, the evaluation of number susceptibilities and the incorporation of finite current quark masses. Furthermore, we performed a generalized Ginzburg-Landau expansion for elaborating the dependence of Lifshitz and critical point on the vector interaction. Part of this comprehensive study is also motivated in order to back up an approximation employed within our mean-field calculation, namely to use the spatially averaged number density when evaluating the thermodynamic potential. A fully self-consistent analysis considering a spatially modulated density as well as the spatial parts of the vector condensate would of course be most desirable, and for one-dimensional modulations is expected to be numerically feasible.

Probably less spectacular but nevertheless worth checking is the behavior of our model when the quarks are coupled to the Polyakov loop in order to suppress their contribution to the thermodynamic potential in chirally broken phases, thus mimicking confinement. This effect mostly leads to a stretch in the temperature direction of the $\mu-T$ phase diagram, similar to the case of homogeneous phases. This implementation of the PNJL model for inhomogeneous phases has also been used as a starting point to study the effects of the number of colors on these chiral crystalline structures. The large N_c extension of the model

is however not unique, and improvements on the approximation used could be possible. Aside from that, our PNJL implementation always implies a spatially constant expectation value of the Polyakov loop, and it would be interesting to relax this assumption.

As a final step, we analyzed the phase structure of the model at higher chemical potentials. The most striking result is the appearance of a second inhomogeneous phase, seemingly extending to arbitrarily high chemical potentials. Although this may appear to be a regularization artifact, we argue that it should rather be interpreted as a characteristic feature of the NJL model which might have physical relevance.

In this region, beyond a given value of chemical potential, we find that the structure of the ground state changes from having one-dimensional modulations to a two-dimensional square lattice and, at even higher μ , to an hexagonal shape. Although the results must not be trusted blindly in this high-density regime, which lies at the edge of the expected range of validity of the model, we find it nevertheless noteworthy that we reproduce qualitatively the behavior recently proposed for quarkyonic matter [70]. Quasicrystalline structures with discrete rotational symmetries higher than six, which have also been discussed in Ref. [70], are much more difficult to implement in our model since we heavily rely on the translational periodicity to perform our numerical calculations. These structures are anyway expected to appear only at even higher chemical potentials. It is also interesting that a similar sequence of phases was predicted for a 2D superconductor in a magnetic field [42].

In conclusion, although we recognize that the NJL model has several limitations and that the regularization procedure may in principle affect its results, our findings seem to suggest that inhomogeneous chiral symmetry breaking phases may play a more relevant role than expected in the QCD phase diagram. In this sense, our complementary study using the Quark-Meson model seems to support the picture of an inhomogeneous region appearing in the phase diagram. We recall in any case that all calculations were performed at the mean-field level, and that a systematic improvement to include fluctuations would be a logical next step to make our calculations more realistic.

We also note that the intermediate density region where the inhomogeneous island appears may be relevant for the physics of compact stellar objects like neutron stars, and that the resulting equation of state might be compared with present astrophysical data. In order to provide reliable predictions for this kind of system however our model study should first implement charge neutrality. This is typically done by enforcing different chemical potentials for the up and down quark species, and can in principle be implemented within our setup. Furthermore, in this range of densities the strange quark may become a relevant degree of freedom, and an extension of the model to three flavors would also be an interesting next step.

Finally, we note that this chemical potential region may belong to the realm of color superconductivity as well, and it would therefore be necessary to study the competition of inhomogeneous chiral condensation with diquark pairing as well. A combination of the present study with the one developed in [38] for inhomogeneous color-superconductors might predict the formation of a “mixed” phase where diquarks condense in the chirally restored bags described in Sec. 4.2. This is a fascinating possibility which is definitely worth investigating.

A. Conventions

Throughout the whole thesis, natural units have been employed:

$$\hbar = c = k_B = 1. \quad (\text{A.1})$$

Greek letters μ, ν, \dots indicate Lorentz indices running from 0 to 3. We always make use of the Einstein convention, for which we sum over repeated indices.

Our convention for the Minkowski metric is

$$\eta_{\mu\nu} = \text{diag}\{1, -1, -1, -1\}. \quad (\text{A.2})$$

Scalar products of four-vectors assume then the form

$$x \cdot p = x^\mu p_\mu = x^0 p_0 + x^i p_i = x^0 p_0 - \mathbf{x} \cdot \mathbf{p}. \quad (\text{A.3})$$

In our calculations, we mainly use the chiral representation for the Dirac matrices:

$$\gamma^0 = \begin{pmatrix} 0 & 1 \\ 1 & 0 \end{pmatrix}, \quad \gamma^k = \begin{pmatrix} 0 & \sigma^k \\ -\sigma^k & 0 \end{pmatrix}, \quad \gamma^5 = \begin{pmatrix} -1 & 0 \\ 0 & 1 \end{pmatrix}, \quad (\text{A.4})$$

$$\gamma^0 \gamma^k = \begin{pmatrix} -\sigma^k & 0 \\ 0 & \sigma^k \end{pmatrix}, \quad \gamma^0 \gamma^5 = \begin{pmatrix} 0 & 1 \\ -1 & 0 \end{pmatrix}, \quad (\text{A.5})$$

and here σ^i are Pauli matrices:

$$\sigma^1 = \begin{pmatrix} 0 & 1 \\ 1 & 0 \end{pmatrix}, \quad \sigma^2 = \begin{pmatrix} 0 & -i \\ i & 0 \end{pmatrix}, \quad \sigma^3 = \begin{pmatrix} 1 & 0 \\ 0 & -1 \end{pmatrix}. \quad (\text{A.6})$$

Some common abbreviations that appear in the thesis are:

- CP : Critical point
- LP : Lifshitz point
- BZ : Brillouin zone
- RL : Reciprocal lattice
- QM : Quark-meson (model)
- GL : Ginzburg-Landau

B. Details on the formalism

In this appendix we present more details on the calculations performed in chapter 2.

B.1. Mean-field Lagrangian

In order to obtain expression Eq. (2.9) from Eq. (2.6), we expand the field bilinears around their expectation values. We take the scalar channel as template and define $\phi(x) = \langle \bar{\psi}\psi \rangle$, then write (in the following we will for brevity omit the x dependence of the quantities of interest)

$$\bar{\psi}\psi = \phi + \delta\phi \rightarrow \delta\phi = \bar{\psi}\psi - \phi, \quad (\text{B.1})$$

from which

$$\begin{aligned} (\bar{\psi}\psi)^2 \approx \phi^2 + 2\delta\phi\phi &= \phi^2 + 2\phi\bar{\psi}\psi - 2\phi^2 \\ &= 2\phi\bar{\psi}\psi - \phi^2. \end{aligned} \quad (\text{B.2})$$

With this substitution for both the scalar and pseudoscalar bilinears, the mean-field Lagrangian becomes

$$\mathcal{L}_{MF} = \bar{\psi}(i\gamma^\mu\partial_\mu - m + 2G_S(\phi_S + i\gamma^5\tau_a\phi_P^a))\psi - G_S(\phi_S^2 + \phi_P^a)^2. \quad (\text{B.3})$$

B.2. Inverse propagator in momentum space

We review here in more detail the required steps to obtain an expression for the mean-field inverse quark propagator in momentum space. For this, we start from the definition of the euclidean action,

$$\begin{aligned} \mathcal{S}_E &= \int_{\mathbf{x} \in [0, \frac{1}{T}] \times V} d\tau d\mathbf{x} (\mathcal{L}_{MF}(t = -i\tau, \mathbf{x}) + \mu\bar{\psi}\gamma^0\psi) \\ &= \int_{\mathbf{x} \in [0, \frac{1}{T}] \times V} d\tau d\mathbf{x} [\bar{\psi}(x)S^{-1}(x)\psi(x) + \mathcal{V}] \\ &\equiv \mathcal{S}_E^{kin} + \mathcal{S}_E^{cond}, \end{aligned} \quad (\text{B.4})$$

where in the last line we isolated the condensate part $\mathcal{S}_E^{cond} = \int_{\mathbf{x} \in [0, \frac{1}{T}] \times V} d\tau d\mathbf{x} \mathcal{V}$. If we now consider only the first part and plug in the expression (Eq. (2.10)) for the inverse

quark propagator $S^{-1}(x)$, with the spinors written as Fourier expansions (Eq. (2.25) and Eq. (2.26)), we obtain

$$\mathcal{S}_E^{kin} = \frac{1}{V} \int d\mathbf{x} d\tau \sum_{\omega_n \omega_m} \sum_{\mathbf{p}_m \mathbf{p}_n} \bar{\psi}_{p_m} e^{ip_m x} [i\gamma^\mu \partial_\mu - M(\mathbf{x}) + \gamma^0 \mu] \psi_{p_n} e^{-ip_n x} \quad (\text{B.5})$$

$$\begin{aligned} &= \frac{1}{V} \int d\mathbf{x} d\tau \sum_{\omega_n \omega_m} \sum_{\mathbf{p}_m \mathbf{p}_n} \bar{\psi}_{p_m} e^{i(\omega_m \tau - \mathbf{p}_m \cdot \mathbf{x})} \left[i\gamma_\mu (-ip_n^\mu) - \sum_{\mathbf{k}_n} M_{k_n} e^{i\mathbf{k}_n \cdot \mathbf{x}} + \gamma^0 \mu \right] \psi_{p_n} e^{-i(\omega_n \tau - \mathbf{p}_n \cdot \mathbf{x})} \\ &= \frac{1}{V} \int d\mathbf{x} d\tau \sum_{\omega_n \omega_m} \sum_{\mathbf{p}_m \mathbf{p}_n} e^{i(\omega_m - \omega_n)\tau} \bar{\psi}_{p_m} e^{-i\mathbf{p}_m \cdot \mathbf{x}} \left[\not{p}_n - \sum_{\mathbf{k}_n} M_{k_n} e^{i\mathbf{k}_n \cdot \mathbf{x}} + \gamma^0 \mu \right] \psi_{p_n} e^{i\mathbf{p}_n \cdot \mathbf{x}}, \end{aligned}$$

at this point one can recognize a representation of the Kronecker delta in the complex exponentials involving the Matsubara frequencies,

$$\int d\tau e^{i(\omega_m - \omega_n)\tau} = \frac{1}{T} \delta_{\omega_n, \omega_m}, \quad (\text{B.6})$$

and write

$$\mathcal{S}_E^{kin} = \frac{1}{V} \frac{1}{T} \int d\mathbf{x} \sum_{\omega_n} \sum_{\mathbf{p}_m \mathbf{p}_n} \bar{\psi}_{p_m} e^{-i\mathbf{p}_m \cdot \mathbf{x}} \left[i\gamma^0 \omega_n - \boldsymbol{\gamma} \cdot \mathbf{p}_n - \sum_{\mathbf{k}_n} M_{k_n} e^{i\mathbf{k}_n \cdot \mathbf{x}} + \gamma^0 \mu \right] \psi_{p_n} e^{i\mathbf{p}_n \cdot \mathbf{x}},$$

then factor out a γ^0 , recalling that $(\gamma^0)^2 = 1$:

$$= \frac{1}{V} \frac{1}{T} \int d\mathbf{x} \sum_{\omega_n} \sum_{\mathbf{p}_m \mathbf{p}_n} \bar{\psi}_{p_m} e^{-i\mathbf{p}_m \cdot \mathbf{x}} \gamma^0 \left[i\omega_n - \gamma^0 \boldsymbol{\gamma} \cdot \mathbf{p}_n - \gamma^0 \sum_{\mathbf{k}_n} M_{k_n} e^{i\mathbf{k}_n \cdot \mathbf{x}} + \mu \right] \psi_{p_n} e^{i\mathbf{p}_n \cdot \mathbf{x}},$$

and finally recognize again another delta representation in the exponential of spatial momenta,

$$= \frac{1}{V} \frac{1}{T} \sum_{\omega_n} \sum_{\mathbf{p}_m \mathbf{p}_n} \bar{\psi}_{p_m} \gamma^0 \left[i\omega_n \delta_{\mathbf{p}_n, \mathbf{p}_m} - \gamma^0 \boldsymbol{\gamma} \cdot \mathbf{p}_n \delta_{\mathbf{p}_n, \mathbf{p}_m} - \gamma^0 \sum_{\mathbf{k}_n} M_{k_n} \delta_{\mathbf{p}_n, \mathbf{p}_m + \mathbf{k}_n} + \mu \delta_{\mathbf{p}_n, \mathbf{p}_m} \right] \psi_{p_n}.$$

We thus finally obtain the expression we employ for the effective action containing the inverse quark propagator in momentum space:

$$\begin{aligned}
\mathcal{S}_E^{kin} &= \frac{1}{T} \sum_{\omega_n} \sum_{\mathbf{p}_m \mathbf{p}_n} \bar{\psi}_{p_m} \gamma^0 \left[i\omega_n \delta_{\mathbf{p}_n, \mathbf{p}_m} - \gamma^0 \boldsymbol{\gamma} \cdot \mathbf{p}_n \delta_{\mathbf{p}_n, \mathbf{p}_m} - \gamma^0 \sum_{\mathbf{k}_n} M_{k_n} \delta_{\mathbf{p}_n, \mathbf{p}_m + \mathbf{k}_n} + \mu \delta_{\mathbf{p}_n, \mathbf{p}_m} \right] \psi_{p_n} \\
&\equiv \frac{1}{T} \sum_{\omega_n} \sum_{\mathbf{p}_m \mathbf{p}_n} \bar{\psi}_{p_m} S_{p_m, p_n}^{-1} \psi_{p_n} .
\end{aligned} \tag{B.7}$$

C. Regularization

This appendix is devoted to a more thorough discussion of different possible regularization schemes for the NJL model.

As mentioned already in chapter 2, the expression obtained for the thermodynamic potential involves a diverging sum over the energies of the system. Since the NJL model is non-renormalizable, unphysical divergencies cannot be reabsorbed in redefining the model parameters, and a regularization scheme has to be specified instead.

C.1. Isolating vacuum and medium contributions

The typical diverging expression we encounter in our calculations has the form

$$\int_{-\infty}^{\infty} dE \rho(E) T \log \left(2 \cosh \left(\frac{E - \mu}{2T} \right) \right), \quad (\text{C.1})$$

and contains both a divergent vacuum contribution f_{vac} , increasing like $|E|$, as well as a finite medium part f_{med} . As thoroughly discussed in chapter 3, the specific form of $\rho(E)$ will depend on the shape of the chiral condensate. It can be seen however that for big values of E the density of states will always grow like $\mathcal{O}(E^2)$ ¹.

The integrand of Eq. (C.1) can be rewritten as

$$T \log \left(2 \cosh \left(\frac{E - \mu}{2T} \right) \right) = T \log \left(e^{-\frac{E-\mu}{T}} + 1 \right) + \frac{E - \mu}{2}, \quad (\text{C.2})$$

we can also note at this point that the function in Eq. (C.2) is even in the argument $(E - \mu)$. This is obvious if we recall that the expression for the hyperbolic cosine is simply

$$\cosh(x) = \frac{e^x + e^{-x}}{2}. \quad (\text{C.3})$$

In order to single out the vacuum contributions, we must assume that the eigenvalue spectrum of the effective Hamiltonian is symmetric. This turns out to be the case for all kinds of modulations considered in this work. In particular, we can write (for simplicity in the following we will omit the density of states $\rho(E)$ as well as the integration variable dE)

¹A simple way of understanding this is to look at the density of states for the non-interacting massless particle case, which is simply given by $\rho(E) = E^2/\pi^2$, and realize that for asymptotically high energies (or equivalently momenta), the effects of chiral symmetry breaking, which no matter the pattern are always expected to be of order Λ_{QCD} , will always be negligible.

$$\begin{aligned}
& \int_{-\infty}^{\infty} T \log \left[2 \cosh \left(\frac{E - \mu}{2T} \right) \right] \\
&= \int_{-\infty}^{\infty} T \log \left\{ \exp \left(\frac{E - \mu}{2T} \right) + \exp \left(-\frac{E - \mu}{2T} \right) \right\} \\
&= \int_{-\infty}^{\infty} T \left\{ \log \left[\exp \left(\frac{E - \mu}{2T} \right) \right] + \log \left[1 + \exp \left(-\frac{E - \mu}{T} \right) \right] \right\} \\
&= \int_{-\infty}^{\infty} T \left\{ \frac{E - \mu}{2T} + \log \left[1 + \exp \left(-\frac{E - \mu}{T} \right) \right] \right\} \\
&= \int_0^{\infty} T \left\{ \frac{E - \mu + (-E - \mu)}{2T} + \log \left[1 + \exp \left(-\frac{E - \mu}{T} \right) \right] + \log \left[1 + \exp \left(-\frac{-E - \mu}{T} \right) \right] \right\} \\
&= \int_0^{\infty} T \left\{ \frac{-\mu}{T} + \log \left[1 + \exp \left(-\frac{E - \mu}{T} \right) \right] + \log \left[\exp \left(\frac{E + \mu}{T} \right) \left(\exp \left(-\frac{E + \mu}{T} \right) + 1 \right) \right] \right\} \\
&= \int_0^{\infty} \left\{ E + T \log \left[1 + \exp \left(-\frac{E - \mu}{T} \right) \right] + T \log \left[1 + \exp \left(-\frac{E + \mu}{T} \right) \right] \right\}, \tag{C.4}
\end{aligned}$$

which is a familiar expression from homogeneous NJL in which the first term denotes the diverging vacuum contribution.

The zero temperature limit of Eq. (C.2) is given by

$$T \log \left(2 \cosh \left(\frac{x - \mu}{2T} \right) \right) \xrightarrow{T \rightarrow 0} \frac{|E - \mu|}{2}. \tag{C.5}$$

This can be seen immediately by expanding the cosh in two exponentials and by observing that only one of them survives in the limit $T \rightarrow 0$, according to the sign of $(E - \mu)$. If we now again assume that the energy spectrum is symmetric around zero, we can rewrite the expression for Eq. (C.1) at zero temperature as

$$\begin{aligned}
\int_{-\infty}^{\infty} \frac{|E - \mu|}{2} &= \int_0^{\infty} \frac{|E - \mu|}{2} + \int_0^{\infty} \frac{|-E - \mu|}{2} \\
&= \int_0^{\mu} \frac{\mu - E}{2} + \int_{\mu}^{\infty} \frac{E - \mu}{2} + \int_0^{\infty} \frac{E + \mu}{2} \\
&= \frac{1}{2} \left\{ \int_0^{\infty} E + \int_0^{\infty} \mu + \int_0^{\mu} (\mu + E) + \int_{\mu}^{\infty} (E - \mu) - 2 \int_0^{\mu} E \right\} \\
&= \int_0^{\infty} E + \int_0^{\mu} (\mu - E), \tag{C.6}
\end{aligned}$$

where in the second last line $-E$ has been rewritten as $E - 2E$. This is the standard result found for homogeneous NJL for zero temperature.

Having now isolated the vacuum contributions from the medium ones, we can consider different regularization schemes.

C.2. Regularization schemes

C.2.1. Three-momentum cutoff

The energy sum in Eq. (2.33) can be effectively rewritten as an integral over quark momenta. This is the standard procedure when dealing with homogeneous phases, where the inverse quark propagator is diagonal in momentum space and each energy is basically that of a free quasiparticle dressed with a constituent mass and characterized by a well-defined momentum: $E = \sqrt{\mathbf{p}^2 + M^2}$. The simplest and most widely employed regularization scheme in NJL model studies consists of imposing a sharp cutoff $\Lambda_{O(3)}$ on the magnitude of the maximum allowed momentum for the quarks. Typical values for this sharp cutoff are of a few hundred MeV [77, 18]. The expression for the thermodynamic potential in this case becomes

$$\Omega_{kin}^{O(3)} \propto \int_{|\mathbf{p}| < \Lambda_{O(3)}} d^3 p T \log \left(2 \cosh \left(\frac{E(\mathbf{p}) - \mu}{2T} \right) \right). \quad (\text{C.7})$$

This obviously renders all expressions finite, and can be interpreted as a crude implementation of the asymptotic freedom property, since quarks are expected to interact weakly at high momenta. This naive interpretation however clearly fails when dealing with inhomogeneous condensates, since the quark momenta are not fixed and the quasi-particle energies can no longer be labeled by a conserved three-momentum. For inhomogeneous pairing, the practical implementation of such a scheme would involve a cut on the maximum allowed momenta $\mathbf{p}_m, \mathbf{p}_n$ in the effective Hamiltonian, Eq. (2.30). Such a cut will however artificially reduce the phase space for the formation of a crystalline condensate, which may be expected to carry a momentum $Q \approx \Lambda_{O(3)}$, and will seriously limit any possibility for inhomogeneous pairing.

For this reason, more refined methods which mostly act on the quark energies rather than momenta are the preferred choice when dealing with inhomogeneous phases.

C.2.2. Free energy regularization

An alternative and less constraining regularization scheme acting on the particle energies rather than momenta may be introduced by going back to the expression for the thermodynamic potential Eq. (2.31) and replacing the logarithm by its Schwinger proper-time representation,

$$\log A \rightarrow - \int_0^\infty \frac{d\tau}{\tau} f(\tau) e^{-\tau A}, \quad (\text{C.8})$$

where we introduced a blocking function $f(\tau)$ as a regulator. Thus, our regularization scheme is defined by specifying $f(\tau)$.

The most simple prescription would be to put a lower bound in the proper-time variable, $f(\tau) = \theta(\tau - 1/\Lambda^2)$. However, as we would like to keep a structure which allows us to perform the Matsubara sum analytically, we prefer the function

$$f(\tau) = 1 - 3e^{-\tau\Lambda^2} + 3e^{-2\tau\Lambda^2} - e^{-3\tau\Lambda^2}. \quad (\text{C.9})$$

Inserting this into Eq. (C.8), this amounts to the replacement

$$\log A \rightarrow \log A - 3 \log(A + \Lambda^2) + 3 \log(A + 2\Lambda^2) - \log(A + 3\Lambda^2), \quad (\text{C.10})$$

and we can carry out the Matsubara sum in the usual way. The regularized version of Eq. (2.33) then reads:

$$\Omega(T, \mu) = \int dE \rho(E) \sum_{j=0}^3 c_j \left\{ E_\mu^j + 2T \log \left(1 + e^{-E_\mu^j/T} \right) \right\} + \Omega_{\text{cond}}, \quad (\text{C.11})$$

where $c_0 = -c_3 = 1$, $c_1 = -c_2 = 3$ and

$$E_\mu^j = \sqrt{E_\mu + j\Lambda^2}, \quad E_\mu = E - \mu. \quad (\text{C.12})$$

This kind of prescription is similar to the Pauli-Villars regularization. Note, however, that according to Eq. (C.12) we replace the *free energies* in a Pauli-Villars-like manner, which is not exactly the same as introducing regulator particles with large masses, as in the standard Pauli-Villars regularization.

A shortcoming of this kind of prescription is that the obtained value for the constituent quark mass acquires an unwanted dependence on the chemical potential, which is included in our definition of the free energy. As such, this regularization method will not be employed in the following.

We finally note that the replacement Eq. (C.8) is not exact. Indeed, we know that

$$-\int_{\tau_{\text{low}}}^{\infty} \frac{d\tau}{\tau} e^{-\tau A} = -\Gamma(0, \tau_{\text{low}} A) = \gamma_E + \log(\tau_{\text{low}} A) + \mathcal{O}(\tau_{\text{low}}), \quad (\text{C.13})$$

where γ_E is the Euler-Mascheroni constant. It is however possible to see that the introduction of an appropriate blocking function removes the constant terms and allows to take the limit $\tau_{\text{low}} \rightarrow 0$. As a simple case, we can consider $f(\tau) = 1 - e^{-\tau\Lambda^2}$ and perform the integration on the right side of Eq. (C.8):

$$\begin{aligned} -\lim_{\tau_{\text{low}} \rightarrow 0} \int_{\tau_{\text{low}}}^{\infty} \frac{d\tau}{\tau} f(\tau) e^{-\tau A} &= -\lim_{\tau_{\text{low}} \rightarrow 0} \int_{\tau_{\text{low}}}^{\infty} \frac{d\tau}{\tau} \left(e^{-\tau A} - e^{-\tau(A+\Lambda^2)} \right) \\ &= \lim_{\tau_{\text{low}} \rightarrow 0} -\Gamma(0, \tau_{\text{low}} A) + \Gamma(0, \tau_{\text{low}}(A + \Lambda^2)) \\ &= \log\left(\frac{A}{A + \Lambda^2}\right) = \log(A) - \log(A + \Lambda^2). \quad (\text{C.14}) \end{aligned}$$

The constant terms and the τ_{low} parameter dependence in the logarithms cancel obviously for the blocking function Eq. (C.9) as well, leaving only the expression Eq. (C.10).

C.2.3. Vacuum proper-time regularization

In order to remove the artificial medium dependence obtained by regularizing the free energies, it is useful to take one step back and single out the diverging vacuum contributions to the thermodynamic potential from the medium effects. For this we follow [54]

and rewrite only the vacuum part of Ω using the Schwinger proper time representation of the logarithm. More specifically, using the zero temperature formalism Ω_{vac} (aside from a $2N_f N_c$ factor coming from the trace over spin, color, flavor) can be written as

$$\Omega_{vac} = - \int_C \frac{d^4 k}{i(2\pi)^4} \log A, \quad (C.15)$$

where, similarly to the previous section, A is basically the inverse quark propagator.

Inserting the proper time representation and Wick-rotating on k_0 , we get

$$\Omega_{vac} = \int_C \frac{d^4 k_E}{(2\pi)^4} \int_0^\infty \frac{ds}{s} e^{iAs}. \quad (C.16)$$

For the homogeneous case, this reduces to

$$\begin{aligned} \Omega_{vac}^{hom} &= \int_{-\infty}^\infty \frac{d^4 k_E}{(2\pi)^4} \int_0^\infty \frac{ds}{s} e^{i(-k_E^2 - \mathbf{k}^2 - M^2)s} \\ &= \int_{-\infty}^\infty \frac{d^4 k_E}{(2\pi)^4} \int_0^\infty \frac{d\tau}{\tau} e^{-(k_E^2 + \mathbf{k}^2 + M^2)\tau} \\ &= \int_0^\infty \frac{d\tau}{\tau^3} \frac{1}{16\pi^2} e^{-M^2\tau}. \end{aligned} \quad (C.17)$$

Inserting back the appropriate multiplicity factors, we arrive at

$$\Omega_{vac}^{hom} = \frac{N_f N_c}{8\pi^2} \int_0^\infty \frac{d\tau}{\tau^3} e^{-M^2\tau}. \quad (C.18)$$

Let us now consider for simplicity a one-dimensional modulation of the chiral condensate like the CDW, characterized by a wave vector \mathbf{Q} determining the size of the BZ. After exploiting the dimensional reduction procedure of Sec. 3.2.1 and integrating over transverse momenta, we are left with (inserting all the appropriate multiplicity factors)

$$\Omega_{vac}^{CDW} = \frac{N_f N_c}{8\pi^{3/2}} \int_0^\infty \frac{d\tau}{\tau^{5/2}} \int_0^Q \frac{dk}{2\pi} \sum_{\lambda > 0} e^{-\lambda^2\tau}, \quad (C.19)$$

with $\lambda(k)$ eigenvalues of the dimensionally reduced Hamiltonian. As a cross-check, we can obtain from here the homogeneous case (Eq. (C.18)), for which the integral over the BZ extends over the whole p_z range and

$$\lambda = \sqrt{p_z^2 + M^2} \quad (\text{twice degenerate}), \quad (C.20)$$

leading to

$$\Omega_{vac}^{hom} = \frac{N_f N_c}{16\pi^{5/2}} \int_0^\infty \frac{d\tau}{\tau^{5/2}} \int_{-\infty}^\infty dp_z 2 e^{-(p_z^2 + M^2)\tau}. \quad (C.21)$$

The p_z integral can be carried out analytically, leading to Eq. (C.18).

At this point, the simplest way to regularize the proper time integral involves introducing a sharp cut $1/\Lambda$ on the lowest allowed proper time. A possible value is reported in Appendix D.1.

C.2.4. Pauli-Villars

As mentioned already in Sec. 2.2.4, our preferred regularization scheme throughout this thesis is a Pauli-Villars regularization which we apply only to the diverging vacuum term. This amounts to the replacement [77]

$$f_{\text{vac}}(x) \rightarrow f_{\text{PV}}(x) = \sum_{j=0}^3 c_j \sqrt{x^2 + j\Lambda^2}, \quad (\text{C.22})$$

with $c_0 = 1$, $c_1 = -3$, $c_2 = 3$, $c_3 = -1$ and a cutoff scale Λ .

C.3. Parameter fitting

Having chosen a regularization scheme, we proceed to determining the model parameters G_S and Λ by fitting vacuum phenomenology. The typical procedure involves fitting values for the chiral condensate $\langle\bar{\psi}\psi\rangle$ and the pion decay constant. For Pauli-Villars those are given by [77]

$$\langle\bar{\psi}\psi\rangle = -\frac{3M_{\text{vac}}}{4\pi^2} \sum_{j=0}^3 c_j (M_{\text{vac}}^2 + j\Lambda^2) \log\left(\frac{M_{\text{vac}}^2 + j\Lambda^2}{M_{\text{vac}}^2}\right), \quad (\text{C.23})$$

$$f_\pi^2 = -\frac{N_c M_{\text{vac}}^2}{4\pi^2} \sum_{j=0}^3 c_j \log\left(\frac{M_{\text{vac}}^2 + j\Lambda^2}{M_{\text{vac}}^2}\right), \quad (\text{C.24})$$

where M_{vac} is the constituent mass for the chirally broken phase in the vacuum.

The NJL model with a proper-time regularization and adjusted to these quantities is however known to give constituent quark masses of around 200 MeV in vacuum. Hence it gives an undesired phenomenology with regard to the QCD phase diagram, since quasi-particles will start forming a Fermi surface at $\mu \approx M_{\text{vac}}$. This is phenomenologically unacceptable for $\mu \lesssim M_N/3 \approx 300$ MeV, where M_N is the nucleon mass. We instead fix our parameters by enforcing a value for the constituent quark mass M_{vac} and determine Λ by fitting Eq. (C.24) to the appropriate value of f_π , which in the chiral limit is taken to be 88 MeV [77]. We then determine the coupling G_S from the vacuum gap equation [77]

$$M_{\text{vac}} = \frac{1}{2\pi^2} G_S N_f N_c M_{\text{vac}} \sum_{j=0}^3 c_j (M_{\text{vac}}^2 + j\Lambda^2) \log\left(\frac{M_{\text{vac}}^2 + j\Lambda^2}{M_{\text{vac}}^2}\right). \quad (\text{C.25})$$

D. Parameter sets

D.1. NJL parameters

Throughout most of this work we choose a parameter set fitted to give a vacuum constituent quark mass of $M_{vac} = 300$ MeV. In Chapter 6 we however also perform calculations using parameters giving a vacuum constituent quark mass of $M_{vac} = 330$ MeV.

In table D.1 we report the parameter sets used for the Pauli-Villars regularization used in most of our NJL calculations, according to the enforced value for the vacuum constituent quark mass for a fixed $f_\pi = 88$ MeV.

M_{vac} (MeV)	Λ (MeV)	$G_S \Lambda^2$
300	757.048	6.002
330	728.368	6.599

Table D.1.: Parameter sets for Pauli-Villars regularization.

For the comparisons of chapter 6 involving the use of vacuum proper-time regularization as described in Sec. C.2.3, we use the parameters from [54]:

M_{vac} (MeV)	Λ (MeV)	$G_S \Lambda^2$
330	660.37	6.35

Table D.2.: Parameter set for vacuum proper time regularization.

D.2. QM parameters

For the quark-meson model, we fit the parameters to the pion-decay constant f_π , the constituent quark mass in the vacuum M_{vac} , the pion mass m_π and σ -meson mass m_σ through the relations

$$\begin{aligned} \langle \sigma \rangle &= f_\pi \ , & \langle \pi^a \rangle &= 0 \ , & c &= m_\pi^2 f_\pi \ , \\ g &= M_{vac}/f_\pi \ , & \lambda &= (m_\sigma^2 - m_\pi^2)^2/(2f_\pi^2) \ , & v^2 &= f_\pi^2 - m_\pi^2/\lambda \ . \end{aligned}$$

The parameter set we employed is reported in table D.3.

M_{vac} (MeV)	M_σ (MeV)	f_π (MeV)	M_π (MeV)
300	600	88	0

Table D.3.: Parameter set for the quark-meson model

D.3. PNJL parameters

For the Polyakov-loop potential, we adopt the parameters of Ref. [95], shown in table D.4. The parameter a is fixed by the condition that for pure gluo-dynamics the phase transition takes place at $T = 270$ MeV, while b is chosen to have a crossover around $T = 200$ MeV at $\mu = 0$ when quarks are included. Since we are mainly interested in the qualitative effect of the Polyakov loop, we did not perform a refit of b within our regularization scheme. We checked, however, that this parameter choice gives reasonable results for the behavior of the order parameters at $\mu = 0$.

a (MeV)	b (MeV 3)
664.0	$7.55 \cdot 10^6$

Table D.4.: Parameter set for the PNJL potential

E. More details on the solitonic solutions

For completeness, we review here some more details on the solitonic solutions introduced in Sec. 3.3.3. We recall that in the chiral limit the order parameter is given by

$$M(z) = \Delta\nu \frac{\text{sn}(\Delta z|\nu)\text{cn}(\Delta z|\nu)}{\text{dn}(\Delta z|\nu)}, \quad (\text{E.1})$$

where Δ is a scale parameter and sn , cn , dn are elliptic Jacobi functions with elliptic modulus ν . We furthermore note that this expression can be rewritten as

$$M(z) = \sqrt{\nu'}\Delta' \text{sn}(\Delta' z|\nu') \quad (\text{E.2})$$

where $\nu' = (\frac{1-\sqrt{1-\nu}}{1+\sqrt{1-\nu}})^2$ and $\Delta' = (1 + \sqrt{1-\nu})\Delta$.

This allows us to comment on the shape of the mass functions by simply plotting $\text{sn}(z|\nu)$ for different values of the elliptic modulus. We are in particular interested in what happens at the onset of the inhomogeneous phase, where ν varies from 1 to 0.9 in a chemical potential window of less than 10 MeV. For this, we plot in Fig. E.1 the function $\text{sn}(z|\nu)$ at several values of ν close to 1, to give an idea of how infinitely spaced solitons get close together as the elliptic modulus decreases. The period of these functions, plotted in Fig. E.2, is given by $4\mathbf{K}(\nu)$, with K complete elliptic integral of first kind. As can be seen from Fig. E.2, the period becomes infinite for $\nu \rightarrow 1$, as $\text{sn}(z|\nu)$ reduces to $\tanh(z)$. For more details on the Jacobi elliptic functions, we refer to standard texts on special functions like [109].

E.1. Density of states

For the solitonic solutions, the one-dimensional density of states is given by [45, 110]

$$\rho_{1D}(\lambda) = \begin{cases} \frac{1}{\pi} \frac{\lambda^2 - \Delta^2 \mathbf{E}(\nu)/\mathbf{K}(\nu)}{\sqrt{(\lambda^2 - \Delta^2)(\lambda^2 - (1-\nu)\Delta^2)}} & , (\lambda^2 - \Delta^2)(\lambda^2 - (1-\nu)\Delta^2) > 0 \\ 0 & , \text{else.} \end{cases} \quad (\text{E.3})$$

Within our dimensionally reduced framework (see Sec. 3.2.1), the evaluation of the thermodynamic potential for the full 3+1-dimensional system then reduces to evaluating expressions of the form

$$\tilde{\Omega} = \sum_{\lambda} \int \frac{d^2 \mathbf{p}_{\perp}}{(2\pi)^2} f \left(\lambda \sqrt{1 + \mathbf{p}_{\perp}^2/\lambda^2} \right), \quad (\text{E.4})$$

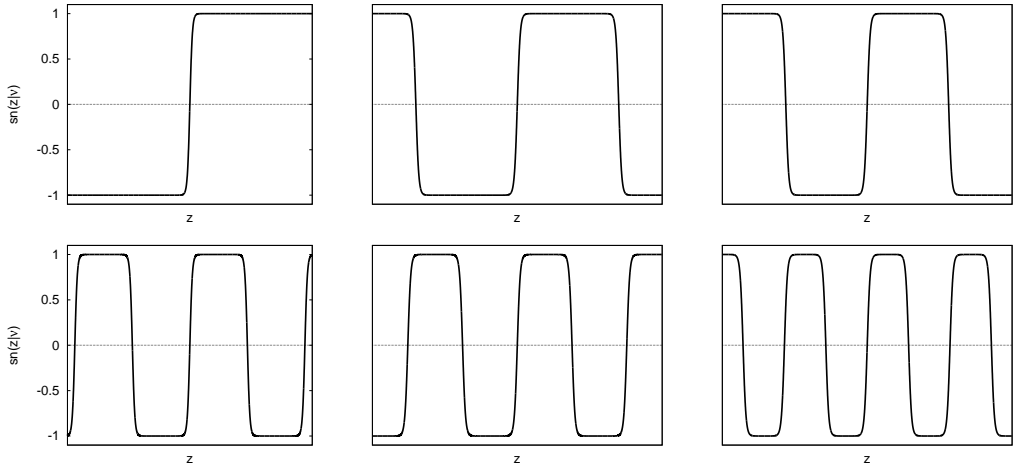


Figure E.1.: Shape of $\text{sn}(z|\nu)$ for several values of ν close to 1.

Top row: $\nu = 0.99999999999$, $\nu = 0.9999999999$, $\nu = 0.99999999$;

Bottom row: $\nu = 0.99999$, $\nu = 0.9999$, $\nu = 0.99$. The z scale is the same for all figures, ranging from $z = -50$ to 50 .

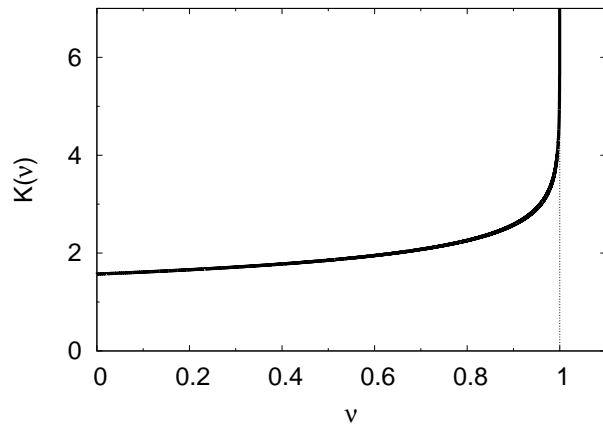


Figure E.2.: Quarter period for the elliptic functions, $L/4 = \mathbf{K}(\nu)$.

where $f(x)$ is an even function. After introducing the density of states of the GN model ρ_{1D} , we can rewrite this as

$$\tilde{\Omega} = 2 \int_{-\infty}^{\infty} d\lambda \int \frac{d^2 \mathbf{p}_\perp}{(2\pi)^2} \rho_{1D}(\lambda) f\left(sgn(\lambda) \sqrt{\lambda^2 + \mathbf{p}_\perp^2}\right), \quad (\text{E.5})$$

where the overall factor of two stems from the degeneracy of the two Hamiltonians $H_{GN}(M)$ and $H_{GN}(M^*)$ in \mathcal{H}'_{1D} (see Eq. (3.23)). If we now use the symmetry property of the eigenvalue spectrum $\rho_{1D}(\lambda) = \rho_{1D}(-\lambda)$ and define $\tilde{f}(x) = f(x) + f(-x)$, we can obtain

$$\begin{aligned} \tilde{\Omega} &= \int_{-\infty}^{\infty} d\lambda \int \frac{d^2 \mathbf{p}_\perp}{(2\pi)^2} \rho_{1D}(\lambda) \tilde{f}\left(\sqrt{\lambda^2 + \mathbf{p}_\perp^2}\right) \\ &= \frac{1}{2\pi} \int_0^{\infty} dE E^2 \int_{-1}^1 du \rho_{1D}(Eu) \tilde{f}(E) \\ &= \int_0^{\infty} dE \rho(E) \tilde{f}(E), \end{aligned} \quad (\text{E.6})$$

where we introduced the energies E for the 3+1-dimensional system and defined the effective density of states

$$\rho(E) = \frac{1}{2\pi} \int_{-1}^1 du E^2 \rho_{1D}(Eu). \quad (\text{E.7})$$

After plugging the one-dimensional density of states Eq. (E.3) in Eq. (E.7) and performing the integration, carefully considering the different bands, we arrive at the explicit expression

$$\begin{aligned} \rho(E) = \frac{E\Delta}{\pi^2} \left\{ \right. & \theta(\sqrt{\tilde{\nu}}\Delta - E) \left[\mathbf{E}(\tilde{\theta}|\tilde{\nu}) + \left(\frac{\mathbf{E}(\nu)}{\mathbf{K}(\nu)} - 1 \right) \mathbf{F}(\tilde{\theta}|\tilde{\nu}) \right] \\ & + \theta(E - \sqrt{\tilde{\nu}}\Delta) \theta(\Delta - E) \left[\mathbf{E}(\tilde{\nu}) + \left(\frac{\mathbf{E}(\nu)}{\mathbf{K}(\nu)} - 1 \right) \mathbf{K}(\tilde{\nu}) \right] \\ & \left. + \theta(E - \Delta) \left[\mathbf{E}(\theta|\tilde{\nu}) + \left(\frac{\mathbf{E}(\nu)}{\mathbf{K}(\nu)} - 1 \right) \mathbf{F}(\theta|\tilde{\nu}) + \frac{\sqrt{(E^2 - \Delta^2)(E^2 - \tilde{\nu}\Delta^2)}}{E\Delta} \right] \right\}, \end{aligned} \quad (\text{E.8})$$

where \mathbf{K} and \mathbf{F} are the complete and incomplete elliptic integrals of 1st kind, respectively, \mathbf{E} are the (complete or incomplete) elliptic integrals of 2nd kind, and we introduced the notations $\tilde{\nu} = 1 - \nu$, $\tilde{\theta} = \arcsin(E/(\sqrt{\tilde{\nu}}\Delta))$, and $\theta = \arcsin(\Delta/E)$.

As an cross-check we can consider the limits $\nu \rightarrow 1$ and $\nu \rightarrow 0$, which should correpond to the inhomogeneous broken and restored solutions, respectively.

For $\nu = 1$ ($\tilde{\nu} = 0$), only the second and third terms in Eq. (E.8) contribute (since the first step functions reduces to $\theta(0 - E)$, and we are considering positive energies only). Furthermore, we note that

$$\mathbf{E}(x|0) = \mathbf{F}(x|0), \quad \mathbf{K}(0) = \mathbf{E}(0), \quad \mathbf{E}(1) = 1, \quad \mathbf{E}(1)/\mathbf{K}(1) = 0, \quad (\text{E.9})$$

so that the second contribution becomes identically zero, and we are left with only the last part of the third term, which reduces to

$$\rho(E)|_{\nu=1} = \frac{1}{\pi^2} \theta(E - \Delta) \sqrt{(E^2 - \Delta^2)} E, \quad (\text{E.10})$$

which is the effective density of states in an homogeneous phase with a quasiparticle gap Δ .

For the case $\nu = 0$, both the first and third term contribute. We make use of the property

$$\mathbf{E}(\arcsin(x)|1) = x, \quad (\text{E.11})$$

and see that both terms are equal, so the step functions add up to 1 and we are left with

$$\rho(E)|_{\nu=0} = \frac{1}{\pi^2} E^2, \quad (\text{E.12})$$

which corresponds to the density of states for a massless ultra-relativistic gas.

F. Spatially dependent density

In this section we present more details on the derivation of the expression for the spatial density of the system employed in Sec. 4.2.

Our starting point is the thermodynamic potential of the system, introduced in Chapter 2. Neglecting the condensate terms which are irrelevant for the density, it is given by

$$\Omega = -\frac{T}{V} \log \int D\bar{\psi} D\psi \exp \left(\int d^4x \bar{\psi} \mathcal{S}^{-1} \psi \right) \quad (\text{F.1})$$

$$= -\frac{T}{V} \log \det \frac{\mathcal{S}^{-1}}{T} = -\frac{T}{V} \text{Tr} \log \frac{\mathcal{S}^{-1}}{T}. \quad (\text{F.2})$$

We now introduce an operator $A = \gamma^0 \mathcal{S}^{-1}$ whose eigensystem in momentum space¹ is defined by

$$A\psi_k = \lambda_{n,k} \psi_k = (i\omega_n - E_k) \psi_k, \quad (\text{F.3})$$

where E_k are the eigenvalues of the Hamiltonian operator \mathcal{H} (Eq. (2.13)).

If we now include a finite chemical potential μ , we obtain (neglecting from now on color, flavor and spin factors for brevity)

$$\Omega = -T \sum_{n,k} \log \lambda_{n,k} = -T \sum_{n,k} \log(i\omega_n + \mu - E_k) = -T \sum_k \log \left[2 \cosh \left(\frac{E_k - \mu}{2T} \right) \right]. \quad (\text{F.4})$$

The particle density is given by

$$n = -\frac{\partial \Omega}{\partial \mu} = T \sum_k \frac{\partial}{\partial \mu} \log \left[2 \cosh \left(\frac{E_k - \mu}{2T} \right) \right] \quad (\text{F.5})$$

$$= -\frac{1}{2} \sum_k \tanh \left(\frac{E_k - \mu}{2T} \right) \quad (\text{F.6})$$

which, when exploiting the symmetry of the eigenvalue spectrum around $E = 0$, reduces to the familiar

$$n = -\frac{1}{2} \sum_{E>0} \left[\tanh \left(\frac{E - \mu}{2T} \right) + \tanh \left(\frac{-E - \mu}{2T} \right) \right] = \sum_{E>0} (n_q - \bar{n}_q), \quad (\text{F.7})$$

¹in euclidean space, a basis is given by the spatial momenta \mathbf{k} and the discrete Matsubara frequencies ω_n

with the usual occupation numbers n_q .

If we wish now to obtain an expression for the spatially-dependent particle density, we can take a step back and perform a change of basis to coordinate space. For this, let us consider a generic expression for an observable O of the type (it is always implied that we are talking about thermal expectation values)

$$O = \sum_{basis} f(E_{basis}), \quad (\text{F.8})$$

recalling that for the case of the density, $f(E) \propto \tanh((E - \mu)/2T)$. In a momentum basis, if we perform the Matsubara sum as before, it will be

$$O = \int d^3k f(E_{\mathbf{k}}) = \int d^3k O(\mathbf{k}). \quad (\text{F.9})$$

In coordinate space, if we assume for simplicity that the Matsubara sum has already been performed here as well (that is, we are working in a mixed representation where only the time component has been Fourier-transformed), the expression will look like

$$O = \int d^3x f(E_{\mathbf{x}}) = \int d^3x O(\mathbf{x}). \quad (\text{F.10})$$

As mentioned before, in order to get from one expression to the other it is possible to insert a complete basis,

$$O(\mathbf{x}) = \langle \mathbf{x} | O | \mathbf{x} \rangle = \sum_{k,k'} \langle \mathbf{x} | \mathbf{k}' \rangle \langle \mathbf{k}' | O | \mathbf{k} \rangle \langle \mathbf{k} | \mathbf{x} \rangle. \quad (\text{F.11})$$

If we consider in particular the solitonic modulations of the order parameter considered in chapter 4, eigenfunctions will be labeled by one-dimensional energies λ , so that the change to that basis leads to

$$O(\mathbf{x}) = \int d^2p_{\perp} \sum_{\lambda, \lambda'} \langle \mathbf{x} | \lambda' \rangle \langle \lambda' | O | \lambda \rangle \langle \lambda | \mathbf{x} \rangle = \int d^2p_{\perp} \sum_{\lambda} \psi_{\lambda}^{\dagger}(z) \psi_{\lambda}(z) O(\lambda), \quad (\text{F.12})$$

and we known from Ref. [45] that

$$\psi_{\lambda}^{\dagger}(z) \psi_{\lambda}(z) = \frac{(\lambda/\Delta)^2 + \frac{1}{2}((M(z)/\Delta)^2 + \nu - 2)}{(\lambda/\Delta)^2 - \mathbf{E}(\nu)/\mathbf{K}(\nu)}. \quad (\text{F.13})$$

Putting now everything together and including back the appropriate factors, for the spatially modulated density we obtain

$$n(z) = N_f N_c \int d\lambda \rho_{1D}(\lambda) \int \frac{dp_{\perp}}{(2\pi)^d} \psi_{\lambda}^{\dagger}(z) \psi_{\lambda}(z) (n_+(E) - n_-(E)), \quad (\text{F.14})$$

where $\rho_{1D}(\lambda)$ is the spectral density of the one-dimensional GN model². Similar to the determination of the effective density of states performed in Appendix E.1, it is then a tedious but straightforward exercise to cast the expression for the density profile into the form

$$n_{\text{soliton}}(z) = N_f N_c \int_0^\infty dE \rho_{D,\text{soliton}}(E, z) (n_+(E) - n_-(E)) , \quad (\text{F.15})$$

where the density matrix element $\rho_{D,\text{soliton}}(E, z)$ can be related to $\rho_{\text{soliton}}(E)$, Eq. (3.26), upon the replacement

$$\rho_{D,\text{soliton}}(E, z) = \rho_{\text{soliton}}(E) \Big|_{\frac{\mathbf{E}(\nu)}{\mathbf{K}(\nu)} \rightarrow -\frac{1}{2} \left(\left(\frac{M(z)}{\Delta} \right)^2 + \nu - 2 \right)} . \quad (\text{F.16})$$

²The combination $\psi_\lambda^\dagger(z)\psi_\lambda(z)$ is a boost-invariant quantity.

G. Ginzburg-Landau expansion for vector interactions

This appendix is devoted to the discussion of a Ginzburg-Landau analysis on the effects of vector interactions on the position of the chiral critical point (CP) and the Lifshitz point (LP). In the vicinity of a second-order phase transition and in particular of a critical point, the thermodynamic potential can be expanded as an effective action in $\delta M(\mathbf{x}) = M(\mathbf{x}) - M_0$ and $\delta\tilde{\mu}(\mathbf{x}) = \tilde{\mu}(\mathbf{x}) - \tilde{\mu}_0$ around their values $M(\mathbf{x}) = M_0$ and $\delta\tilde{\mu}(\mathbf{x}) = \tilde{\mu}_0$ in the restored phase. For simplicity, we restrict ourselves to the chiral limit, so that $M_0 = 0$ and therefore $\delta M(\mathbf{x}) = M(\mathbf{x})$. However, unlike in the numerical studies performed in Sec. 5.1.2, we will not assume $\tilde{\mu}(\mathbf{x})$ to be spatially uniform.

At given temperature and chemical potential the expansion then takes the form

$$\Omega[M, \tilde{\mu}] = \Omega[0, \tilde{\mu}_0] + \frac{1}{V} \int d\mathbf{x} \Omega_{GL}(M(\mathbf{x}), \delta\tilde{\mu}(\mathbf{x})), \quad (\text{G.1})$$

with

$$\begin{aligned} \Omega_{GL}(M(\mathbf{x}), \delta\tilde{\mu}(\mathbf{x})) &= c_{2,a}|M(\mathbf{x})|^2 + c_{2,b}\delta\tilde{\mu}(\mathbf{x})^2 + c_{3,a}|M(\mathbf{x})|^2\delta\tilde{\mu}(\mathbf{x}) + c_{3,b}\delta\tilde{\mu}(\mathbf{x})^3 \\ &+ c_{4,a}|M(\mathbf{x})|^4 + c_{4,b}|\nabla M(\mathbf{x})|^2 + c_{4,c}|M(\mathbf{x})|^2\delta\tilde{\mu}(\mathbf{x})^2 + c_{4,d}\delta\tilde{\mu}(\mathbf{x})^4 + c_{4,e}(\nabla\delta\tilde{\mu}(\mathbf{x}))^2 + \dots, \end{aligned} \quad (\text{G.2})$$

when expanding to fourth order in $M(\mathbf{x})$, $\delta\tilde{\mu}(\mathbf{x})$ and gradients acting on these functions. The symmetries of the theory and of the background simplify the expansion: linear terms vanish as we are expanding around a homogeneous solution of the gap equations, odd terms in $M(\mathbf{x})$ vanish by chiral symmetry and odd numbers of derivatives vanish due to rotational symmetry.

Taking $M(\mathbf{x})$ to be the small scale of interest, we first aim at an estimate for $\delta\tilde{\mu}(\mathbf{x}; M(\mathbf{x}))$ defined through the stationary constraint

$$\left. \frac{\delta\Omega}{\delta\delta\tilde{\mu}} \right|_{M(\mathbf{x}), \delta\tilde{\mu}(\mathbf{x})=\delta\tilde{\mu}(\mathbf{x}; M(\mathbf{x}))} = 0. \quad (\text{G.3})$$

Because of the absence of a linear term in $M(\mathbf{x})$ we conclude that $\delta\tilde{\mu}(\mathbf{x}; M(\mathbf{x})) \sim O(|M(\mathbf{x})|^2)$. More precisely,

$$\delta\tilde{\mu}(\mathbf{x}; M(\mathbf{x})) = -\frac{c_{3,a}}{2c_{2,b}}|M(\mathbf{x})|^2 + \dots. \quad (\text{G.4})$$

Consequently, the expansion of $\Omega_{GL}(M(\mathbf{x})) \equiv \Omega_{GL}(M(\mathbf{x}), \delta\tilde{\mu}(\mathbf{x}; M(\mathbf{x})))$ to fourth order is given by

$$\begin{aligned}\Omega_{GL}(M(\mathbf{x})) &= \Omega_{GL}[0, \tilde{\mu}_0] + c_{2,a}|M(\mathbf{x})|^2 \\ &+ \left(c_{4,a} - \frac{c_{3,a}^2}{4c_{2,b}} \right) |M(\mathbf{x})|^4 + c_{4,b}|\nabla M(\mathbf{x})|^2 + \dots,\end{aligned}\quad (\text{G.5})$$

which allows us to determine the Lifshitz and the critical points from the GL coefficients. The latter is characterized by vanishing quadratic and quartic mass terms, while at the former the quadratic term and the gradient term are zero:

$$\begin{aligned}\text{LP: } 0 &= c_{2,a} = c_{4,b}, \\ \text{CP: } 0 &= c_{2,a} = c_{4,a} - \frac{c_{3,a}^2}{4c_{2,b}}.\end{aligned}\quad (\text{G.6})$$

As outlined in Ref. [89] for the NJL model without vector interactions, it is a straightforward exercise to work out the explicit form of the GL coefficients. As obvious from Eqs. (5.5) the kinetic part of the thermodynamic potential, Ω_{kin} , and, hence, its contributions to the GL coefficients depend on G_V only indirectly through $\tilde{\mu}_0$ and T . The only explicit dependence on G_V therefore originates from the condensate term Ω_{cond} and only affects $c_{2,b}$. For this reason the Lifshitz point as a function of $\tilde{\mu}_0$ and T is independent of G_V , in agreement with our findings in Sec. 5.1.2.

In contrast there is an explicit dependence of the location of the critical point on G_V through $c_{2,b}$. One finds

$$c_{2,b} = -\frac{1}{4G_V} - N_c \left(\frac{\tilde{\mu}_0^2}{\pi^2} + \frac{T^2}{3} \right), \quad (\text{G.7})$$

where the first term on the right hand side is due to Ω_{cond} , while the second term is due to Ω_{kin} . Since we are expanding around a homogeneous restored solution, the latter is just given by the corresponding term in an ideal Fermi gas at temperature T and chemical potential $\tilde{\mu}_0$. Here we have neglected the contributions from the regulator terms, which would arise in our specific model. However, these terms are small in the region of interest and therefore do not lead to qualitative changes. Hence, $1/c_{2,b}$ vanishes for $G_V = 0$ and decreases monotonously with increasing positive values of G_V . Furthermore $c_{4,a}$ typically decreases when increasing $\tilde{\mu}_0$ or decreasing T in the vicinity of the critical point. Put together, we conclude from Eq. (G.6) that the CP moves to smaller temperatures upon increasing G_V . Moreover, discarding possible issues related to the regularization of the UV-divergent vacuum contribution to the thermodynamic potential¹, we find $c_{4,a} = c_{4,b}$, as in the case without vector interaction. For $G_V = 0$ we therefore recover the result of Ref. [89] that the LP and the CP coincide.

Since $\delta\tilde{\mu}(\mathbf{x}) \sim O(M(\mathbf{x})^2)$ we can also conclude that the thermodynamic potential expanded around $\tilde{\mu}_0$ to order $O(|M(\mathbf{x})|^2)$ and arbitrary gradients coincides with that of the model

¹For a renormalizable theory divergent GL coefficients are subject to renormalization; the present discussion is consistent for a regularization scheme acting on the energy spectrum as applied in this work.

for $G_V = 0$ upon replacing $\mu \rightarrow \tilde{\mu}_0$. As a result, the second-order phase transition from any inhomogeneous to the chirally restored phase, being triggered by these contributions, is only depending on G_V through $\tilde{\mu}_0$, as it was already obtained in Sec. 5.1.2 after applying further truncations.

On the other hand, the present analysis is not applicable to the transition from the homogeneous broken to inhomogeneous phase, where the mass function is not related to a small parameter, when we go away from the LP. As we have argued earlier, even the order of the phase transition may change in this regime when vector interactions are included. Qualitatively the same properties as discussed here for the NJL model with a vector interaction also show up in the Gross-Neveu model with a Thirring interaction (GNT model) at leading order in the large N -expansion [71].

H. Lattice structures and symmetries

In this appendix we discuss some of the symmetry properties of lattice structures which allow us to perform our numerical analysis.

When considering spatial modulations for the chiral condensate, it is naturally possible to allow for different crystalline structures. Once having set the underlying lattice structure, the chiral condensate will be allowed to assume a spatial dependence compatible with the periodicity in the different directions. For one-dimensional structures, there is obviously no freedom to build an arbitrary structure and the only quantity defining the underlying lattice is the period in the z direction, whereas in two spatial dimensions different patterns are possible.

If we assume a periodic structure for the chiral condensate, the evaluation of the thermodynamic potential can be dramatically simplified by employing well established results from solid state physics. For this, we start from the generic definition of a Bravais lattice (BL) as the set of all points defined as a linear combination of the basis vectors $\{\mathbf{a}_i\}$ with integer coefficients $\{n_i\}$. The index i runs up to the number of spatial dimensions. For a three-dimensional lattice we therefore have

$$\mathbf{R} = n_1 \mathbf{a}_1 + n_2 \mathbf{a}_2 + n_3 \mathbf{a}_3, \quad n_i \in \mathbb{Z} \quad (\text{H.1})$$

A primitive cell can be defined as a cell containing a single lattice point that when translated covers the whole lattice without overlaps. A Wigner-Seitz (WS) cell is a primitive cell with the full lattice symmetry. It can be alternatively defined as the region of space that is closer to a single lattice point than to any other point.

Once having defined our lattice structure in coordinate space, we can introduce the concept of reciprocal lattice (RL), a lattice of momenta arising due to the crystal periodicity and the loss of translational symmetry in the system. If we consider a generic plane wave $e^{i\mathbf{kr}}$, we say that for it to have the lattice periodicity, its wave vector k must be in the reciprocal lattice. That is, for $\mathbf{R} \in BL$,

$$\mathbf{K} \in RL \quad \text{if} \quad e^{i\mathbf{K}(\mathbf{r}+\mathbf{R})} = e^{i\mathbf{K}\mathbf{r}} \longrightarrow e^{i\mathbf{K}\mathbf{R}} = 1 \quad \forall \mathbf{R} \in BL \quad (\text{H.2})$$

The RL is thus generated by a set of \mathbf{b}_i for which

$$\mathbf{b}_i \mathbf{a}_j = 2\pi\delta_{ij} \quad (\text{H.3})$$

A primitive cell of the RL has volume $(2\pi)^3/v_{cell}$, with v_{cell} being the volume of the WS cell. The Wigner-Seitz primitive cell of the RL is called first Brillouin zone. For an homogeneous chiral condensate, the Brillouin zone is infinite.

For periodic shapes of the chiral condensate, the only allowed wave vectors in the Fourier expansion of the spatial modulation will therefore lie in the RL. It is then clear from

Eq. (2.30) that when quarks scatter with the chiral condensate, they will only be able to exchange these determined momenta and the problem can therefore effectively be factorized. In particular, due to this periodicity, the Hamiltonian operator can be block-diagonalized, with each block characterized by a momentum of the BZ.

$$\mathcal{H} = \sum_{k \in BZ} \mathcal{H}(k), \quad (H.4)$$

and for each of these block, we know that scattering with the quark condensate will only couple momenta differing by a RL element. This in turn allows to map momenta in the matrix $\mathcal{H}(k)$ in a grid structure, where each element is separated from the others by a RL vector, and the momentum integration can be effectively factorized in an integral over the Brillouin zone and a sum over the eigenvalues $\{\lambda_k\}$ of the grid-structured $\mathcal{H}(k)$.

H.1. Two-dimensional lattice structures

In this section we briefly outline the procedure followed to build the two-dimensional crystalline structures considered in our analysis.

We start from a generic unit cell spanned by the vectors \mathbf{a}_1 and \mathbf{a}_2 . A periodic modulation on this lattice will fulfill

$$M(\mathbf{x}) = M(\mathbf{x} + n\mathbf{a}_1 + m\mathbf{a}_2). \quad (H.5)$$

This in turn allows for a Fourier expansion of the order parameter,

$$M(\mathbf{x}) = \sum_{m,n} M_{mn} e^{i\mathbf{q}_{mn} \cdot \mathbf{x}}, \quad (H.6)$$

with the reciprocal lattice for the momenta defined by

$$\mathbf{q}_{mn} \cdot \mathbf{a}_1 = 2\pi m, \quad \mathbf{q}_{mn} \cdot \mathbf{a}_2 = 2\pi n. \quad (H.7)$$

Explicitly, in cartesian coordinates this becomes

$$\begin{pmatrix} q_{mn}^x \\ q_{mn}^y \end{pmatrix} = \frac{2\pi}{a_{1x}a_{2y} - a_{1y}a_{2x}} \begin{pmatrix} ma_{2y} - na_{1y} \\ na_{1x} - ma_{2x} \end{pmatrix}. \quad (H.8)$$

A generic parametrization on the (x, y) plane for the lattice basis vectors can be given by

$$\mathbf{a}_1 = \begin{pmatrix} a \\ 0 \end{pmatrix}, \quad \mathbf{a}_2 = \begin{pmatrix} b \cos \varphi \\ b \sin \varphi \end{pmatrix}, \quad (H.9)$$

from which the definition of the RL vectors in cartesian coordinates follows:

$$\mathbf{q}_{mn} = \frac{2\pi}{ab \sin \varphi} \begin{pmatrix} mb \sin \varphi \\ na - mb \cos \varphi \end{pmatrix}. \quad (H.10)$$

For the first vectors of the RL which define the Brillouin zone one has

$$\mathbf{q}_{00} = \begin{pmatrix} 0 \\ 0 \end{pmatrix}, \quad \mathbf{q}_{10} = \frac{2\pi}{a b \sin \varphi} \begin{pmatrix} b \sin \varphi \\ -b \cos \varphi \end{pmatrix}, \quad \mathbf{q}_{01} = \frac{2\pi}{b \sin \varphi} \begin{pmatrix} 0 \\ 1 \end{pmatrix}. \quad (\text{H.11})$$

For the simplest case, namely a square lattice, we choose the angle between the two lattice basis vectors (Eq. (H.9)) to be $\varphi = \frac{\pi}{2}$, and their lengths to be the same: $a = b$. The two basis vectors are therefore

$$\mathbf{a}_1 = \begin{pmatrix} a \\ 0 \end{pmatrix}, \quad \mathbf{a}_2 = \begin{pmatrix} 0 \\ a \end{pmatrix}, \quad (\text{H.12})$$

and the Brillouin zone is given by

$$\mathbf{q}_{00} = \begin{pmatrix} 0 \\ 0 \end{pmatrix}, \quad \mathbf{q}_{10} = \frac{2\pi}{a} \begin{pmatrix} 1 \\ 0 \end{pmatrix}, \quad \mathbf{q}_{01} = \frac{2\pi}{a} \begin{pmatrix} 0 \\ 1 \end{pmatrix}. \quad (\text{H.13})$$

For brevity we introduce $Q \equiv \frac{2\pi}{a}$. The Fourier expansion for $M(\mathbf{x})$ in this particular lattice is

$$M(\mathbf{x}) = \sum_{m,n} M_{mn} e^{i\mathbf{q} \cdot \mathbf{x}} = \sum_{m,n} M_{mn} e^{imQx} e^{inQy}. \quad (\text{H.14})$$

A simple real ansatz on top of this lattice can be built by limiting the sum to

$$\begin{pmatrix} m \\ n \end{pmatrix} = \left\{ \begin{pmatrix} 1 \\ 1 \end{pmatrix}, \begin{pmatrix} 1 \\ -1 \end{pmatrix}, \begin{pmatrix} -1 \\ 1 \end{pmatrix}, \begin{pmatrix} -1 \\ -1 \end{pmatrix} \right\}, \quad (\text{H.15})$$

and by choosing the same amplitude for all of these modes, $M_{mn} \equiv \Delta$, one obtains

$$\begin{aligned} M(\mathbf{x}) &= \Delta [e^{iQx} e^{iQy} + e^{iQx} e^{-iQy} + e^{-iQx} e^{iQy} + e^{-iQx} e^{-iQy}] \\ &= 4\Delta [\cos(Qy) \cos(Qx)]. \end{aligned} \quad (\text{H.16})$$

An alternative choice would be

$$\begin{pmatrix} m \\ n \end{pmatrix} = \left\{ \begin{pmatrix} 1 \\ 0 \end{pmatrix}, \begin{pmatrix} -1 \\ 0 \end{pmatrix}, \begin{pmatrix} 0 \\ 1 \end{pmatrix}, \begin{pmatrix} 0 \\ -1 \end{pmatrix} \right\}, \quad (\text{H.17})$$

again with the same amplitude Δ for all modes, leading to $M(x, y) = 2\Delta(\cos(Qx) + \cos(Qy))$. This is however equivalent to the previous ansatz in a frame rotated by $\pi/4$ and with Q replaced by $Q/\sqrt{2}$.

To calculate useful quantities like $\langle M(x, y)^2 \rangle$ one has to perform integrals over the Wigner-Seitz (WS) cell of the lattice defined by the vectors \mathbf{a} and \mathbf{b} , where the volume of this cell is simply given by

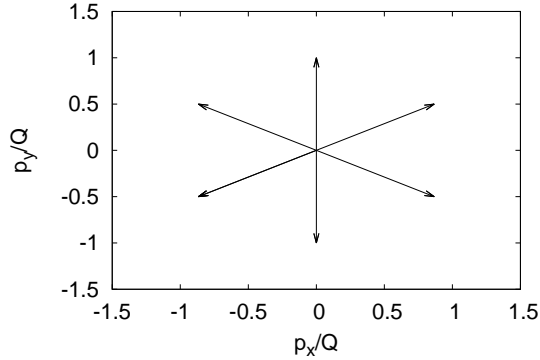


Figure H.1.: Momenta in the RL for the hexagonal symmetry solution (Eq. (H.23)).

$$V_{WS} = \int_0^a dy \int_0^a dx = a^2 = \left(\frac{2\pi}{Q}\right)^2 \quad (\text{H.18})$$

Let us now consider a different lattice structure. by choosing the angle between the two basis vectors to be $\varphi = \frac{\pi}{3}$ and their lengths to be the same ($a = b$), we obtain a triangular lattice. The two basis vectors are then

$$\mathbf{a}_1 = \begin{pmatrix} a \\ 0 \end{pmatrix}, \quad \mathbf{a}_2 = \begin{pmatrix} a/2 \\ a\sqrt{3}/2 \end{pmatrix}, \quad (\text{H.19})$$

and the Brillouin zone is given by

$$\mathbf{q}_{00} = \begin{pmatrix} 0 \\ 0 \end{pmatrix}, \quad \mathbf{q}_{10} = \frac{4\pi}{a\sqrt{3}} \begin{pmatrix} \sqrt{3}/2 \\ -1/2 \end{pmatrix}, \quad \mathbf{q}_{01} = \frac{4\pi}{a\sqrt{3}} \begin{pmatrix} 0 \\ 1 \end{pmatrix}. \quad (\text{H.20})$$

Here we define for brevity $Q = \frac{4\pi}{a\sqrt{3}}$.

Now $M(\mathbf{x})$ can be expanded as a Fourier series in this particular lattice as

$$M(\mathbf{x}) = \sum_{m,n} M_{mn} e^{i\mathbf{Q} \cdot \mathbf{x}} = \sum_{m,n} M_{mn} e^{i\frac{\sqrt{3}}{2}mQx} e^{i(n-\frac{m}{2})Qy}. \quad (\text{H.21})$$

One can pick a simple ansatz with some symmetry by limiting the sum to (Fig. H.1)

$$\begin{pmatrix} m \\ n \end{pmatrix} = \left\{ \begin{pmatrix} 1 \\ 0 \end{pmatrix}, \begin{pmatrix} -1 \\ 0 \end{pmatrix}, \begin{pmatrix} 0 \\ 1 \end{pmatrix}, \begin{pmatrix} 0 \\ -1 \end{pmatrix}, \begin{pmatrix} 1 \\ 1 \end{pmatrix}, \begin{pmatrix} -1 \\ -1 \end{pmatrix} \right\}, \quad (\text{H.22})$$

and by choosing the same amplitude $M_{mn} \equiv \Delta$ for all of these modes, we obtain

$$\begin{aligned}
M(\mathbf{x}) &= \Delta \left[e^{iQy} + e^{iQ\sqrt{3}/2x} e^{-i/2Qy} + e^{-iQy} + e^{-iQ\sqrt{3}/2x} e^{i/2Qy} + e^{iQ\sqrt{3}/2x} e^{i/2Qy} + e^{-iQ\sqrt{3}/2x} e^{-i/2Qy} \right] \\
&= 2\Delta \left[\cos(Qy) + 2 \cos\left(\frac{\sqrt{3}}{2}Qx\right) \cos\left(\frac{1}{2}Qy\right) \right]. \tag{H.23}
\end{aligned}$$

Another possible ansatz that can be built on top of this triangular lattice is given by the sum over the harmonics

$$\begin{pmatrix} m \\ n \end{pmatrix} = \left\{ \begin{pmatrix} 0 \\ -1 \end{pmatrix}, \begin{pmatrix} -1 \\ 0 \end{pmatrix}, \begin{pmatrix} 1 \\ 1 \end{pmatrix} \right\}, \tag{H.24}$$

leading to

$$M(x, y) = \Delta \left[e^{-iQy} + 2e^{\frac{i}{2}Qy} \cos\left(\frac{\sqrt{3}}{2}Qx\right) \right]. \tag{H.25}$$

Due to the lower symmetry of this complex modulation, its numerical treatment is however more involved. Since it appears that real modulations are usually energetically favored over complex ones, we choose to postpone the study of this last ansatz to future work and focus our efforts on the study of real modulations.

For this lattice, the volume of the WS cell is given by

$$V_{WS} = \int_0^{a\frac{\sqrt{3}}{2}} dy \int_{\frac{y}{\sqrt{3}}}^{a+\frac{y}{\sqrt{3}}} dx = \frac{8\pi^2}{\sqrt{3}Q^2} = a^2 \frac{\sqrt{3}}{2}. \tag{H.26}$$

I. Numerical diagonalization of the Hamiltonian

With the notable exceptions of the chiral density wave and the solitonic solutions, there are no analytical expressions for the eigenvalue spectrum of the mean-field Hamiltonian \mathcal{H} (Eq. (2.13)) in Dirac and momentum space for an inhomogeneous order parameter. In order to calculate the thermodynamic potential associated with a given crystalline shape, a numerical diagonalization of the model Hamiltonian has therefore to be performed. As a template describing the basics of our numerical implementation, we discuss here the simple case of the one-dimensional real sinusoidal modulation introduced in Sec. 3.3.2:

$$M(z) = 2M_1 \cos(Qz). \quad (\text{I.1})$$

After plugging this kind of modulation in the mean-field Hamiltonian Eq. (2.30), we obtain the following structure in Dirac and momentum space:

$$\mathcal{H}_{p_n, p_m}^{\cos} = \gamma^0 [\boldsymbol{\gamma} \cdot \mathbf{p}_n \delta_{p_n, p_m} + M_1 \delta_{p_n, p_m + Q} + M_1 \delta_{p_n, p_m - Q}]. \quad (\text{I.2})$$

For our numerical implementation we exploit the lattice symmetries described in Appendix H and build a set of Hamiltonians, one for each momentum k of the Brillouin zone. The elements of these Hamiltonians $\mathcal{H}(k)$ will be 4 by 4 Dirac blocks, each one characterized by momenta separated by reciprocal lattice elements. In the case of the one-dimensional cosine, momentum elements will be given by $p_z = k + nQ$, with n integer and Q wave vector of the modulation. Since only the ± 1 harmonics are involved, only the first off-diagonal elements are filled, so that the matrix has a banded structure.

Even after identifying this block structure, the $\mathcal{H}(k)$ are still infinite matrices, as the index n can run from $-\infty$ to ∞ . We therefore implement a numerical cutoff Λ_P on the maximum allowed momentum. In practice we write each $\mathcal{H}(k)$ as

$$\mathcal{H}(k) = \begin{pmatrix} \square_D(k - NQ) & \square_O & & & \dots & & & \\ \square_O & \square_D(k - (N-1)Q) & \square_O & \square_O & & & & \\ & \square_O & \square_D(k - (N-2)Q) & & & & & \\ & & & \dots & & & & \\ & & & & \dots & & & \\ & & & & & \square_O & \square_D(k + NQ) & \\ & & & & & & & (\text{I.3}) \end{pmatrix},$$

where N is the cutoff-dependent integer that determines how big the matrix is, *i. e.* basically how many times the modulation wave vector (and thus the BZ size) is contained in the momentum cutoff Λ_P :

$$N = (\text{nearest integer}) \frac{\Lambda_P}{Q}. \quad (\text{I.4})$$

Within this setup, smaller BZ sizes will therefore result in larger matrices. In practice, the numerical diagonalization becomes no longer feasible for modulations with small (below ≈ 100 MeV) wave vectors. This is not expected to be a dramatic limitation anyway, since we expect the typical values for Q to be of order $\mu \approx 300$ MeV in our inhomogeneous window.

For the one-dimensional cosine, the diagonal blocks are given by

$$\square_D(p_z) = \gamma^0 \boldsymbol{\gamma} \cdot \mathbf{p} = \gamma^0 \gamma^3 p_z = \begin{pmatrix} -p_z & 0 & 0 & 0 \\ 0 & p_z & 0 & 0 \\ 0 & 0 & p_z & 0 \\ 0 & 0 & 0 & -p_z \end{pmatrix}, \quad (\text{I.5})$$

while the off-diagonal ones are

$$\square_O = \gamma^0 M_1 = \begin{pmatrix} 0 & 0 & M_1 & 0 \\ 0 & 0 & 0 & M_1 \\ M_1 & 0 & 0 & 0 \\ 0 & M_1 & 0 & 0 \end{pmatrix}. \quad (\text{I.6})$$

The condensate part Ω_{cond} can be readily evaluated, giving

$$\Omega_{\text{cond}}^{\text{cos}} = \frac{1}{4G_S L} \int_0^L dz M(z)^2 = \frac{M_1^2}{2G_S}, \quad (\text{I.7})$$

where $L = 2\pi/Q$ is the period of the modulation.

I.1. Cutoff and asymptotic density of states

Since our matrices are cut in momentum space, one might expect cutoff effects at the edges. In order to reduce these, we also cut the integration over the (boosted) eigenvalues at a certain value $\Lambda_E < \Lambda_P$ ¹. Beyond that, we use an asymptotic expression for the density of states.

We know that asymptotically the density of states is, for a one-dimensional real order parameter² [90]:

$$\rho_A(E) = \frac{E^2}{\pi^2} - \frac{\langle M(z)^2 \rangle}{2\pi^2} - \frac{\langle M(z)^4 \rangle + \langle M'(z)^2 \rangle}{8\pi^2 E^2} + O(E^{-4}) \quad (\text{I.8})$$

¹Although Λ_E has been varied to test the numerical stability of the results, a typical value for it is $\Lambda_E \approx \Lambda_P - 2M_{\text{vac}}$.

²This expression can be obtained by expanding $\rho(E, \langle M(\mathbf{x}) \rangle)$ in powers of $1/E$, which (for dimensional arguments) can lead only to specific terms depending on powers of $\langle M(\mathbf{x}) \rangle$ and its gradients. The prefactors can then be obtained by matching the expression with a GL expansion of the thermodynamic potential.

The generalization of Eq. (I.8) for a two-dimensional modulation can be obtained by requiring a rotationally invariant expression which reduces to Eq. (I.8) for the one-dimensional case. This consists in substituting

$$\langle M(z)^2 \rangle \longrightarrow \langle M(x, y)^2 \rangle = \frac{1}{V_{xy}} \int_{V_{xy}} dx dy M(x, y)^2, \quad (\text{I.9})$$

$$\langle M(z)^4 \rangle \longrightarrow \langle M(x, y)^4 \rangle = \frac{1}{V_{xy}} \int_{V_{xy}} dx dy M(x, y)^4, \quad (\text{I.10})$$

$$\langle M'(z)^2 \rangle \longrightarrow \langle \nabla M(x, y)^2 \rangle = \frac{1}{V_{xy}} \int_{V_{xy}} dx dy \left(\frac{\partial M}{\partial x}, \frac{\partial M}{\partial y} \right) \cdot \left(\frac{\partial M}{\partial x}, \frac{\partial M}{\partial y} \right). \quad (\text{I.11})$$

We get therefore

$$\rho_A^{2D}(E) = \frac{E^2}{\pi^2} - \frac{\langle M(x, y)^2 \rangle}{2\pi^2} - \frac{\langle M(x, y)^4 \rangle + \langle (\nabla M(x, y))^2 \rangle}{8\pi^2 E^2} + O(E^{-4}). \quad (\text{I.12})$$

With this asymptotic contribution the thermodynamic potential is then

$$\Omega_{kin}(T, \mu; M(\mathbf{x})) = \Omega_{kin}^{\Lambda_E} - N_f N_c \int_{\Lambda_E}^{\infty} dE \rho_A(E) \{ f_{UV}^{PV}(E) + f_{med}(E) \}, \quad (\text{I.13})$$

where in $\Omega_{kin}^{\Lambda_E}$ the eigenvalue sum is performed up to a numerical cutoff Λ_E , that is,

$$\Omega_{\Lambda_E} = -\frac{4N_f N_c}{(2\pi)^3} \int_{BZ} dk_x dk_y \int_0^{\infty} dp_{\perp} \sum_{\lambda > 0} \{ [f_{UV}^{PV}(E_{\perp}) + f_{med}(E_{\perp})] \theta(\Lambda_E - |E_{\perp}|) \}, \quad (\text{I.14})$$

with $\lambda(\mathbf{k})$ eigenvalues of the 2D Hamiltonian and $E_{\perp} = \sqrt{\lambda(\mathbf{k})^2 + p_{\perp}^2}$ boosted energies.

I.2. Analytical expressions for the chiral density wave modulation

If the spatial dependence of the chiral condensate is described by a plane wave modulation (CDW), an analytical expression for the eigenvalue spectrum of the mean-field Hamiltonian can be derived. While a detailed derivation is already reported in [54, 49], in this section we just want to point out how the same analytical expression can be derived by looking at the shape of the Hamiltonian in Dirac and momentum space and recognizing a block-diagonal structure.

Explicitly, in our Fourier expansion of the order parameter Eq. (2.28), we keep only the first component:

$$M(z) = M_1 e^{iQz}, \quad (\text{I.15})$$

where the wave vector Q of the modulation determines the size of the first Brillouin zone for our chiral crystal. Some authors prefer to insert a factor of 2 in the definition of the wave vector, for reasons that will become apparent in the following. For our purposes, it is better to work with the equivalent expression $M(z) = M_1 e^{-iQz}$.

In Dirac and momentum space, the mean-field Hamiltonian for this kind of modulation will look like

$$\mathcal{H} = \begin{pmatrix} \dots & & & & & \\ & \begin{bmatrix} -p_i & 0 & 0 & 0 \\ 0 & p_i & 0 & 0 \\ 0 & 0 & p_i & 0 \\ 0 & 0 & 0 & -p_i \\ 0 & 0 & M_1 & 0 \\ 0 & 0 & 0 & M_1 \\ 0 & 0 & 0 & 0 \\ 0 & 0 & 0 & 0 \end{bmatrix} & \begin{bmatrix} 0 & 0 & 0 & 0 \\ 0 & 0 & 0 & 0 \\ M_1 & 0 & 0 & 0 \\ 0 & M_1 & 0 & 0 \\ -p_{i+1} & 0 & 0 & 0 \\ 0 & p_{i+1} & 0 & 0 \\ 0 & 0 & p_{i+1} & 0 \\ 0 & 0 & 0 & -p_{i+1} \end{bmatrix} & \begin{bmatrix} 0 & 0 & 0 & 0 \\ 0 & 0 & 0 & 0 \\ 0 & 0 & 0 & 0 \\ 0 & 0 & 0 & 0 \\ 0 & 0 & 0 & 0 \\ 0 & 0 & 0 & 0 \\ M_1 & 0 & 0 & 0 \\ 0 & M_1 & 0 & 0 \end{bmatrix} & \dots \\ & & & & & \dots \end{pmatrix}$$

with the momenta in the various blocks defined as $p_i = k + iQ$, $k \in BZ$, $i \in \mathcal{N}$.

At this point we can notice that the matrix is block-diagonal, (aside from the first two and the last two entries, which are immediately diagonal due to the numerical cutoff implemented) and the blocks on the diagonal (which have been highlighted in red) are given by

$$\square_{Diag} = \begin{bmatrix} p_i & 0 & M_1 & 0 \\ 0 & -p_i & 0 & M_1 \\ M_1 & 0 & -p_{i+1} & 0 \\ 0 & M_1 & 0 & p_{i+1} \end{bmatrix}, \quad (I.16)$$

and the eigenvalues of a given block m are given by

$$\lambda_m = \pm \left(\sqrt{\tilde{p}_m^2 + M_1^2} \pm \tilde{Q} \right), \quad (\text{I.17})$$

where we introduced $\tilde{Q} = Q/2$ and $\tilde{p}_m = k + m\tilde{Q}$.

The expression for the thermodynamic potential is

$$\Omega(T, \mu; Q, M(z)) \propto \int_0^Q dk \int_0^\infty dp_\perp p_\perp \sum_{\lambda_\perp} f(E_\perp), \quad (\text{I.18})$$

where $E_\perp = \sqrt{\lambda_k^2 + p_\perp^2}$ and $f(x)$ is the usual integrand. Focusing on the one-dimensional eigenvalues (the problem can be subsequently boosted along the two transverse directions,

as described in Sec. 3.2.1), in principle one would have to sum over the infinite grid of momenta,

$$\int_0^{\tilde{Q}} dk \sum_{\lambda_k} f(\lambda_k) = \int_0^{\tilde{Q}} dk \sum_{m=-\infty}^{\infty} f(\lambda_m), \quad (I.19)$$

where the $\{\lambda_m\}$ are the eigenvalues of the single blocks. At this point one can see that the combined sum and integral over the BZ are simply a way to rewrite the integral over the full p_z range (we will relabel $p_z = p$ in the following). We can thus write

$$\int_0^{\tilde{Q}} dk \sum_{\lambda} f(\lambda) = \int dp \sum_{Dirac} f(\lambda). \quad (I.20)$$

We now plug in the expression found for the one-dimensional eigenvalues,

$\lambda(p) = \pm \left(\sqrt{p^2 + M_1^2} \pm \tilde{Q} \right)$ and convert the integration variable from momentum to energy. For this, consider as an example the case $\lambda = \sqrt{p^2 + M_1^2} + \tilde{Q}$, from which $\lambda - \tilde{Q} = \sqrt{p^2 + M_1^2} > 0$. One can then rewrite

$$\begin{aligned} \lambda^2 &= p^2 + M_1^2 + \tilde{Q}^2 + 2\tilde{Q}\sqrt{p^2 + M_1^2} = p^2 + M_1^2 + \tilde{Q}^2 + 2\tilde{Q}(\lambda - \tilde{Q}), \\ p^2 &= (\lambda - \tilde{Q})^2 - M_1^2, \end{aligned} \quad (I.21)$$

from which

$$d\lambda = \frac{dp p}{\sqrt{p^2 + M_1^2}} = \frac{\sqrt{(\lambda - \tilde{Q})^2 - M_1^2}}{\lambda - \tilde{Q}} dp. \quad (I.22)$$

Starting from this, we would like to recover the result from [49] for the density of states of the one-dimensional chiral density wave (or chiral spiral). The chiral spiral has a spectrum with a single band, its density of states being

$$\rho_{sp}^{1D}(\lambda) = \frac{1}{\pi} \frac{|\lambda - \tilde{Q}|}{\sqrt{(\lambda - \tilde{Q})^2 - M_1^2}}. \quad (I.23)$$

After inverting Eq. (I.22) and plugging the result in Eq. (I.20), we can rewrite the equation as $\int d\lambda \rho(\lambda) f(\lambda)$, and by comparing the two expressions we see that we recover one part of the density of states. The same procedure can be applied for the other eigenvalues, leading to the full expression Eq. (I.23).

Bibliography

- [1] CERN, press release on Higgs search, 4 July 2012.
- [2] D. J. Gross and F. Wilczek, *Phys.Rev.Lett.* **30**, 1343–1346 (1973).
- [3] H. D. Politzer, *Phys.Rev.Lett.* **30**, 1346–1349 (1973).
- [4] M. A. Stephanov, *Prog. Theor. Phys. Suppl.* **153**, 139 (2004).
- [5] D. H. Rischke, *Prog.Part.Nucl.Phys.* **52**, 197–296 (2004), [arXiv:nucl-th/0305030](https://arxiv.org/abs/nucl-th/0305030).
- [6] P. Braun-Munzinger and J. Wambach, *Rev. Mod. Phys.* **81**, 1031 (2009), [arXiv:0801.4256 \[hep-ph\]](https://arxiv.org/abs/0801.4256).
- [7] K. Fukushima, *J.Phys.G* **39**, 013101 (2012), [arXiv:1108.2939](https://arxiv.org/abs/1108.2939).
- [8] N. Cabibbo and G. Parisi, *Phys. Lett. B* **59**, 67 – 69 (1975).
- [9] F.R. Brown et al., *Phys. Rev. Lett.* **65**, 2491–2494 Nov 1990.
- [10] Y. Aoki et al., *Nature* **443**, 675–678 (2006), [arXiv:hep-lat/0611014](https://arxiv.org/abs/hep-lat/0611014).
- [11] C. DeTar and U. M. Heller, *Eur.Phys.J. A* **41**, 405–437 (2009), [arXiv:0905.2949](https://arxiv.org/abs/0905.2949).
- [12] A. N. Sissakian and A. S. Sorin, *J.Phys.G* **36**, 064069 (2009).
- [13] B. Friman (ed.) et al., *The CBM physics book: Compressed baryonic matter in laboratory experiments* volume 814, (2011).
- [14] N. Glendenning, *Compact Stars: Nuclear Physics, Particle Physics, and General Relativity*, Astronomy and Astrophysics Library. Springer (2000).
- [15] D. Page and S. Reddy, *Ann.Rev.Nucl.Part.Sci.* **56**, 327–374 (2006), [arXiv:astro-ph/0608360](https://arxiv.org/abs/astro-ph/0608360).
- [16] C. Fischer, J. Luecker and J. Mueller, *Phys.Lett. B* **702**, 438–441 (2011), [arXiv:1104.1564](https://arxiv.org/abs/1104.1564).
- [17] J. Pawłowski, *AIP Conf.Proc.* **1343**, 75–80 (2011), [arXiv:1012.5075](https://arxiv.org/abs/1012.5075).
- [18] M. Buballa, *Phys. Rept.* **407**, 205 (2005), [arXiv:hep-ph/0402234](https://arxiv.org/abs/hep-ph/0402234).
- [19] K. Fukushima and T. Hatsuda, *Rept.Prog.Phys.* **74**, 014001 (2011).
- [20] J. C. Collins and M. J. Perry, *Phys.Rev.Lett.* **34**, 1353 (1975).

- [21] D. Bailin and A. Love, *Phys.Rept.* **107**, 325 (1984).
- [22] M. Alford, K. Rajagopal and F. Wilczek, *Phys.Lett. B* **422**, 247–256 (1998), [arXiv:hep-ph/9711395](https://arxiv.org/abs/hep-ph/9711395).
- [23] R. Rapp, T. Schafer, E. V. Shuryak and M. Velkovsky, *Phys.Rev.Lett.* **81**, 53–56 (1998), [arXiv:hep-ph/9711396](https://arxiv.org/abs/hep-ph/9711396).
- [24] M. Alford, A. Schmitt, K. Rajagopal and T. Schafer, *Rev.Mod.Phys.* **80**, 1455–1515 (2008), [arXiv:0709.4635](https://arxiv.org/abs/0709.4635).
- [25] K. Rajagopal and F. Wilczek, *The Condensed Matter Physics of QCD*, November 2000.
- [26] W. Broniowski, *To be published in Acta Phys. Pol. B* (2011), [arXiv:1110.4063](https://arxiv.org/abs/1110.4063).
- [27] A. W. Overhauser, *Phys. Rev. Lett.* **4**, 415–418 Apr 1960.
- [28] D. Ravenhall, C. J. Pethick and J. R. Wilson, *Phys. Rev. Lett.* **50**, 2066–2069 Jun 1983.
- [29] I. Klebanov, *Nucl.Phys. B* **262**, 133 (1985).
- [30] A. S. Goldhaber and N. S. Manton, *Phys. Lett. B* **198**, 231 (1987).
- [31] M. Rozali, H. H. Shieh, M. Van Raamsdonk and J. Wu, *JHEP* **0801**, 053 (2008).
- [32] F. Dautry and E. Nyman, *Nucl. Phys. A* **319**, 323 (1979).
- [33] J. Bardeen, L. N. Cooper and J. R. Schrieffer, *Phys.Rev.* **108**, 1175–1204 (1957).
- [34] P. Bedaque and T. Schafer, *Nucl.Phys. A* **697**, 802–822 (2002), [arXiv:hep-ph/0105150](https://arxiv.org/abs/hep-ph/0105150).
- [35] R. Casalbuoni and G. Nardulli, *Rev.Mod.Phys.* **76**, 263–320 (2004), [arXiv:hep-ph/0305069](https://arxiv.org/abs/hep-ph/0305069).
- [36] P. Fulde and R. A. Ferrell, *Phys. Rev.* **135**, A550 (1964).
- [37] A. I. Larkin and Yu. N. Ovchinnikov, *Zh. Eksp. Teor. Fiz.* **47**, 1136 (1964).
- [38] D. Nickel and M. Buballa, *Phys. Rev. D* **79**, 054009 (2009), [arXiv:0811.2400](https://arxiv.org/abs/0811.2400).
- [39] M. G. Alford, J. A. Bowers and K. Rajagopal, *Phys. Rev. D* **63**, 074016 (2001), [arXiv:hep-ph/0008208](https://arxiv.org/abs/hep-ph/0008208).
- [40] J. A. Bowers and K. Rajagopal, *Phys. Rev. D* **66**, 065002 (2002), [arXiv:hep-ph/0204079](https://arxiv.org/abs/hep-ph/0204079).
- [41] K. Rajagopal and R. Sharma, *Phys. Rev. D* **74**, 094019 (2006), [arXiv:hep-ph/0605316](https://arxiv.org/abs/hep-ph/0605316).

[42] Y. Matsuda and H. Shimahara, *Journal of the Physical Society of Japan* **76**, 051005 May 2007, [arXiv:cond-mat/0702481](https://arxiv.org/abs/cond-mat/0702481).

[43] D. J. Gross and A. Neveu, *Phys. Rev. D* **10**, 3235 (1974).

[44] V. Schon and M. Thies, (2000), [arXiv:hep-th/0008175](https://arxiv.org/abs/hep-th/0008175).

[45] O. Schnetz, M. Thies and K. Urlich, *Annals Phys.* **314**, 425 (2004).

[46] O. Schnetz, M. Thies and K. Urlich, *Annals Phys.* **321**, 2604 (2006).

[47] C. Boehmer, M. Thies and K. Urlich, *Phys. Rev. D* **75**, 105017 (2007).

[48] G. Basar and G. V. Dunne, *Phys.Rev.Lett.* **100**, 200404 (2008), [arXiv:0803.1501](https://arxiv.org/abs/0803.1501).

[49] G. Basar, G. V. Dunne and M. Thies, *Phys. Rev. D* **79**, 105012 (2009).

[50] M. Thies, *J. Phys. A* **39**, 12707 (2006).

[51] D. Ebert, N. V. Gubina, K. Klimenko, S. G. Kurbanov and V. Zhukovsky, *Phys.Rev. D* **84**, 025004 (2011), [arXiv:1102.4079](https://arxiv.org/abs/1102.4079).

[52] R. E. Peierls, *Quantum Theory of Solids*, International series of monographs on physics. Clarendon Press (1955).

[53] G. Gruner, *Rev.Mod.Phys.* **66**, 1–24 (1994).

[54] E. Nakano and T. Tatsumi, *Phys. Rev. D* **71**, 114006 (2005).

[55] R. Rapp, E. V. Shuryak and I. Zahed, *Phys. Rev. D* **63**, 034008 (2001), [arXiv:hep-ph/0008207](https://arxiv.org/abs/hep-ph/0008207).

[56] D. V. Deryagin, D. Y. Grigoriev and V. A. Rubakov, *Int. J. Mod. Phys. A* **7**, 659 (1992).

[57] E. Shuster and D. T. Son, *Nucl. Phys. B* **573**, 434 (2000).

[58] T. Kojo, Y. Hidaka, L. McLerran and R.D. Pisarski, *Nucl.Phys. A* **843**, 37–58 (2010), [arXiv:0912.3800](https://arxiv.org/abs/0912.3800).

[59] B. Y. Park, M. Rho, A. Wirzba and I. Zahed, *Phys.Rev. D* **62**, 034015 (2000), [arXiv:hep-ph/9910347](https://arxiv.org/abs/hep-ph/9910347).

[60] B. Bringoltz, *JHEP* **0703**, 016 (2007), [arXiv:hep-lat/0612010](https://arxiv.org/abs/hep-lat/0612010).

[61] M. Sadzikowski and W. Broniowski, *Phys. Lett. B* **488**, 63 (2000).

[62] I. Frolov, V. Zhukovsky and K. Klimenko, *Phys.Rev. D* **82**, 076002 (2010), [arXiv:1007.2984](https://arxiv.org/abs/1007.2984).

[63] M. A. Halasz, A. D. Jackson, R. E. Shrock, M. A. Stephanov, and J. J. M. Verbaarschot, *Phys. Rev. D* **58**, 096007 (1998), [arXiv:hep-ph/9804290](https://arxiv.org/abs/hep-ph/9804290).

- [64] M. A. Stephanov, K. Rajagopal and E. V. Shuryak, *Phys. Rev. Lett.* **81**, 4816 (1998), [arXiv:hep-ph/9806219](https://arxiv.org/abs/hep-ph/9806219).
- [65] G. 't Hooft, *Nucl.Phys. B* **72**, 461 (1974).
- [66] E. Witten, *Nucl.Phys. B* **160**, 57 (1979).
- [67] L. McLerran and R. D. Pisarski, *Nucl. Phys. A* **796**, 83 (2007).
- [68] T. Kojo, *Nucl.Phys. A* **877**, 70–94 (2012), [arXiv:1106.2187](https://arxiv.org/abs/1106.2187).
- [69] T. Kojo, R. D. Pisarski and A. M. Tsvelik, *Phys. Rev. D* **82**, 074015 (2010), [arXiv:1007.0248 \[hep-ph\]](https://arxiv.org/abs/1007.0248).
- [70] T. Kojo et al., *ArXiv e-prints* July 2011, [arXiv:1107.2124](https://arxiv.org/abs/1107.2124).
- [71] S. Carignano, D. Nickel and M. Buballa, *Phys. Rev. D* **82**, 054009 (2010), [arXiv:1007.1397](https://arxiv.org/abs/1007.1397).
- [72] S. Carignano and M. Buballa, *To be published in Acta Phys. Pol. B* (2011), [arXiv:1111.4400](https://arxiv.org/abs/1111.4400).
- [73] S. Carignano and M. Buballa, (2012), [arXiv:1203.5343](https://arxiv.org/abs/1203.5343).
- [74] V. Koch, *Int.J.Mod.Phys. E* **6**, 203–250 (1997), [arXiv:nucl-th/9706075](https://arxiv.org/abs/nucl-th/9706075).
- [75] J. Goldstone, A. Salam and S. Weinberg, *Phys. Rev.* **127**, 965–970 Aug 1962.
- [76] U. Vogl and W. Weise, *Prog. Part. Nucl. Phys.* **27**, 195 (1991).
- [77] S. P. Klevansky, *Rev. Mod. Phys.* **64**, 649 (1992).
- [78] T. Hatsuda and T. Kunihiro, *Phys. Rept.* **247**, 221 (1994).
- [79] Y. Nambu and G. Jona-Lasinio, *Phys. Rev.* **122**, 345 (1961).
- [80] Y. Nambu and G. Jona-Lasinio, *Phys. Rev.* **124**, 246 (196x).
- [81] M. Asakawa and K. Yazaki, *Nucl.Phys. A* **504**, 668–684 (1989).
- [82] J. Kapusta and C. Gale, *Finite-Temperature Field Theory: Principles and Applications*, Cambridge monographs on mechanics and applied mathematics. Cambridge University Press (2006).
- [83] D. Nickel, private communication.
- [84] M. Gell-Mann and M. Levy, *Nuovo Cim.* **16**, 705 (1960).
- [85] O. Scavenius, A. Mocsy, I. N. Mishustin and D. H. Rischke, *Phys. Rev. C* **64**, 045202 (2001), [arXiv:nucl-th/0007030](https://arxiv.org/abs/nucl-th/0007030).

[86] B. J. Schaefer and J. Wambach, *Phys. Rev. D* **75**, 085015 (2007), [arXiv:hep-ph/0603256](https://arxiv.org/abs/hep-ph/0603256).

[87] V. Skokov, B. Friman, E. Nakano, K. Redlich and B. J. Schaefer, *Phys. Rev. D* **82**, 034029 (2010), [arXiv:1005.3166](https://arxiv.org/abs/1005.3166).

[88] H. Abuki, D. Ishibashi and K. Suzuki, *Phys. Rev. D* **85**, 074002 (2012), [arXiv:1109.1615](https://arxiv.org/abs/1109.1615).

[89] D. Nickel, *Phys. Rev. Lett.* **103**, 072301 (2009), [arXiv:0902.1778](https://arxiv.org/abs/0902.1778).

[90] D. Nickel, *Phys. Rev. D* **80**, 074025 (2009), [arXiv:0906.5295](https://arxiv.org/abs/0906.5295).

[91] C. Itzykson and J. B. Zuber, *Quantum Field Theory*, (1980).

[92] L. D. Landau and E. M. Lifshitz, *Statistical physics*, Number Bd. 1 in Course of theoretical physics. Pergamon Press (1969).

[93] G. Baym, B. L. Friman and G. Grinstein, *Nucl. Phys. B* **210**, 193 (1982).

[94] J. D. Walecka, *Annals Phys.* **83**, 491 (1974).

[95] K. Fukushima, *Phys. Rev. D* **77**, 114028 (2008), [arXiv:0803.3318 \[hep-ph\]](https://arxiv.org/abs/0803.3318).

[96] K. Fukushima, *Phys. Rev. D* **78**, 114019 (2008), [arXiv:0809.3080 \[hep-ph\]](https://arxiv.org/abs/0809.3080).

[97] Z. Zhang and T. Kunihiro, *Phys. Rev. D* **80**, 014015 (2009).

[98] N. M. Bratovic, T. Hatsuda and W. Weise, (2012), [arXiv:1204.3788](https://arxiv.org/abs/1204.3788).

[99] M. Kitazawa, T. Koide, T. Kunihiro and Y. Nemoto, *Prog. Theor. Phys.* **108**, 929 (2002), [arXiv:hep-ph/0207255](https://arxiv.org/abs/hep-ph/0207255).

[100] D. Ebert and H. Reinhardt, *Nucl. Phys. B* **271**, 188 (1986).

[101] C. Ratti, M. A. Thaler and W. Weise, *Phys. Rev. D* **73**, 014019 (2006), [arXiv:hep-ph/0506234](https://arxiv.org/abs/hep-ph/0506234).

[102] K. Fukushima, *Phys. Lett. B* **591**, 277 (2004).

[103] L. D. McLerran and B. Svetitsky, *Phys. Rev. D* **24**, 450 (1981).

[104] F. Karsch and H. W. Wyld, *Phys. Rev. Lett.* **55**, 2242 (1985).

[105] S. Rößner, C. Ratti and W. Weise, *Phys. Rev. D* **75**, 034007 (2007).

[106] L. McLerran, K. Redlich and C. Sasaki, *Nucl. Phys. A* **824**, 86 (2009).

[107] E. Nakano and T. Tatsumi, (2004), [arXiv:hep-ph/0408294](https://arxiv.org/abs/hep-ph/0408294).

[108] W. Broniowski, A. Kotlorz and M. Kutschera, *Acta Phys. Polon. B* **22**, 145 (1991).

- [109] M. Abramowitz and I.A. Stegun, *Handbook of Mathematical Functions*, Dover New York fifth edition (1964).
- [110] F. Correa, G. V. Dunne and M. S. Plyushchay, *Annals Phys.* **324**, 2522 (2009), arXiv:0904.2768 [hep-th].

Acknowledgements

In spite of my nihilistic efforts in trying to fail, so that I could complain afterwards, it appears I almost made it to the end. This would not have been possible without the support of a surprisingly large number of people, which I'm happy to thank here.

My first big thanks goes to Professor J. Wambach, for giving me the opportunity to do some serious research in a great work environment, and for his continuous support, not only on the physics side, but also for the boring bureaucratic stuff. Without him, none of this could have happened.

A huge thanks goes also to Dr. Michael Buballa, who has always been there with his infinite patience to answer all of my stupid questions, and has been a great supervisor and a good friend. I really think I've been spoiled by him.

Another person I am deeply indebted to is Dr. Jean-Sébastien Gagnon. When I was shattered and broken, he picked up and slowly put my pieces back together, and has ever since taken care of my mental health. I hope he realizes how grateful I am.

I am very grateful to David Scheffler, who from the very beginning until now has always helped me with all sorts of problems and taught me zillions of tips and tricks on programming and all kinds of other stuff.

For all the great discussions and help during the early stages of my work I would also like to mention Dr. Dominik Nickel, who simply had an answer for every question I had, and much more.

For all the good times spent together, I want to thank many of my colleagues, in particular Sam Edwards, with all his crazy quirks and ideas, Dr. Richard Williams, for making me rediscover the joy of playing guitar, and Daniel Müller, who somehow always manages to convince me to follow him in his stupid hikes.

A special mention goes also to Dr. Haris Djapo, Nils "smiles, shakes head" Strodtthoff, Daniel Zablocki (to whom I owe something like a thousand beers), Pascal Büscher (mostly for the dartboard), Thorsten Zöller, Michael Linus Knichel (and his car), Hans Beck and Jan Uphoff.

The Helmholtz graduate school for quark matter research H-QM is gratefully acknowledged for its generous financial support through all these years.

Some final thanks go to people who will probably never read this, but still deserve to be in here. First of all, to my parents and my family, for being always so patient with me, even though I really try my best to be as annoying as possible. Then, to my cats, for being so awesome. Finally, to a couple more persons who at some point made my life miserable, but also somehow pushed me to improve myself (whether I succeeded, is a different story), confirming that old saying that whatever doesn't kill us makes us stronger.

Curriculum

Name: Stefano Carignano
Date of birth: 24. July 1984
Place of birth: Moncalieri (Torino), Italy
Citizenship: Italian

09/1998-07/2003	High school “Liceo classico europeo Umberto I”, Torino, Italy
07/2003	High school diploma (Maturità classica europea), Note: 100/100
09/2003 - 09/2006	Undergraduate studies in Physics at Torino University
09/2006	Bachelor in Physics, Note: 110/110 <i>cum laude</i>
10/2006-10/2008	Master studies in Physics of the fundamental interactions at Torino University
10/2008	Master degree in Physics of the fundamental interactions, Note: 110/110 <i>cum laude</i>
03/2009-10/2012	Graduate study in Physics at TU Darmstadt

Eidesstattliche Erklärung

Hiermit erkläre ich eidesstattlich, dass ich die vorliegende Dissertation selbständig verfasst, keine anderen als die angegebenen Hilfsmittel verwendet und noch keinen Promotionsversuch unternommen habe.